University of Zurich

Masterthesis

Faculty of Science
Institute for Theoretical Physics

The intrinsic shape of galaxy clusters

Sebastian Elser

Supervision:
Prof. Dr. Philippe Jetzer, Dr. Mauro Sereno

November 2009

Abstract

In this Master thesis, we studied the estimation of the intrinsic shape of galaxy clusters through multi-wavelength observations. The cluster shape has an influence on the distance and mass estimation of the cluster. It plays an important role in high-precision cosmology. We used parametric models and presented common electron density models and temperature profiles to describe the intracluster medium and derived expression in terms of well known functions for the X-ray surface brightness and the Sunyaev-Zel'dovitch temperature decrement. We showed that X-ray surface brightness measurements are not enough to estimate the cluster shape. Then, we produced observations and fitted them with different models to estimate the elongation of the cluster. We observed that a simple isothermal model is often a good choice to fit a polytropic cluster if the average error on the temperature profile and on the central temperature decrement are $\sigma_{T(r)} \sim 2\,keV$ and $\sigma_{\Delta T_0}/\Delta T_0 \sim 10\%$. Otherwise, the elongation is overestimated by the isothermal model. Assuming the same errors, we showed that a simple isothermal β-model is a good choice to estimate the elongation of a cluster with a central cusp in the electron density. We observed that one can ignore a cool core in the measured temperature profile under centrain circumstances if one wants to estimate the cluster shape.

Contents

1 Introduction **5**

1.1 Galaxy clusters . . . 5

1.1.1 Optical classification . . . 6

1.1.2 Observation . . . 6

1.2 Remarks on astrophysics . . . 8

1.2.1 Bremsstrahlung and X-ray surface brightness . . . 8

1.2.2 Compton scattering and Sunyaev-Zeldovich effect . . . 10

1.2.3 Gravitational lensing . . . 12

1.2.4 Distance measures in cosmology . . . 12

1.2.5 Multiwavelength approach . . . 13

2 Electron density models and temperature profiles **15**

2.1 Electron density models . . . 15

2.1.1 β-model . . . 15

2.1.2 Double β-model . . . 17

2.1.3 Pratt & Arnaud model . . . 18

2.1.4 Vikhlinin model . . . 18

2.1.5 Vikhlinin-Ettori model . . . 19

2.1.6 Hierarchical structure . . . 19

2.2 ICM temperature profiles . . . 20

2.2.1 Isothermal . . . 21

2.2.2 Polytropic model . . . 22

2.2.3 Vikhlinin temperature model . . . 22

3 Projected quantities of ellipsoidal clusters **24**

3.1 The geometry of clusters . . . 24

3.2 Projection effects . . . 27

3.3 Isothermal and polytropic gas . . . 29

3.3.1 β model . . . 29

3.3.2 2β model . . . 31

3.3.3 PA-model . . . 32

3.3.4 VE-model . . . 34

3.3.5 Checking the results . . . 36

3.4 General temperature profile . . . 36

3.4.1 β model . . . 38

3.4.2 2β model . . . 39

3.4.3 PA model . . . 40

3.4.4 VE model . . . 41

3.5 On the deprojection of X-ray surface brightness . . . 41

3.5.1 Analytic counterexample: prolate vs. oblate cluster . . . 41

3.5.2 Degeneracies of the triaxial β model . . . 42

3.5.3 Numerical examples . . . 44

3.5.4 Model independent statements . . . 46

4 On the estimation of the elongation **47**

4.1 X-ray surface brightness . . . 48

4.1.1 Simulation . . . 48

4.1.2 Fitting Procedure . . . 51

4.2 Temperature profile . . . 54

4.2.1 Simulation . . . 55
4.2.2 Fitting procedure . . . 55
4.3 Sunyaev-Zeldovich effect . . . 56
4.4 Combining the simulations . . . 57
4.5 Estimation of the Elongation: Example . . . 58
4.5.1 X-ray surface brightness simulation . . . 59
4.5.2 Fitting procedure . . . 60
4.6 Results . . . 64
4.6.1 β-model, polytropic . . . 64
4.6.2 PA-model, polytropic . . . 66
4.6.3 PA-model with cool core . . . 71
4.7 Summary . . . 74

5 Conclusions and future prospects **76**

6 Some personal remarks **77**

7 Acknowledgments **77**

A Constants **78**

B Parameter α **78**

C Useful Functions **78**

D Additional Calculations **79**

E Integral Solutions **79**

F Detailed Calculations of Several Integrals **80**

1 Introduction

Observations reveal that galaxies are not regularly distributed in space. Rather, they tend to form groups or clusters of galaxies. Groups, clusters and superclusters make up the large scale structure of the universe.

Galaxies provide only a small fraction of the total mass of a cluster. X-ray astronomy reveals that galaxy clusters are intensive sources of X-ray radiation, that is emitted by hot gas between the galaxies, the ICM (intracluster medium). Due to the dynamics of the cluster members, the properties of the X-ray emission, and the observed gravitational lensing data, it seems that dark matter is dominating the mass of clusters.

Galaxy clusters play a remarkable role in cosmology. They are the largest gravitationally bound structures in the Universe and can be observed up to high redshift. Therefore, they are an often used probe for cosmological tests and the evolution of large scale structure or for providing an estimate for cosmological parameters. Moreover, galaxy clusters can act as gravitational lenses which can reveal a view on objects beyond the range of present day telescopes.

Clusters of galaxies are not spherical symmetric. Their intrinsic shape and orientation provides information about the evolution of the mass distribution in the universe, since they have been strongly influenced by the statistical properties of the large-scale primordial density field. Hence, their intrinsic structure probes the cosmic structure formation, because it can show how material aggregates form large-scale structures. Moreover, cluster mass estimations and distance measurements depend on the cluster shape, since the cluster distance obtained through multi wavelength observations and the elongation of the cluster degenerate. So, the intrinsic shape of a cluster is an important parameter.

The goal of this thesis is to investigate methods for the estimation of the three dimensional shape of galaxy clusters, more precisely of the ICM, through the combination of X-ray wave band observations and analysis of the Sunyaev Zeldovich effect. We use a parametric approach. We try to understand the dependence of an estimation of the intrinsic shape on the used models and measurements of the observable quantities. Therefore, first, we derive expressions for the observable quantities. Then, we simulate the observable data of the clusters and fit them with different models and profiles. At last, we could determine their elongation along the line of sight and estimate the effect of different assumptions.

In this introducing section 1, we briefly review general features of galaxy clusters and their observation at different wave lengths. We give some theoretical background of high energy astrophysics and discuss how we can describe the measured data. In section 2, we present a set of models to describe the gas density and the temperature profile of galaxy clusters. They are important to express the observed data in terms of the properties of the ICM. In section 3, we find analytic expressions for the observable quantities of clusters in the case of some of the models. In section 4, we use those expressions to simulate cluster observations, we test our method and examine the effect of different assumptions on the elongation. In section 5, we summarise the most important results we obtained and future prospects are mentioned.

1.1 Galaxy clusters

For many years, only observations in the wave band of visible light were possible. The optical appearance of galaxy clusters invites to classify them. Hence, we will briefly introduce some ideas of classification. Present day telescopes allow to go a step

further and to observe clusters in a wider spectrum from the X-ray to the micro wave band. This provides a lot of new information. We will shortly present some of these instruments.

1.1.1 Optical classification

The most famous compilation of galaxy clusters is the *Abell-catalogue* published by George Abell in 1958. To identify the clusters he looked for overdensities in the galaxy distribution on the plane of the sky. Observations were first limited to the northern sky and then extended to the southern sky. The resulting *ACO-catalogue* (named after Abell, Corwin & Olowin, 1989, [Abell]) includes 4076 clusters.

To arrange this huge amount of objects properly, a classification is desirable. Possible criteria are the number of cluster members or the magnitude of the clusters, both used in the ACO-catalogue (six *richness classes* and seven *distance classes*). The morphology of the galaxy distribution in the clusters is also used to classify them in several ways. So-called regular clusters are compact, are often dominated by a central galaxy and have a large number of members. On the other hand, the irregular clusters are not compact, have no dominant central galaxies, but they often have pronounced substructures and hold not as much cluster member as the regular ones. Thus, regular clusters can be seen as relaxed while irregular ones still undergo evolution [Schneider]. Of course, there is a smooth transition between regular and irregular cluster. These properties show that the morphological classification is connected to physical differences.

Galaxies are the dominant part of the clusters in the optical wave band. Nevertheless, most of the gravitational mass of a cluster is dark matter. Baryonic matter makes up only a small part of the total mass. The largest part of the baryonic matter, e.g. around 30% of the total mass in the case of the Coma cluster [Jetzer 03], is not bound in stars of galaxies but scattered in between. This is the intracluster medium, hot ionized gas, mostly hydrogen. Observations in the X-ray wave band reveal this crucial component of the galaxy clusters. It is assumed that the ICM is a mixture of primordial gas and gas that is ejected from galaxies. It is very hot ($\sim 10^8\,K$) and has a low density ($10^{-3}\,atoms/cm^3$). Several heating mechanisms are proposed to explain such large gas temperature: if gas falls into the cluster, its kinetic energy will be converted to thermal energy due to friction and scattering. Also the constant movement of the galaxies in the cluster causes friction between galaxies and gas. Moreover, supernova explosions in the cluster galaxies can heat up the gas and are important for the enrichment of the ICM. The high temperature leads to an almost fully ionized gas.

1.1.2 Observation

Present day X-ray observatories

Since most of the X-rays are absorbed by atoms and molecules of Earth's atmosphere, observations of the ICM were not possible before space-based X-ray observatories like *UHURU* (1970) or *ROSAT* (1990) were build.

The most important X-ray instruments in space today are the *Chandra X-ray Observatory* and the *X-ray Multi-Mirror Mission*, *XMM-Newton*, both launched in 1999. A combination of the very fine angular resolution of Chandra and the large field of view of XMM-Newton is a powerful tool to reveal the complex structure and physics of the ICM.

Chandra X-ray observatory NASA's Chandra was boosted into an elliptical high-earth orbit that allows long-duration uninterrupted exposures of celestial objects like clusters. The Chandra telescope is operating in the energy band between $0.1-10\,keV$. X-rays from distant clusters of galaxies can be imaged and spectra measured as a function of position within the cluster. The ACIS (*AXAF*[1] *Charged Coupled Imaging Spectrometer*) consists of two CCD arrays with a field of view of $16' \times 16'$, respective $8' \times 48'$ and a spatial resolution of 0"49. Another important instrument is the *High Resolution Camera* (HRI) with a field of view of $30' \times 30'$ and a comparable resolution.

XMM-Newton ESA's XMM-Newton telescope operates in an energy range of $0.1-15\,keV$. There are three co-aligned telescopes. They provide images over a $30' \times 30'$ field of view with a moderate spatial resolution of $5''$ using the *European Photon Imaging Camera* (EPIC). High-resolution spectral information is provided by the *Reflection Grating Spectrometer* (RGS). The gratings, mounted under two telescopes, deflect about half of the X-ray light onto an array of EPIC CCD detectors. An additional telescope is a co-aligned $30\,cm$ optical/UV telescope (called *Optical Monitor*). Hence, one can measure in the X-ray and in the optical/UV band at once. In figure 1, we show a cross section of this observatory.

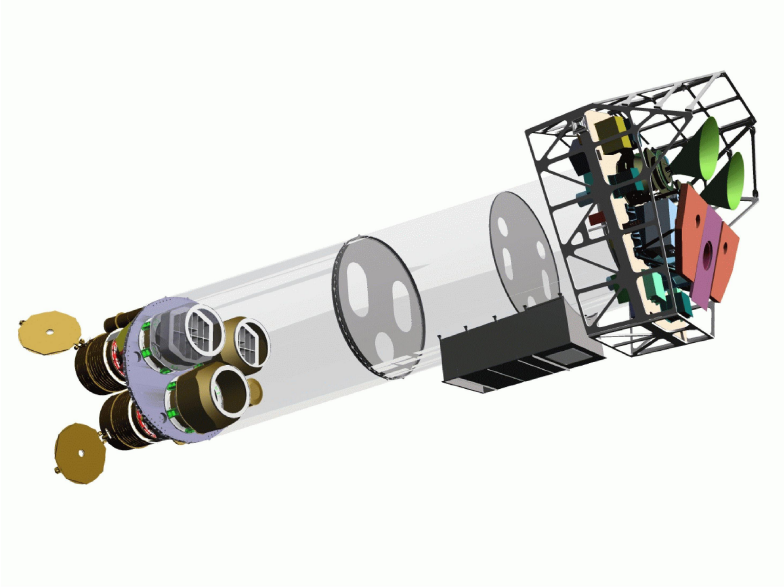

Figure 1: A sketch of the interior of XMM-Newton. On the left, we see the three mirror modules, two of them are equipped with grating arrays. The Optical Mirror is hidden behind the lower module. On the right, there are the EPIC cameras and the spectrometers. From [XMM].

Sunyaev-Zeldovich measurements

One way to detect galaxy clusters and to get information about their ICM is to use the *Sunyaev-Zeldovich effect* (SZ-effect or SZE), see section 1.2.2. This effect is usually measured in the microwave band. Microwaves easily penetrate the atmosphere and ground-based observation is possible. The SZE does not explicitly depend on the redshift of the cluster, and it is almost not sensitive to the used cosmological model, see section 1.2.4. Therefore, it could be a tool to detect all clusters in a given region of the sky because there is almost no limitation due to large distances[2]. On the other

[1] Advanced X-ray Astrophysics Facility

[2] Since the SZE signal is almost independent of redshift, the limit of such surveys is the cluster mass limit. If the clusters are small, the temperature of the gas is small and therefore, the SZ-effect

hand, measurements in the X-ray band depend on the redshift and become more faint with increasing distance as show in figure 2.

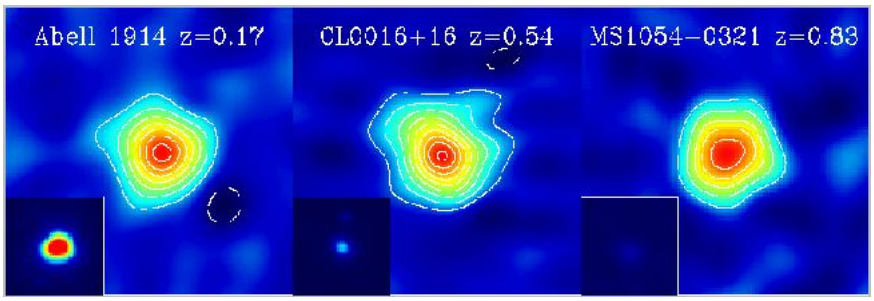

Figure 2: These three clusters at increasing redshift (from left to right) illustrate an advantage of the SZ measurements (large images) compared with X-ray surface brightness map (small images). Clusters a large distances become fainter in the X-ray band while the temperature decrement is not affected by the redshift. It is therefore a powerful tool to search for distant clusters. From [SZA].

Planck The European *Planck* satellite was launched in May 2009 and is operating in the $30 - 857\,GHz$ wave band. Its mean objective is to measure the fluctuations of the Cosmic Microwave Background (CMB). Another result will be the measurement of the distortion of the CMB spectrum, the SZ-effect, in thousands of galaxy clusters, see [Planck] for details.

Owens Valley Radio Observatory The Owens Valley Radio Observatory (OVRO) in California is the largest university-operated radio observatory in the world. Beside other instruments, there are a $40\,m$ telescope and a $5,5\,m$ telescope both constructed in between 1965 and 1968 that are used primarily for studies of the CMB radiation and therefore also for observations of the SZE of known X-ray clusters. First results on this topic were published in 1995, see [Herbig].

1.2 Remarks on astrophysics

Electromagnetic signals provide the only observational constraints on properties of galaxy cluster. Therefore, we will briefly discuss some important processes in high energy astrophysics, see [Jetzer 03] and references there in. Moreover, we will shortly introduce gravitational lensing, a tool which is very important to observe the total cluster mass. Finally, we discuss projection effects in astronomy and how we can combine the projected quantities which are observed at different wavelength to tell something about the shape of galaxy clusters.

1.2.1 Bremsstrahlung and X-ray surface brightness

Bremsstrahlung is radiation emitted in the encounter between an electron and a nucleus; in general, it is emitted whenever a charged particle is accelerated or decelerated. Therefore, if there is hot ionized gas in the Universe, it emits bremsstrahlung.

Electrons in a hot ionized gas at temperature T whose velocity distribution is Maxwellian emit a continuum spectrum of thermal bremsstrahlung. The velocity distribution is as follows:

$$n_e(v) = 4\pi n_e \left(\frac{m_e}{2\pi k_B T}\right)^{3/2} v^2 e^{\frac{-m_e v^2}{2k_B T}} \tag{1}$$

decreases, [Gioia].

where n_e is the number density of electrons, which is in general a function of position, m_e is the rest mass of an electron and k_B the Boltzmann constant.

$I(w, v)$ is the radiation spectrum, a function of particle velocity and radiation frequency. It is given as

$$I(w, v) = \frac{Z^2 e^6 N}{12\pi^3 \epsilon_0^3 c^3 m_e^2} \frac{1}{v} ln\Lambda \tag{2}$$

in the case of high energetic but still non-relativistic electrons, where N is the number density of nuclei and $\Lambda = \frac{8\pi\epsilon_0 m_e v^3}{Ze^2\omega}$ for low electron velocities ($v < Z\,c/137$), and $\Lambda = \frac{2m_e v^2}{\hbar\omega}$ for high velocities ($v \geq Z\,c/137$). Z is the atomic number of the involved nucleus. ϵ_0 is the electric constant, commonly known as vacuum permittivity.

The spectral emissivity of the plasma, k_ν, defined as the emitted energy per unit time, frequency and volume, is given as

$$k_\nu = \int_0^\infty n_e(v)\, I(w, v)\, dv \propto Z^2 \frac{1}{\sqrt{k_B T}} g(\nu, T) N n_e e^{\frac{-h\nu}{kT}}, \tag{3}$$

where g is the averaged Gaunt factor, a quantum mechanical factor related to the number of states. Typically, $g \simeq 1.2$. Therefore, the spectrum is nearly an exponential function of the frequency ν.

By integrating the spectral emissivity k_ν over the frequency we find the total energy loss rate of the plasma:

$$-\left(\frac{dE}{dt}\right) \propto Z^2 T^{1/2} g N n_e. \tag{4}$$

A cluster of galaxies or more precisely the intracluster medium is a source of thermal bremsstrahlung. A typical X-ray spectrum of intracluster gas with its characteristic exponential shape is show in figure 3. Moreover, if the metallicity of the plasma is not zero, strong emission lines occur above the bremsstrahlung spectrum. Processes contributing to X-ray line emission from a diffuse plasma include collisional excitation of valence or inner shell electrons and radiative recombination. These emission lines, especially the so-called Fe K line at $7keV$, can be used to determine the redshift of the clusters. Moreover, in addition with the position of the exponential cut off of the X-ray spectrum and its shape, they are good tools to determine the temperature of the gas.

X-ray surface brightness Observations in the keV-regime performed by instruments like Chandra reveal a map of the galaxy cluster that is produced by bremsstrahlung and line emission in the intracluster medium. This surface brightness is given by

$$S_X = \frac{1}{4\pi\,(1+z)^4} \int_{los} n_e^2 \Lambda(T_e, Z)\, dl. \tag{5}$$

According to (4), the total emissivity is proportional to n_e^2, assuming $n_e \simeq N$. $\Lambda(T_e, Z)$ is called the *cooling function* of the intracluster medium. It is usually a power law of the temperature, i.e. $\Lambda(T_e, Z) \sim \Lambda(Z) T_e^\alpha$, whereas α depends on the energy band of the instrument, the electron temperature and the metallicity of the gas. Usually, if $T_e > 2.5\,keV$, the emission is mainly due to bremsstrahlung and $\tilde{\Lambda} = 3.0 \times 10^{-27}\, erg\, cm^3\, s^{-1}\, K^{-\alpha}$ and $\alpha = 0.5$, [Sarazin]. Ettori [Ettori 00] derived α in the case of different energy windows, temperature regimes and metallicities, which should lead to a more appropriate cooling function, see appendix. Λ also embodies the averaged Gaunt factor. The factor of 4π arises from the assumption that the emissivity is isotropic, while the $(1+z)^4$ factor takes into account the cosmological expansion of

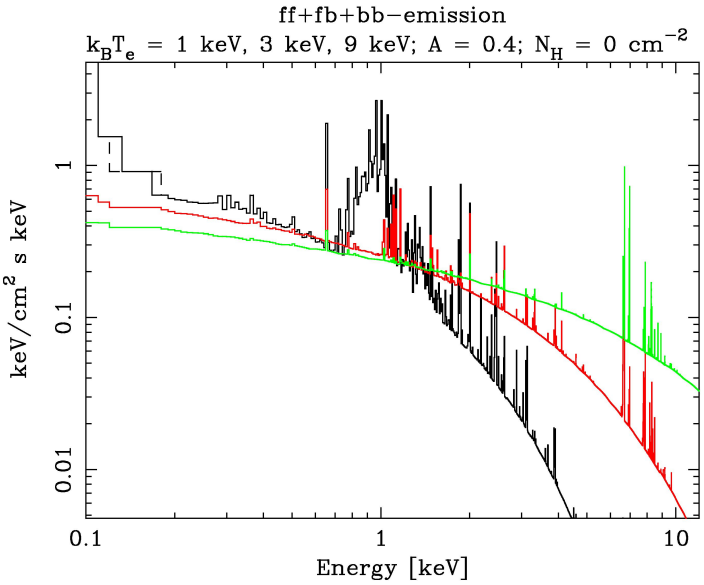

Figure 3: X-ray emission of a hot plasma. Three different gas temperatures are shown, ($1\,keV$, $3\,keV$, $9\,keV$). The radiation of the hotter gas reaches higher energies. We see the exponential cutoff. In addition, the line emission is taken into account. It gains importance if the temperature is lower. The photoabsorbtion is neglected since the H column density is $0\,cm^{-2}$. From [Schneider].

spectral surface brightness and energy.

1.2.2 Compton scattering and Sunyaev-Zeldovich effect

Compton scattering describes high energy photons which scatter on electrons. Usually, if the electrons are nearly at rest, a fraction of the momentum is transferred from the photon to the electron, i.e. the frequency of the photon decreases. If the energy of the incoming photon is low enough to ignore the momentum transfer, this process is called Thompson scattering.

For a stationary electron, the change of the photon wavelength $\Delta\lambda$ is given as:

$$\frac{\Delta\lambda}{\lambda} = \frac{\hbar\omega}{\gamma m_e c^2}(1 - cos\alpha), \tag{6}$$

where λ is the wavelength and $\hbar\omega$ the energy of the incoming photon, γ is the common relativistic factor and α is the scattering angle.

If low energy photons hit ultrarelativistic electrons, the photons acquire energy from the electrons. This process is called *inverse* Compton scattering because the electrons lose energy rather than the photons.

Consider a hot thin plasma, e.g. the hot intergalactic gas in clusters of galaxies. Photons which pass through this medium will lose or acquire energy. In the non-relativistic regime in which $kT_e \ll m_e c^2$ and $\hbar\omega \ll m_e c^2$ (T_e is the electron gas temperature, ω the angular frequency of the photon), the overall energy change of a photon $\Delta\epsilon$ is

$$\frac{\Delta\epsilon}{\epsilon} = -\frac{\hbar\omega_0}{m_e c^2} + 4\frac{kT_e}{m_e c^2}, \tag{7}$$

where $\hbar\omega_0$ describes the photon energy before the scattering event.

A detailed description of how the energy spectrum of the photons gets modified requires the use of the Boltzmann equation. In the non-relativistic regime, the energy transfer will be small. Therefore, the Boltzmann equation can be expanded to the second order in $\Delta\epsilon$, leading to an approximation which is known as *Kompaneets equa-*

tion. It is used to describe the distortions of the spectrum of the cosmic microwave background radiation, figure 4. The CMB intensity increases at frequencies above 218 GHz and decreases at lower frequencies.

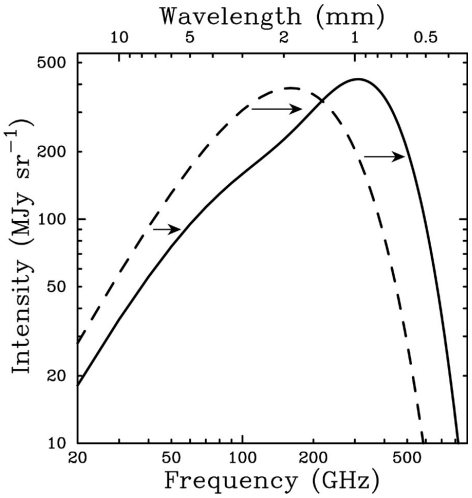

Figure 4: The Sunyaev-Zeldovich effect leads to a distortion of the cosmic microwave background radiation spectrum. This distortion is shown for a fictional cluster around 1000 times more massive than a typical massive galaxy cluster. The SZE causes a decrease in the CMB intensity at frequencies lower than $218\,GHz$ and an increase at higher frequencies. From [Reese 03].

Thermal Sunyaev-Zeldovich effect In 1970, Sunyaev and Zeldovich [SZ 70] have found the following temperature decrement in the Rayleigh Jeans region ($h\nu \ll k_B T$) of the CMB spectrum:

$$\frac{\Delta T}{T_{CMB}} = -2y, \tag{8}$$

where y is called the *Comptonisation parameter*. It is given by

$$y = \int_{los} \frac{\sigma_T k_B}{m_e c^2} n_e T_e \, dl. \tag{9}$$

σ_T is the Thompson cross section. The integration is along the line of sight ('los'). If T_e does not depend on the position, y is proportional to the optical depth and is therefore also called Compton optical depth.

If the CMB photons are scattered as they propagate to the Earth through regions of very hot plasma, as in the case of clusters of galaxies, the temperature decrement is called Sunyaev Zeldovich Effect (SZ effect or SZE). It is typically of the order $\sim 1\,mK$ at frequencies in the Rayleigh-Jeans regime and provides information about the electron density in the ICM and is a good tool to detect clusters: Galaxy clusters cast shadows below 218 GHz and shine above.

In general, the measured temperature decrement is given by

$$\frac{\Delta T_{SZ}}{T_{CMB}} = f_{SZ}(\nu, T_e) \frac{\sigma_T k_B}{m_e c^2} \int_{los} n_e T_e \, dl. \tag{10}$$

$f_{SZ}(\nu, T_e)$ gives the frequency dependence of the temperature decrement and also accounts for relativistic corrections at frequency ν, this results in a change of the prefactor compared to equation (8)[3]. The integrand is proportional to the gas pressure, $P \propto n_e\, T_e$. We remark that this decrement does not depend explicitly on the redshift.

[3]More precisely, in the Rayleigh-Jeans limit $f_{SZ}(\nu, T_e) \to -2$, [Reese 02]

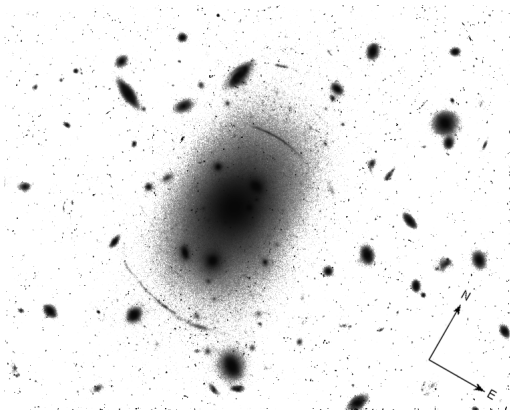

Figure 5: The galaxy cluster Abell 963 is member of the Abell-catalogue. The apparent cluster center of A963 is located at $(RA, Dec.) = (10^h17^m03^s.62), 39°02'48''.84)$ in 2000, the redshift of the brightest cluster galaxy is $z = 0.206$. Due to the strong gravitational lensing effect, two giant arcs appear at the north and south of the cluster. These are distorted, multiple images of two galaxies at $z = 0.771$ (north) and $z = 1.958$ (south). From [Elser].

1.2.3 Gravitational lensing

In this thesis, we won't use this powerful tool to analyse clusters. Nevertheless, it is worth mentioning. More information can be found in [Elser] and references therein.

One of the statements of General relativity is the deflection of light rays when they propagate through a gravitational field. Gravitational lensing occurs when light of a bright source far away, for example quasars, is bended around a massive object like a galaxy cluster. In this case, the gravitational field is similar to an optical lens.

Hence, a fundamental difference to X-ray emission and SZ effect is that gravitational lensing does not probe the electron density but maps the total mass of the cluster. Usually, this mass can be related to the ICM if the gas is assumed to be in hydrostatic equilibrium with the gravitational potential of the cluster. After estimating the total mass of the cluster, one can get information about the dark matter component.

There are two methods to estimate the the cluster mass. In strong lensing, the surface mass density is obtained by fitting the multiple images of the background source, figure 5. In weak lensing, analysis of the statistical distortion of the background images reveals the projected lens mass.

1.2.4 Distance measures in cosmology

Galaxy clusters belong to the farthest objects, we can observe today. Those large distances have to be handled with care. In cosmology there are many ways to specify the distance between two points [Hogg]. Because of the expanding Universe, the distances between comoving objects are constantly changing. The concept of distance in curved spacetime are more complicated than in the Euclidean case. For a quantitative description, we have to assume that our Universe is described through the Friedmann-Robertson-Walker metric.

The Hubble constant H_0 is the factor of proportionality between recession speed v and distance d in the expanding Universe. The Hubble distance is defined as

$$D_H \equiv \frac{c}{H_0} = 9.26 \times 10^{25}\, h^{-1} m, \tag{11}$$

where $0.6 < h < 0.9$ and c is the speed of light. The mass density ρ and the value of the cosmological constant Λ are dynamical properties of the Universe. They are often

rescaled in a dimensionless form, depending on H_0 and their present day values, Ω_M and Ω_Λ. The third parameter, the 'curvature of space' Ω_K is defined by the relation

$$\Omega_M + \Omega_\Lambda + \Omega_K = 1. \tag{12}$$

This allows several combinations of parameters whereas Ω_M is larger than zero. Common models are for instance the high lambda model $(\Omega_M, \Omega_\Lambda, \Omega_K) = (0.2, 0.8, 0)$ or the Einstein-de-Sitter model $(\Omega_M, \Omega_\Lambda, \Omega_K) = (1, 0, 0)$.

The *angular diameter distance* D_A is defined as the ratio of an object physical transverse size at a redshift z to its angular size. The angular diameter distance from the observer to an object at redshift z depends on the cosmological parameters and is given as

$$D_A(z) = \frac{1}{1+z} \frac{c}{H_0|\Omega_{K0}|} S_K \left(\int_0^z \frac{|\Omega_{K0}|}{H(z')} dz' \right), \tag{13}$$

where $H(z') = \sqrt{\Omega_{M0}(1+z')^3 + \Omega_{K0}(1+z')^2 + \Omega_{\Lambda 0}}$. The subscript 0 denotes the present value. $S_K(x)$ is defined as $sin(x)$ if the Universe is closed, $\Omega_{K0} < 0$, $S_K(x) = sinh(x)$ if the Universe is open, $\Omega_{K0} > 0$, and $S_K(x) = x$ if the metric is flat, $\Omega_{K0} = 0$.

1.2.5 Multiwavelength approach

X-ray surface brightness, Sunyaev-Zeldovich temperature decrement and gravitational lensing are especially powerful tools if we combine them. This helps to determine properties of the cluster or to estimate cosmological parameters.

A combination of SZ-effect and X-ray emission measurements yields an estimate of the distance to the cluster and therefore a determination of the Hubble constant. It is enough to focus on the central values. The temperature decrement is proportional to

$$\frac{\Delta T_{SZ,0}}{T_{CMB}} \propto n_{e,0} T_{e,0} L, \tag{14}$$

where L is the cluster's length along the line of sight. We obtain this, if we substitute the integration along the line of sight by a multiplication. It is inversely proportional to the elongation e_Δ. The X-ray brightness in contrary is proportional to

$$S_{X0} \propto n_{e,0}^2 L. \tag{15}$$

We can determine T_e through a X-ray spectrum analysis. We can eliminate n_e in (14) and (15) and get

$$\Delta T_{SZ,0} \propto \sqrt{S_{X0} L}. \tag{16}$$

Next, we assume spherical symmetry of the cluster. Therefore, we can equalise the length L along the line of sight and a width R on the plane of the sky, $L = R = \theta D_A$. θ is the angular diameter of the cluster (13). Hence:

$$D_A = \frac{L}{\theta} \sim \frac{R}{\theta} \propto \Delta T_{SZ,0}^2 \frac{1}{S_{X0}}. \tag{17}$$

This proportionality allows to estimate the angular diameter distance of the cluster if we know the central temperature decrement, the X-ray surface brightness and the ICM temperature. Therefore, a determination of the Hubble constant, $D_A \propto 1/H_0$ is possible, see the previous section.

Of course, the assumption that the cluster is spherical is often not justified. Then, the elongation and the angular diameter distance, respectively the Hubble constant are degenerate and we can't determine both at once. This degeneracy can be broken only

with information about the cluster potential provided by gravitational lensing and an additional constraint given by the assumption of hydrostatic equilibrium which connects the pressure and the gas density, [Fox & Pen 02].

Instead, if the cosmological parameters are known, we can determine the elongation of the cluster thought X-ray surface brightness and temperature decrement observations. If the cluster is not spherical, an additional factor $1/\sqrt{f}$ occurs, see section 3.1. It is related to the elongation and the projected length scale l_p. We get

$$S_{X0} \propto n_{e,0}^2 \frac{l_c}{\sqrt{f}} = n_{e,0}^2 \frac{l_p}{e_\Delta}, \tag{18}$$

$$\Delta T_{SZ,0} \propto n_{e,0} \frac{l_c}{\sqrt{f}} = n_{e,0} \frac{l_p}{e_\Delta}. \tag{19}$$

If we calculate

$$\frac{S_{X0}}{\Delta T_{SZ,0}^2} \propto \frac{l_p}{e_\Delta} \frac{e_\Delta^2}{l_p^2} = \frac{e_\Delta}{l_p}, \tag{20}$$

we can solve for e_Δ, whereas n_{e0} drops out. If the angular diameter distance in $l_p = \theta_p D_A$ is not known, we can not determine the elongation, as mentioned above.

2 Electron density models and temperature profiles

Galaxy clusters consist of up to thousands of galaxies, the ICM and a large amount of DM. As described above, beside optical observations, measurements in the X-ray and micro wave band are important. Those rays originate from the ICM. To characterise the shape of the ICM, it is often described by models. These parametrisations of n_e are of crucial importance for the goal of this thesis, because it allows us to find simpler expressions for the X-ray surface brightness and the SZ temperature decrement. This will result in advantages in the calculations.

The following section introduces the most important models that are used to describe electron densities in galaxy clusters in recent research. We will give the motivation for each model, their benefits and disadvantages. In addition, we will also present different temperature profiles.

2.1 Electron density models

During the last decades, several models have been proposed to parameterize the gas density profile in clusters, from the simple β-model (1976) with two free parameters to the model proposed by Vikhlinin (2006) with 10 independent free parameters.

Here, the models are introduced assuming spherical symmetric density distributions described by radius r. They are generalised to ellipsoidal distributions by changing $r \to \zeta$, whereas ζ is the ellipsoidal radius.

2.1.1 β-model

Cavaliere & Fusco-Femiano noted in 1978 that "...gas and galaxies distributions conforms to the same gravitational potential, the former can be directly related to the latter..." [Cavaliere].

Hydrostatic equilibrium[4] of the gas implies

$$\frac{1}{\rho_{gas}(r)} \frac{dP_{gas}(r)}{dr} = -\nabla\Phi(r), \tag{21}$$

whereas $\Phi(r)$ is the cluster gravitational potential, $P_{gas}(r) \propto \rho(r)\, T(r)$ is the radial gas pressure and $\rho_{gas}(r)$ is its density. Moreover, let the gas distribution be isothermal, $T(r) = T$.

If we assume an 'isothermal' distribution of the galaxies, i.e. their radial velocity dispersion is independent of the radial distance to the center, hydrostatic equilibrium implies

$$\frac{1}{\rho_{gal}(r)} \frac{dP_{gal}(r)}{dr} = -\nabla\Phi(r), \tag{22}$$

where $P_{gal}(r)$ is the radial pressure that is connected to the radial velocity dispersion of the galaxies $P \propto \langle v^2 \rangle$ and $\rho_{gal}(r) = \langle m \rangle\, n(r)$ is the mean mass of a galaxy times the number density.

Comparing equations (21) and (22), it follows

$$\rho_{gas}(r) \propto [\rho_{gal}(r)]^{\beta}, \tag{23}$$

[4] The gas is in hydrostatic equilibrium, i.e. the gravitational forces due to the cluster potential is balanced by the pressure force, if the time required for a sound wave in the ICM to cross the cluster is short compared to the probable age of a cluster unless the gravitational potential varies on a shorter time scale or the gas is heated or cooled more rapidly than this. Usually, gas cools due to emission. This time scale is inverse proportional to the gas density and may be small close to the dense cluster center, [Schneider].

whereas β is a parameter that depends essentially on gas temperature and velocity dispersion of the galaxies along the line of sight σ_v,

$$\beta \propto \sigma_v^2 / T_{gas}. \tag{24}$$

Let's introduce a special kind of density model that describes an isothermal distribution of galaxies, the so called *King model*:

$$\rho_{gal}(r) = \rho_0 \left(1 + (r/r_c)^2\right)^{-\frac{3}{2}}, \tag{25}$$

where r_c is the core radius.

Including the connection between gas and galaxy density, we get a gas density profile, called *β-model*

$$\rho_{gas}(r) = \rho_0 \left(1 + (r/r_c)^2\right)^{-\frac{3\beta}{2}}, \tag{26}$$

whereas β and r_c parameterize this distribution. Here, we normalized $\rho_0^\beta \to \rho_0$.

In general, we assume that the gas is hot and nearly fully ionized. Therefore, the gas density ρ_{gas} may be considered as tracer of the electron number density n_e. Hence:

$$n_e(r) = n_{e0} \left(1 + (r/r_c)^2\right)^{-\frac{3\beta}{2}}. \tag{27}$$

The β-model is widely used. It has only two degrees of freedom (or three, if we count the central electron density too). They have a physical background: the core radius determines the border of the core, i.e. the radius of the change of slope of the profile, where the density is not flat anymore. The β parameter describes the slope of the density decrement. Degeneracies among those two parameters are obvious, an increase of the β-parameter can almost be compensated by an increase of the core radius. Figure 6 illustrates the dependence of n_e on the two parameters.

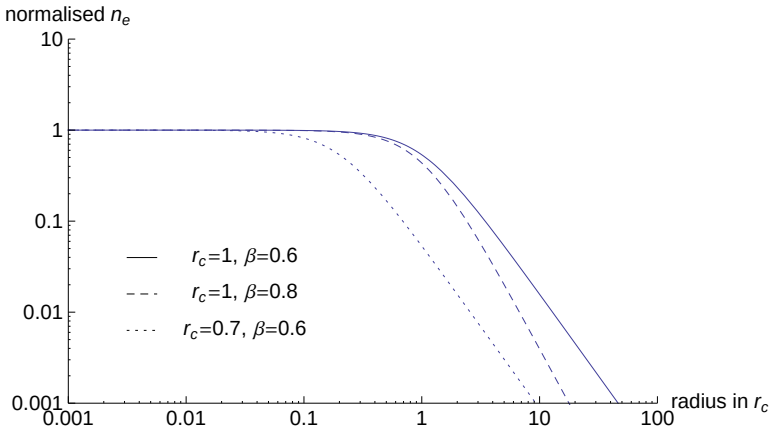

Figure 6: β-model and its dependence on the slope parameter β and the core radius r_c. The electron density is normalized. The radial coordinates are given in units of r_c.

Since there is a relatively simple dependence on the radius, analytic expressions of the projected quantities are easily to find if this model is used. This simplicity holds also disadvantages, of course.

- Due to its small number of free parameters, this model it is often not able to provide a good fit to the data.
- Isothermality is not observationally confirmed, e.g. so called cool cores have been

observed. Moreover, if $\beta < 2/3$, an increasing temperature with cluster radius is required to guarantee an asymptotic baryon fraction that is consistent with the Universe [Xue], which is in contradiction to isothermality and the model is not self consistent.

- The so called β-discrepancy is still not fully explained. It describes a mismatch between the measured and fitted β parameter. Measurements of the gas temperature and the velocity dispersion of the galaxies provide a value of $\beta = \beta_{spec} \simeq 1$ as one would expect in the isothermal case. If the β-model profile is fitted to an X-ray surface brightness map, the slope is $\beta = \beta_{fit} \simeq 0.65$, [Sarazin]. Low-accuracy temperature measurements and an anisotropic velocity distribution of the galaxies might cause this discrepancy.

Fortunately, there are many ways to improve and generalize this model, what we will show below.

2.1.2 Double β-model

In order to improve the model, we add a second β-model, with a new central density $n_{e0,2}$, new core radius $r_{c,2}$ and new slope-parameter β_2. It is especially useful to represent the excess of X-ray emission that is observed at the central region of several clusters and that can not be accounted for by the flat core of the single β-model.

This model is called *double β-model* or 2β-model. The electron density is given by

$$n_{e,2\beta}(r) = \left[n_{e0,1}^2 \left(1 + (r/r_{c,1})^2\right)^{-3\beta_1} + n_{e0,2}^2 \left(1 + (r/r_{c,2})^2\right)^{-3\beta_2} \right]^{\frac{1}{2}}. \qquad (28)$$

Conventionally, $r_{c,1}$ describes the core radius of the central emission region, $r_{c,2}$ is the core radius of the overall distribution, the length scale. Therefore, to mimic a central excess of emission, usually $\beta_1 \geq \beta_2$. In figure 7, we see how the two separate β-models add to the double β-model. Since the emissivity of the ICM is proportional to n_e^2, the X-ray surface brightness is expressed in terms of the square of the electron density. Therefore, the double β-model is defined through the sum of the squares of two density profiles: $n_e^2 = n_{e1}^2 + n_{e2}^2$ and not through the ordinary sum.

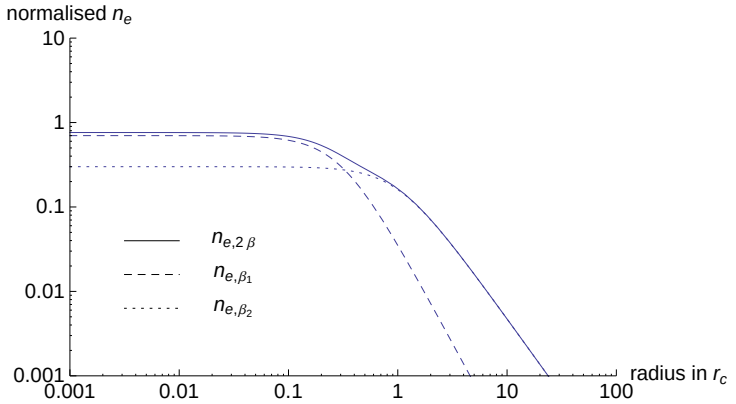

Figure 7: A profile plot of a 2β-model. The single β models with their slopes β_1 and β_2 and different core radii and central electron densities add to a 2β-model. The parameters are ($\beta_1 = 0.8, \beta_2 = 0.6$, $\frac{n_{e0,1}}{n_{e0,1}+n_{e0,2}} = 0.7$, $\frac{r_{c,1}}{r_{c,2}} = 0.3$). The electron density is normalized. The radial coordinates are given in units of $r_c = r_{c,2}$.

2.1.3 Pratt & Arnaud model

Pratt and Arnaud [P & A 02] proposed an alternative parameterization to describe the gas density profile close to the cluster center. We will call this model PA-model for short. At large radii, it behaves similar to a β-model, but there is a power-law-type cusp at the center:

$$n_{e,PA}(r) = n_{e0}\,(r/r_c)^{\frac{-\eta}{2}}\left(1+(r/r_c)^2\right)^{-\frac{3\beta}{2}+\frac{\eta}{4}}. \tag{29}$$

The additional parameter η describes the slope at small radii[5]. Figure 8 presents the behaviour of the profile if η is changed.

If $\eta = 2$, $\beta = 1$, this profile varies from $n_e(r) \propto r^{-1}$ at small radii to $n_e(r) \propto r^{-3}$ at large radii. In this case, it is identical to the Navarro Frenk White (NFW) profile, which describes dark matter halos, [NFW].

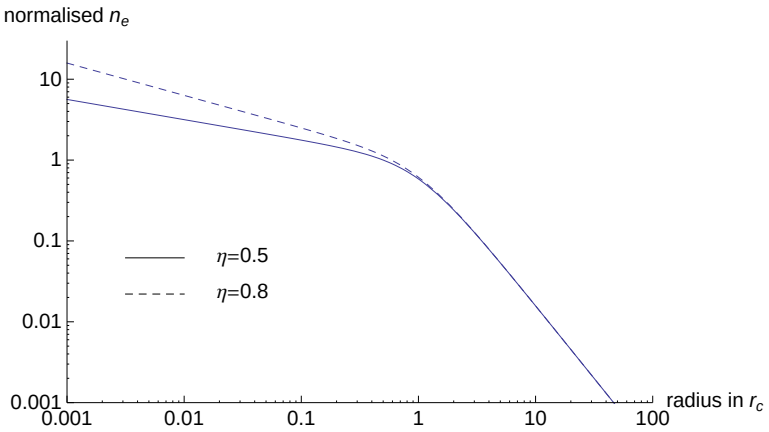

Figure 8: A profile plot of a PA-model and its dependence on the slope parameter η. It controls the strength of the central peak. The electron density is normalized and $\beta = 0.6$. The radial coordinates are given in units of r_c.

2.1.4 Vikhlinin model

Observed X-ray brightness profiles reveal a change of slope at a certain distance $r = r_s$ relative to the power-law at smaller radii, [Vikhlinin 99]. Starting from the PA-Model, in 2006 Vikhlinin et al. [Vikhlinin 06] added a radial dependent factor to describe this change:

$$n_e(r) = n_{e0,1}\,(r/r_{c,1})^{-\frac{\eta}{2}}\left(1+(r/r_{c,1})^2\right)^{-\frac{3\beta}{2}+\frac{\eta}{4}}\left(1+(r/r_s)^\kappa\right)^{-\frac{\epsilon}{2\kappa}}. \tag{30}$$

Three additional parameters are introduced: r_s gives the distance where the change happens, ϵ describes the amplitude of the change of slope and κ controls the width of the transition region.

In order to gain additional modeling freedom near the central cluster region, they added a second β-model, similar as in the case of the double β-model and take the

[5]In the original Pratt & Arnaud paper, they add a factor of 2 to this parameter: $n_{e,PA}(r) = n_{e0}(r/r_c)^{-\eta}\left(1+(r/r_c)^2\right)^{-3\beta/2+\eta/2}$. In order to get a similar parametrisation as in the following models, we changed it.

sum of their squares.

$$n_{e,Vik}(r) = \Bigg[n_{e0,1}^2 \left(r/r_{c,1}\right)^{-\eta} \left(1+\left(r/r_{c,1}\right)^2\right)^{-3\beta_1+\frac{\eta}{2}} \left(1+\left(r/r_s\right)^{\kappa}\right)^{-\frac{\epsilon}{\kappa}} + n_{e0,2}^2 \left(1+\left(r/r_{c,2}\right)^2\right)^{-3\beta_2} \Bigg]^{\frac{1}{2}}. \tag{31}$$

This model has ten independent degrees of freedom, which allow to gain better fits. On the other hand, these parameters are strongly correlate and therefore degenerate. Moreover, the introduction of a sum due to the additional β-model part avoids an at least semi-analytic treatment if we are concerned with the integrals appearing in the observable quantities.

2.1.5 Vikhlinin-Ettori model

In a recent paper of Ettori et al., [Ettori 09], they used the Vikhlinin model without the additional β term. That's why we will call this reduced model Vikhlinin-Ettori model or VE-model:

$$n_{e,VE}(r) = n_{e0}\left(r/r_c\right)^{-\frac{\eta}{2}} \left(1+\left(r/r_c\right)^2\right)^{-\frac{3\beta}{2}+\frac{\eta}{4}} \left(1+\left(r/r_s\right)^{\kappa}\right)^{-\frac{\epsilon}{2\kappa}}. \tag{32}$$

Figure 9 illustrates its profile. A huge advantage of this form is that there are simplifications if we calculate the observed quantities. Thus, we will always prefer this model.

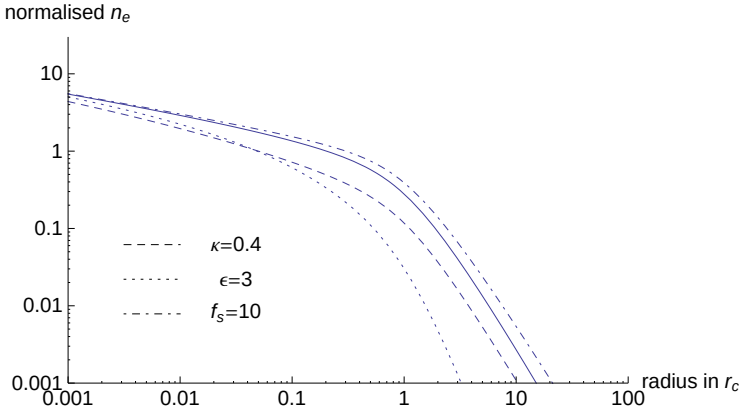

Figure 9: A profile plot of a VE-model and its dependence on the parameters η, κ and the radius at which the slope changes in units of r_c: $f_s = r_s/r_c$. The lines denote the model if we exchange the initial parameter with the one that is corresponding to the line. The parameters of the initial model (drawn through line) are $(\beta = 0.6, r_c = 0.6, f_s = 5, \epsilon = 1, \kappa = 0.5)$. The electron density is normalized. The radial coordinates are given in units of r_c.

2.1.6 Hierarchical structure

It is obvious that the above models are based on each-other as frequently mentioned: Each step increases the degree of detail and therefore each improvement adds a number of new degrees of freedom.

An adequate choice of the parameters reduces the models and we can go backwards step by step. This could be an advantage because if we work with a complex model, we can simply drop some parameters and get the result of a simpler model at the same time.

model	β	2β	PA	VE	Vikhlinin
slopes	β	β_1	β	β	β_1
	-	β_2	-	-	β_2
	-	-	η	η	η
	-	-	-	ϵ	ϵ
	-	-	-	κ	κ
radii	r_c	$r_{c,1}$	r_c	r_c	$r_{c,1}$
	-	$r_{c,2}$	-	-	$r_{c,2}$
	-	-	-	r_s	r_s
densities	n_{e0}	$n_{e0,1}$	n_{e0}	n_{e0}	$n_{e0,1}$
	-	$n_{e0,2}$	-	-	$n_{e0,2}$
#parameters	3	6	4	7	10

Table 1: Comparison of the degrees of freedom of the models in section 2.1. #parameters gives the number of degrees of freedom.

β-model	$\rightarrow$	Pratt & Arnaud-model	$\rightarrow$	Vikhlinin-Ettori-model
$\downarrow$				$\downarrow$
2β-model		$\rightarrow$		Vikhlinin-model

Table 2: Schematic hierarchical structure of the electron density model denotes their affinities.

This hierarchy allows to give some general statements about the properties of those profiles, which are also illustrated in figure 10, where we assume the same model parameters for all models. The asymptotic slope is always β in the case of the PA-model and β_2 in the case of the 2β-model. So, their asymptotic behaviour can be modeled with the β-model. The VE-model has a slope change in the outer regions and has therefore a different slope. Close to the center, the PA-model and the VE-model form a peak, whereas the β- and 2β-model are flat.

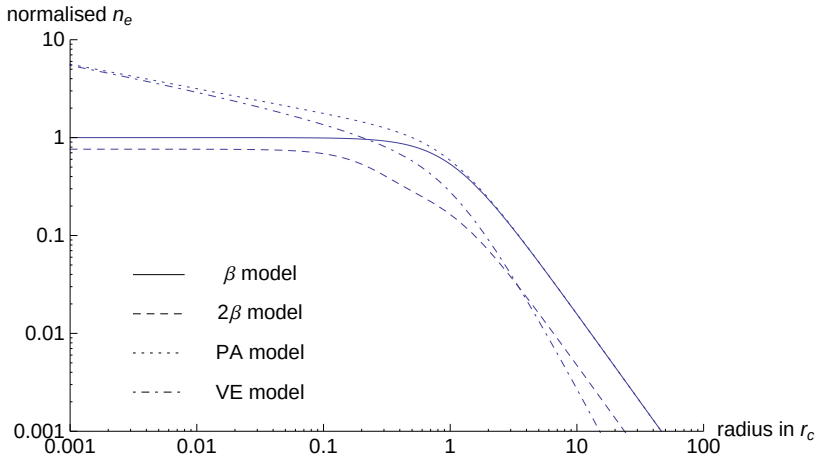

Figure 10: A comparison of the radial profile of the for introduced electron density models. The central electron density is normalized with $n_{e0,\beta}$. The model parameters are $r_c = 1, \beta = 0.6, \eta = 0.5, \beta_1 = 0.8, \beta_2 = 0.6, \frac{n_{e0,1}}{n_{e0,1}+n_{e0,2}} = 0.7, \frac{r_{c,1}}{r_{c,2}} = 0.3, r_s/r_c = 5, \epsilon = 1, \kappa = 0.5$. Beside the VE-model, the slope at large radii is identical. The VE- and PA-model form a similar peak at the center.

2.2 ICM temperature profiles

Beside the electron density, the temperature profile of the ICM is involved in both the X-ray surface brightness and the SZ-effect. Recent observations have revealed that the temperature is neither constant along the radius nor described by a simple linear function. In some clusters, there is a so called *cool core*. The high density of the

gas close to the cluster center forces an increase in emission of the gas, energy is lost through radiation and the ICM cools. Since the temperature profile influences the observable quantities, it can be crucial to take it into account correctly. But simplified profiles have also their advantages.

Temperature measurements of galaxy clusters have usually a low resolution. The spectroscopic temperature T_{spec} is obtained from interpreting the measured spectra of the ICM. It is not simple to define a counterpart of this quantity if we describe a simulated cluster, [Mazzotta]. The most common temperature function used is the so called emission-weighted temperature function defined as

$$T_{ew} = \frac{\int \Lambda(T,Z) n^2 T dV}{\int \Lambda(T,Z) n^2 dV}. \tag{33}$$

Mazzotta et al. have shown that it is better to use a so called spectroscopic like temperature function defined as

$$T_{sl} = \frac{\int W T dV}{\int W dV}. \tag{34}$$

where W is the weighting function

$$W = \frac{n^2}{T^{3/4}}. \tag{35}$$

Compared to the weighting of T_{ew}, where $\Lambda \propto \sqrt{T}$, W weights inversely by the temperature. Thus, if the cluster thermal structure is complex, T_{ew} will substantially differ from T_{spec}. This is due to the fact that T_{spec} is a *projected* temperature obtained by fitting a thermal model to the observed photon spectrum while T_{ew} fully exploit the *three dimensional* information carried by the gas particles an therefore defines a physical temperature. Therefore, T_{sl} gives a better approximation of T_{spec} and should be preferred when a cluster observation is simulated.

2.2.1 Isothermal

The simplest gas temperature profile is described by

$$T_{e,iso}(r) = C \tag{36}$$

where C is a constant positive number.

The advantages of this profile are:

- The overall gas temperature is directly given by the bremsstrahlung continuum.
- Isothermality is physically consistent with the derivation of the β-model density distribution which guarantees simple analytic cluster quantities.
- The integrals along the line of sight involved in the projected quantities S_x and ΔT_{CMB} become just functions of the electron density to the first and second power.

Unfortunately, clusters of galaxies are often far from isothermal. The temperature is often decreasing from the center to the outer regions, there are substructures and sometimes a cool cluster core is observed.

2.2.2 Polytropic model

A gas in a polytropic state with number density $n(r)$ fulfils

$$\frac{n(r)}{n_0} = \left(\frac{T(r)}{T_{e0}}\right)^{\gamma}, \tag{37}$$

where γ is the polytropic index. There are two important values: $\gamma = 1$ describes a isothermal gas, while $\gamma = \frac{5}{3}$ gives an adiabatic gas. Adiabatic gas does not exchange energy with the surrounding environment.

The temperature profile is therefore connected to the gas density profile

$$T_{e,poly}(r) = T_{e0}\left(\frac{n(r)}{n_0}\right)^{\gamma-1}. \tag{38}$$

If the electron density decreases outwards, the temperature will do the same. Figure 11 illustrates the situation in the case of a β-model electron distribution. Therefore, the polytropic profile catches a crucial feature of the observed temperature distribution and is able to model non-constant cluster temperature profiles.

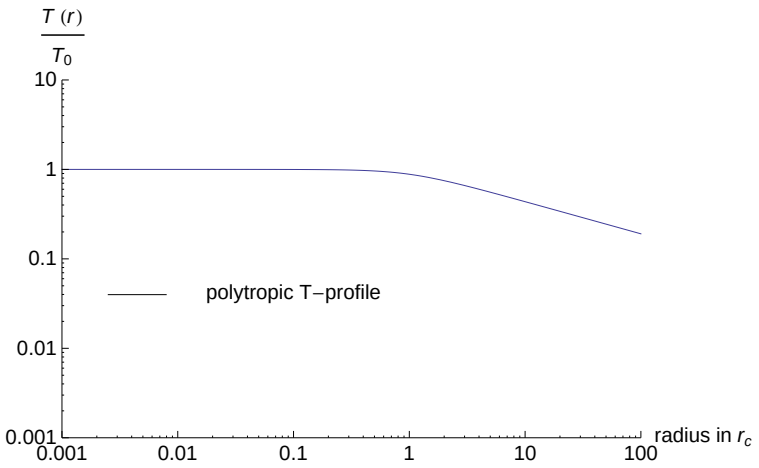

Figure 11: This is a normalized polytropic profile in the case of the β-model with parameters ($r_c = 1, \beta = 0.6$). Hence, the change of slope of the temperature profile happens also at $r = r_c$.

2.2.3 Vikhlinin temperature model

Accurate measurements reveal that the polytropic model is in fact a poor approximation of the temperature profiles at large radii. Moreover, there is a temperature decrement towards the center. Vikhlinin et al. [Vikhlinin 06] proposed a temperature profile that takes into account these observed features:

$$T_{e,Vik}(r) = T_0 \frac{(x + T_{min}/T_0)}{(x+1)} \frac{(r/r_t)^{-a}}{(1+(r/r_t)^b)^{\frac{c}{b}}}, \tag{39}$$

where $x = (r/r_{cool})^{a_{cool}}$. The first quotient describes the temperature behavior in the central cooling region. T_{min} characterizes the decrement due to the cool core, whereas r_{cool} gives the radius of this core. The second quotient represents the profile outside the cool core: a broken power law described by a, b and c with a change of slope at $r = r_t$, r_t is the truncation radius.

There are nine free parameters. Analysing 13 clusters, Vikhlinin et al. found an

average temperature profile, which is constraining the parameters

$$T(r) = 1.35 T_{ew} \frac{(x/0.045)^{1.9} + 0.45}{(x/0.045)^{1.9} + 1} \frac{1}{(1 + (x/0.6)^2)^{0.45}}, \tag{40}$$

where T_{ew} is the averaged emission weighted temperature and $x = r/r_{500}$ [6]. Using this averaged profile, we reduce the number of degrees of freedom in (39), whereas we change the powers $1.9 \to 2$ and $0.45 \to 0.5$:

$$T_{e,fit}(r) = T_0 \frac{(r/r_{cool})^2 + T_{min}/T_0}{(r/r_{cool})^2 + 1} \frac{1}{(1 + (r/r_t)^2)^{1/2}}. \tag{41}$$

To see its dependence on T, r_{cool} and other the other parameters, we plot the profile in figure 12 with different parameter configurations.

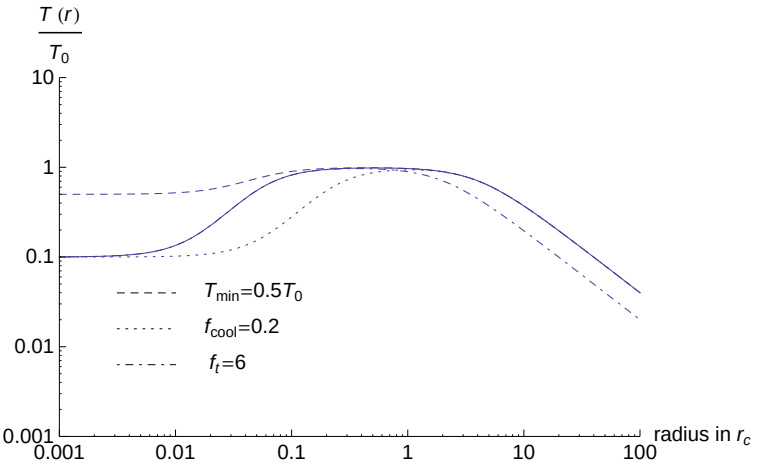

Figure 12: These are normalized Vikhlinin temperature profiles. The drawn through line is a profile with ($T_{min} = 0.1\,T_0, r_{cool}/r_c = 0.05, r_t/r_c = 4$). The other lines show how the profile changes if we vary a particular parameter.

[6] r_Δ is the radius at which the averaged density of the cluster inside this radius equals the over-density Δ given by

$$\Delta = \frac{3M(< r_\Delta)}{4\pi\rho_c r_\Delta^3},$$

where ρ_c is the critical density at cluster redshift.

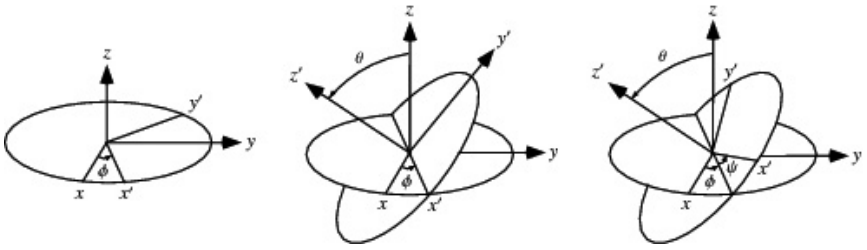

Figure 13: Any rotation can be described using three angles. From left to right, the most common definition of the Euler angles is illustrated. The (x, y, z)-system is the intrinsic frame, while the observer's frame (x', y', z') is aligned with the line of sight so that the observer is along the z'-direction. We see that this is achived by the first two rotations, the third rotation allows to orientate the x' and y' on the plane of the sky. From [MathWorld]

3 Projected quantities of ellipsoidal clusters

The goal of this section is to derive analytic expressions[7] for the X-ray surface brightness, see equation (5), and the SZ temperature decrement, see equation (10). For this purpose, we use combinations of the electron density models n_e and temperature profiles we introduced in the previous section. We will see that the integrand involved in the X-ray surface brightness map and the CMB-temperature decrement is proportional to a real positive power of the electron density and the temperature profile.

If it is possible to simplify these integrals, e.g. express them in terms of well known functions, it becomes much more easier to fit these models to the observational data. Although the fully numerical treatment is always possible, it costs more of computational power.

3.1 The geometry of clusters

First, we introduce quantities that help us to describe the intrinsic geometry of a cluster and the connection to its shape and orientation on the plane of the sky.

Projected ellipsoids In general, galaxy clusters can be assumed to have ellipsoidal shape, [Sereno 07] and references there in . More precisely, the electron density distribution of a cluster, which is responsible for the X-ray and SZE data, is constant on similar, concentric triaxial ellipsoids. In a Euclidean coordinate frame centered on the center of mass of a cluster and whose coordinate axes are aligned with its principal axes, the ICM profile can be described by one radial variable

$$\zeta^2 = e_1^2 x_{1,int}^2 + e_2^2 x_{2,int}^2 + e_3^2 x_{3,int}^2, \tag{42}$$

where $x_{i,int}$ is a vector component in this intrinsic coordinate frame, and e_i is the inverse of a scalelength l_c, in some units, along each axis. Without loss of generality, we can fix $e_3 = 1$. Therefore, this defines our scalelength.

When viewed from an arbitrary direction, quantities constant on similar ellipsoids project themselves on similar ellipses. To relate the intrinsic frame $x_{i,int}$ of the galaxy cluster to the observer's frame $x_{i,obs}$ we use the three Euler angles θ_{Eu}, ϕ_{Eu} and ψ_{Eu}.

Usually, we will assume that the $x_{3,obs}$-axis is aligned with the direction connecting the observer to the cluster center. A rotation through the first two angle is sufficient to achieve this. The third rotation angle ψ_{Eu} helps to adjust the $x_{1,obs}$ and $x_{2,obs}$ axes on the plane of the sky. It is the angle between the projection of the major axis

[7] Let us define 'analytic expression' so that we exclude integrals.

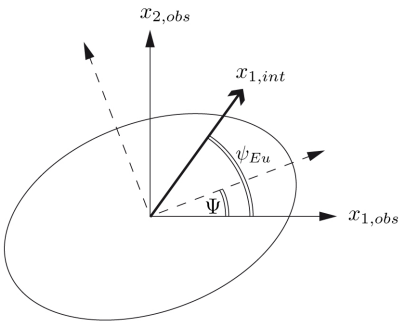

Figure 14: Comparison of the angles ψ_{Eu} and Ψ on the plane of the sky. The third Euler's angle gives the orientation of the major axis of the ellipsoid, here $x_{1,int}$, relative to the observer's frame. Ψ indicates the orientation of the axes of the projected ellipsoid (dashed arrows) relative to this frame. If the ellipsoid is axisymmetric, this angles will coincide.

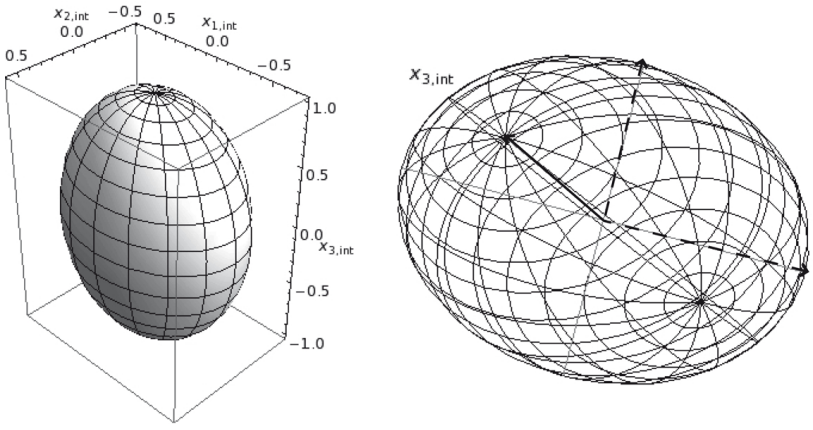

Figure 15: A comparison of a ellipsoidal cluster in the intrinsic coordinate frame x_int, left figure, and its projection on the plane of the sky, right figure. We see that the intrinsic axis $x_{3,int}$ does in general not correspond with the axes of the projected ellipsoid.

of the ellipsoid and the $x_{2,obs}$. Sometimes, we can assume that $x_{1,obs}$ and $x_{2,obs}$ are aligned with the axes of the projected ellipsoids. Otherwise, we introduce the angle Ψ to describe the rotation of the observer frame. Figure 14 compares these angles Ψ and ψ_{Eu} in the plane of the sky.

The axial ratio, the ratio between the major and minor axis of the projected ellipsoid on the plane of the sky, depends on the intrinsic geometry and on the orientation of the ellipsoid and is given as

$$e_p = \sqrt{\frac{j_\zeta + l_\zeta + \sqrt{(j_\zeta - l_\zeta)^2 + 4k_\zeta^2}}{j_\zeta + l_\zeta - \sqrt{(j_\zeta - l_\zeta)^2 + 4k_\zeta^2}}} \geq 1, \tag{43}$$

where j_ζ, k_ζ and l_ζ are in general defined as

$$\begin{aligned} 2j_\zeta \;=\; & e_1^2 + e_2^2 + (e_1^2 - e_2^2)(\cos 2\varphi(\cos^2\psi_{Eu}\cos^2\theta_{Eu} - \sin^2\psi_{Eu}) \\ & - \cos 2\theta_{Eu}\sin 2\varphi_{Eu}\sin 2\psi_{Eu}) \\ & + (2e_1^2e_2^2 - (e_1^2 + e_2^2)e_3^2)\cos^2\psi_{Eu}\,\sin^2\theta_{Eu}, \end{aligned} \tag{44}$$

$$\begin{aligned} 4k_\zeta &= (e_1^2 + e_2^2 - 2e_1^2e_2^2)\,\sin^2\theta_{Eu}\,\sin 2\varphi_{Eu} \\ &\quad -(e_1^2 - e_2^2)[2\cos\theta_{Eu}\cos 2\psi_{Eu}\sin 2\varphi_{Eu} \\ &\quad +(1+\cos^2\theta_{Eu})\cos 2\varphi_{Eu}\sin 2\psi_{Eu}], \end{aligned} \tag{45}$$

$$\begin{aligned} 2l_\zeta &= e_1^2 + e_2^2 + (-e_1^2 - e_2^2 + 2e_1^2e_2^2)\sin^2\psi_{Eu}\,\sin^2\theta_{Eu} \\ &\quad +(e_1^2 - e_2^2)\,(\cos 2\theta_{Eu}\sin 2\varphi_{Eu}\,\sin 2\psi_{Eu} \\ &\quad -\cos 2\varphi_{Eu}(\cos^2\psi_{Eu} - \cos^2\theta_{Eu}\sin^2\psi_{Eu})). \end{aligned} \tag{46}$$

One can show that the ellipticity does not depend on the third Euler's angle, which is obvious since this angle simply rotates the projected ellipsoid in the plane of the sky. Therefore, we can set $\psi_{Eu} = 0$ to obtain the simplified coefficients to express e_p:

$$j_\zeta(\psi_{Eu}=0) \equiv j = e_1^2\,e_2^2\,\sin^2\theta_{Eu} + e_1^2\,\cos^2\theta_{Eu}\,\cos^2\varphi_{Eu} + e_2^2\,\cos^2\theta_{Eu}\,\sin^2\theta_{Eu}, \tag{47}$$

$$k_\zeta(\psi_{Eu}=0) \equiv k = (e_1^2\,-\,e_2^2)\,\sin\varphi_{Eu}\,\cos\varphi_{Eu}\,\cos\theta_{Eu}, \tag{48}$$

$$l_\zeta(\psi_{Eu}=0) \equiv l = e_1^2\,\sin^2\varphi_{Eu}\,+\,e_2^2\,\cos^2\varphi_{Eu}. \tag{49}$$

The orientation of the projected ellipsoid relative to the axes of the observer's frame in terms of j_ζ, k_ζ and l_ζ is given as

$$\Psi = \frac{1}{2}\,\arctan\left(\frac{2k_\zeta}{j_\zeta + \sqrt{4k_\zeta^2 + (j_\zeta - l_\zeta)^2} - l_\zeta}\right). \tag{50}$$

If the observer's frame is orientated along the isophotes, (51) describes the angle between the projection of the $x_{3,int}$ axis and $x_{2,obs}$, see y' in the right panel of figure 13. This angle is ψ_{Eu} and can be expressed in terms of (47-49).

$$\Psi = \frac{1}{2}\,\arctan\left(\frac{2k}{j-l}\right). \tag{51}$$

It vanishes if the ellipsoid is axisymmetric.

Any length scale l_c, e.g. the core radius r_c in the case of the β-model, is projected onto the plane of the sky as

$$\theta_p = \theta_c\,\left(\frac{e_p}{e_1\,e_2}\right)^{1/2} f^{1/4}, \tag{52}$$

where $\theta_c = r_c/D_A$ is the angular core radius and θ_p its projected counterpart. D_A describes the angular diameter distance between observer and cluster and f is defined as

$$f = e_1^2\,\sin^2\theta_{Eu}\,\sin^2\varphi_{Eu}\,+\,e_2^2\,\sin^2\theta_{Eu}\,\cos^2\varphi_{Eu}\,+\,\cos^2\theta_{Eu}. \tag{53}$$

Moreover, one can define the elongation

$$e_\Delta \equiv \frac{r_p}{r_c}\,\sqrt{f} = \left(\frac{e_p}{e_1\,e_2}\right)^{1/2} f^{3/4}, \tag{54}$$

which is inversely proportional to the size of the ellipsoid along the line of sight. If $e_\Delta < 1$ the cluster is more elongated along the line of sight than wide in the plane of the sky, for example.

The elliptical radius on the plane of the sky, given by the projection of the ellipsoidal radius in the intrinsic coordinate frame, expressed in the observer's frame is given as

$$\xi^2 = (x_{1,obs}\cos\Psi + x_{2,obs}\sin\Psi)^2\frac{f}{e_\Delta^2} \tag{55}$$

$$+e_p^2(-x_{1,obs}\sin\Psi + x_{2,obs}\cos\Psi)^2\frac{f}{e_\Delta^2}. \tag{56}$$

where we rotated the observer coordinate frame with the angle Ψ. If the orientation of the intrinsic frame is known and we can do a rotation so that $\Psi = 0$, this expression simplifies as follows

$$\xi^2 = (x_{1,obs}^2 + e_p^2 x_{2,obs}^2)\frac{f}{e_\Delta^2}. \tag{57}$$

Alternatively, we can express ξ in terms of coefficients that describe the ellipticity of the projection:

$$\xi^2 = \frac{1}{f}\left(j_\zeta x_{1,obs}^2 + 2k_\zeta x_{1,obs}x_{2,obs} + l_\zeta x_{2,obs}^2\right). \tag{58}$$

These affinities can be sketched as follows: the coefficients j_ζ, k_ζ and l_ζ in equation (58) can be expressed through a symmetric 2×2 matrix which we can always diagonalize

$$\xi^2 = \frac{1}{f}\begin{pmatrix} x_{1,obs} & x_{2,obs}\end{pmatrix}\begin{pmatrix} j_\zeta & k_\zeta \\ k_\zeta & l_\zeta\end{pmatrix}\begin{pmatrix} x_{1,obs} \\ x_{2,obs}\end{pmatrix} \tag{59}$$

$$= \frac{1}{f}\begin{pmatrix} x_{1,obs} & x_{2,obs}\end{pmatrix}\begin{pmatrix} \lambda_1 & 0 \\ 0 & \lambda_2\end{pmatrix}\begin{pmatrix} x_{1,obs} \\ x_{2,obs}\end{pmatrix}. \tag{60}$$

Its eigenvalues λ_1 and λ_2 are the coefficients in (57). Therefore, the quotient λ_1/λ_2 gives e_p^2.

Projected spheroids Spheroids are axisymmetric ellipsoids. In the case of spheroidal models whose polar axis is aligned with $x_{3,int}$, we define $e_i \equiv (1/q_{int}, 1/q_{int}, 1)$ for a prolate cluster, $e_i \equiv (q_{int}, q_{int}, 1)$ for an oblate one. $q_{int} \geq 1$ describes the intrinsic axis ratio. The general quantities become more simple expressions. The elongations (54) reduce to

$$e_{\Delta,pro} = \frac{\sqrt{1-(1-q_{int}^2)\cos^2 i}}{q_{int}}, \tag{61}$$

$$e_{\Delta,obl} = \sqrt{1+\left(\frac{1}{q_{int}^2}\right)\cos^2 i}. \tag{62}$$

3.2 Projection effects

In astronomy, any intrinsic volume density, e.g. the electron density, can just be observed as its projection on the plane of the sky. If the ICM density profile is monotonically decreasing with radius, the connection between this intrinsic quantity $F_V(\zeta)$, where V denotes the volume density which is a function of the elliptical radius ζ, and its projection $F_S(\xi)$ is given by integration along the line of sight, see [Stark]:

$$F_S(\xi) = \int_{los} F_V(\zeta)\,dl = \frac{2}{\sqrt{f}}\int_\xi^\infty \frac{F_V(\zeta)\zeta}{\sqrt{\zeta^2-\xi^2}}\,d\zeta, \tag{63}$$

where the index S refers to the surface density and ξ is the ellipsoidal radius projected on the plane of the sky (57).

As introduced in section 1.2, physical effects like bremsstrahlung, line emission, Compton scattering and the deflection of light due to masses provide observable quantities like the X-ray brightness map of a cluster or gravitational lensing effects.

X-ray surface brightness and the temperature decrement are of fundamental importance in this thesis. Fitting a suitable model for $n_e(r)$ and $T(r)$ to the observational data gives parameters that describe the electron density. The central temperature decrement $\Delta T_{SZ,0}$ and the central surface brightness S_{X0} provide two further constraint. Moreover, particular combinations of these observations allow to constrain e.g. the elongation of a galaxy cluster along the line of sight.

The structures of both expressions are similar, see (5) and (10). If one compares the involved integrals, there is a fundamental form:

$$\int_{los} n_e^m T_e^b \, dl, \tag{64}$$

where the real powers m and b take into account

- the linear or quadratic dependence of the SZE or of the surface brightness on the electron density: n_e and n_e^2.
- the temperature profile
- the cooling function $\Lambda \propto T^\alpha$

and other properties of the gas that are described through a power of T or n. This is a motivation to give a catalogue of at least semi-analytic expression for combinations of different electron density models and temperature profiles to provide a well-arranged list and show model independent properties of these observable quantities.

It is obvious that we can get some information about the intrinsic shape of a cluster directly through analysing its projected shape if we assume that the cluster can be described by an ellipsoid. From X-ray surface brightness observations, we can estimate the orientation Ψ on the plane of the sky relative to the observers coordinate frame axes. If we compare the major and minor axes of the projected ellipse, the ellipticity e_p can be measured. Spectroscopic X-ray measurements reveal the projected temperature profile of the gas $T_e(r)$ and its metallicity $Z(r)$.

3.3 Isothermal and polytropic gas

Now, we want to calculate the projected quantities in the case of a polytropic temperature profile. The isothermal gas is just a limiting case of the polytropic gas. Therefore, any polytropic model will also include the isothermal case, $T_{e,iso} = T_{e,poly}|_{\gamma=1}$. The temperature profile of gas in a polytropic state is just a power law of the electron density: $T_{e,poly}(r) \propto n_e(r)^{\gamma-1}$. Thus, the surface brightness is given as

$$\begin{aligned} S_X &= \frac{1}{4\pi\,(1+z)^4}\int_{los} n_e^2 \Lambda(T_e, Z)\, dl \\ &= \frac{\tilde{\Lambda}(Z)}{4\pi\,(1+z)^4}\int_{los} n_e^2 T_e^{\alpha}\, dl \\ &= \frac{\tilde{\Lambda}(Z) T_{e0}^{\alpha}}{4\pi\, n_{e0}^{\alpha(\gamma-1)}\,(1+z)^4}\int_{los} n_e^2 n_e^{(\gamma-1)\alpha}\, dl \\ &= \frac{\Lambda(T_{e0}, Z)}{4\pi\, n_{e0}^{\alpha(\gamma-1)}\,(1+z)^4}\int_{los} n_e^{2+\alpha(\gamma-1)}\, dl, \end{aligned} \tag{65}$$

where we assumed in the first step that the metallicity Z is radial independent and the cooling function depends only on the radius through a power of the temperature, $\Lambda(T_e(r), Z) = \tilde{\Lambda}(Z)\, T^{\alpha}(r)$.

Under the same assumptions, the temperature decrement due to the SZ-effect simplifies as follows:

$$\begin{aligned} \frac{\Delta T_{SZ}}{T_{CMB}} &= f_{SZ}(\nu, T_e)\frac{\sigma_T k_B}{m_e c^2}\int_{los} n_e T_e\, dl \\ &= f_{SZ}(\nu, T_e)\frac{T_{e0}}{n_{e0}^{\gamma-1}}\frac{\sigma_T k_B}{m_e c^2}\int_{los} n_e n_e^{(\gamma-1)}\, dl \\ &= f_{SZ}(\nu, T_e)\frac{T_{e0}}{n_{e0}^{\gamma-1}}\frac{\sigma_T k_B}{m_e c^2}\int_{los} n_e^{\gamma}\, dl. \end{aligned} \tag{66}$$

If we compare the final expressions of S_X and ΔT_{SZ}, it is essential to calculate the integral of an arbitrary real positive power m of the electron density n_e,

$$\int_{los} n_e^m\, dl. \tag{67}$$

$m \to 2 + \alpha(\gamma - 1)$ gives the integral included in the X-ray surface brightness of a polytropic gas, $m \to \gamma$ describes the integrand of the temperature decrement. The prefactor is model independent, but depends on other assumptions. Numerical methods are more or less unavoidable, but our goal is to simplify the integrals as much as possible, e.g. to express them in terms of well known functions, like B, Γ and hypergeometric functions, see appendix C. Different density models will lead to different integrals. Therefore, we will spend a paragraph on each of them. At the end, we will conclude with a catalogue which reveals their differences and similarities, see appendix F.

3.3.1 β model

Let's first calculate the integral without the additional prefactors. The integration along the line of sight can be rewritten in terms of the elliptic radius as shown in equation (63).

$$\begin{aligned}
\int_{los} n_{e,\beta}^m \, dl &= \frac{2}{\sqrt{f}} \int_{\xi}^{\infty} n_{e,\beta}^m(\zeta) \frac{\zeta d\zeta}{\sqrt{\zeta^2 - \xi^2}} \\
&= \frac{2}{\sqrt{f}} \int_{\xi}^{\infty} n_{e0}^m \left(1 + (\zeta/r_c)^2\right)^{-\frac{3m\beta}{2}} \frac{\zeta d\zeta}{\sqrt{\zeta^2 - \xi^2}} \\
&= \frac{\sqrt{\pi}}{\sqrt{f}} \frac{\Gamma[-1/2 + 3m\beta/2]}{\Gamma[3m\beta/2]} n_{e0}^m \, r_c^{3m\beta} \left(\xi^2 + r_c^2\right)^{\frac{1}{2} - \frac{3m\beta}{2}} \\
&= \frac{\sqrt{\pi}}{\sqrt{f}} \frac{\Gamma[-1/2 + 3m\beta/2]}{\Gamma[3m\beta/2]} n_{e0}^m \, r_c \left(1 + \frac{\xi^2}{r_c^2}\right)^{\frac{1}{2} - \frac{3m\beta}{2}} . \qquad (68)
\end{aligned}$$

The third line follows from [G & R], equation 3.196.2, see appendix (A-16) if we assume that $3m\beta > 1$. Since $m \geq 1$, this is fulfilled if $\beta > 1/3$ which is usually always true.

The central value ($\xi = 0$) is given by:

$$\int_{los} n_{e,\beta}^m(0) \, dl = \frac{\sqrt{\pi}}{\sqrt{f}} \frac{\Gamma[-1/2 + 3m\beta/2]}{\Gamma[3m\beta/2]} n_{e0}^m \, r_c. \qquad (69)$$

In order to give the complete X-ray surface brightness is useful to split it into a central and radial dependent part. The central part contains all physical constants. It follows from (65) that the polytropic case demands a change of the power $m \to 2 + \alpha(\gamma - 1)$. With this substitution[8] we get:

$$S_X = S_{X0} \left(1 + \frac{\xi^2}{r_c^2}\right)^{\frac{1}{2} - \frac{3m\beta}{2}} = S_{X0} \left(1 + \frac{\xi^2}{r_c^2}\right)^{\frac{1}{2} - 3\beta - \frac{3}{2}\alpha(\gamma-1)\beta} , \qquad (70)$$

where all dimensional terms are included in

$$\begin{aligned}
S_{X0} &\equiv \frac{\tilde{\Lambda}(Z)}{4\pi \, (1+z)^4} \frac{\sqrt{\pi}}{\sqrt{f}} \frac{\Gamma[-1/2 + 3m\beta/2]}{\Gamma[3m\beta/2]} T_{e0}^{\alpha} \, n_{e0}^{\alpha(1-\gamma)+m} \, r_c \\
&= \frac{\tilde{\Lambda}(Z)}{4\pi \, (1+z)^4} \frac{\sqrt{\pi}}{\sqrt{f}} \frac{\Gamma[-1/2 + 3\beta + 3/2\alpha(\gamma-1)\beta]}{\Gamma[3\beta + 3/2\alpha(\gamma-1)\beta]} T_{e0}^{\alpha} \, n_{e0}^2 \, r_c. \qquad (71)
\end{aligned}$$

The temperature decrement can also be split into two parts. From (66), the change of the power is $m \to \gamma$.

$$\Delta T_{SZ} = \Delta T_0 \left(1 + \frac{\xi^2}{r_c^2}\right)^{\frac{1}{2} - \frac{3\gamma\beta}{2}} , \qquad (72)$$

where the central value is defined as

$$\Delta T_0 \equiv T_{CMB} \, f_{SZ}(\nu, T_e) \frac{\sigma_T k_B}{m_e c^2} \frac{\sqrt{\pi}}{\sqrt{f}} \frac{\Gamma[-1/2 + 3\gamma\beta/2]}{\Gamma[3\gamma\beta/2]} T_{e0} \, n_{e0} \, r_c. \qquad (73)$$

In the case of these central observable quantities of a polytropic β-model, the power m and the β-parameter appear always as a product and never alone. This means that they are degenerate. But m, respectively γ and also β are restricted on a limited interval and hence, also this degeneracy is limited. If the whole S_X-profile can be measured,

[8] In order to keep it clear we avoid this substitutions sometimes. But in such case the correct choice should be easily done.

this degeneracy is broken. Moreover, if an additional temperature measurement of the cluster is available, γ can be estimated independently.

3.3.2 2β model

In this case, we are not able to find a simpler form of the integral, due to the square root of the sum. To get a form that is similar to the β-model expression we introduce the following parameters: the total central electron density $n_{e0} \equiv n_{e0,1} + n_{e0,2}$, an electron density fraction $f_e \equiv n_{e0,1}/n_{e0}$, whereas we choose a definition with $n_{e0,1}$, and the fraction of the core radius $f_r = r_{c,1}/r_{c,2}$, which can be interpreted as the inner core radius in units of the overall scale length. Then:

$$\begin{aligned}
\int_{los} n_{e,2\beta}^m \, dl &= \frac{2}{\sqrt{f}} \int_\xi^\infty n_{e,2\beta}^m(\zeta) \frac{\zeta d\zeta}{\sqrt{\zeta^2 - \xi^2}} \\
&= \frac{2}{\sqrt{f}} \int_\xi^\infty \left(\frac{n_{e0,1}^2}{\left(1 + (\zeta/r_{c,1})^2\right)^{3\beta_1}} + \frac{n_{e0,2}^2}{\left(1 + (\zeta/r_{c,2})^2\right)^{3\beta_2}} \right)^{\frac{m}{2}} \frac{\zeta d\zeta}{\sqrt{\zeta^2 - \xi^2}} \\
&= \frac{2}{\sqrt{f}} \int_\xi^\infty \left(\frac{n_{e0}^2 (f_e)^2}{\left(1 + (\zeta/r_{c,1})^2\right)^{3\beta_1}} + \frac{n_{e0}^2 (1-f_e)^2}{\left(1 + (\zeta/r_{c,2})^2\right)^{3\beta_2}} \right)^{\frac{m}{2}} \frac{\zeta d\zeta}{\sqrt{\zeta^2 - \xi^2}}.
\end{aligned}$$

I change the variable of integration, $\zeta/r_{c,2} = x$, hence $d\zeta = r_{c,2} dx$. Thus:

$$\int_{los} n_{e,2\beta}^m \, dl = \frac{2 n_{e0}^2 \, r_{c,2}}{\sqrt{f}} \int_{\xi/r_{c,2}}^\infty \left(\frac{(f_e)^2}{\left(1 + (x/f_r)^2\right)^{3\beta_1}} + \frac{(1-f_e)^2}{(1+x^2)^{3\beta_2}} \right)^{\frac{m}{2}} \frac{x dx}{\sqrt{x^2 - \xi/r_{c,2}^2}}.$$

At last, the surface brightness is written as

$$\begin{aligned}
S_X &= \frac{\tilde{\Lambda}(Z)}{4\pi (1+z)^4} \frac{2}{\sqrt{f}} T_{e0}^\alpha \, n_{e0}^{\alpha(1-\gamma)+m} \, r_{c,2} \\
&\quad \times \int_{\xi/r_{c,2}}^\infty \left(\frac{(f_e)^2}{\left(1 + (x/f_r)^2\right)^{3\beta_1}} + \frac{(1-f_e)^2}{\left(1 + (x)^2\right)^{3\beta_2}} \right)^{\frac{m}{2}} \frac{x dx}{\sqrt{x^2 - \xi/r_{c,2}^2}}.
\end{aligned} \tag{74}$$

A polytropic gas is given by $m \to 2 + \alpha(\gamma - 1)$. In the case of $m = 2$, that is if the gas is isothermal, the model simplifies strongly and reduces to the sum of two β-models, which we can integrate one after another.

$$\begin{aligned}
S_X &= \frac{\tilde{\Lambda}(Z)}{4\pi (1+z)^4} \frac{2}{\sqrt{f}} T_{e0}^\alpha \, n_{e0}^{\alpha(1-\gamma)+m} \, r_{c,2} \\
&\quad \times \left[\frac{\Gamma[-1/2 + 3m\beta_1/2]}{\Gamma[3m\beta_1/2]} {f_e}^2 \left(1 + \frac{\xi^2}{{f_r}^2 {r_{c,2}}^2}\right)^{(1-3m\beta_1)/2} \right. \\
&\quad \left. + \frac{\Gamma[-1/2 + 3m\beta_2/2]}{\Gamma[3m\beta_2/2]} (1-f_e)^2 \left(1 + \frac{\xi^2}{{r_{c,2}}^2}\right)^{(1-3m\beta_2)/2} \right].
\end{aligned} \tag{75}$$

The temperature decrement is ($m \to \gamma$)

$$\begin{aligned}\Delta T_{SZ} &= T_{CMB}\, f_{SZ}(\nu, T_e) \frac{\sigma_T k_B}{m_e c^2} \frac{2}{\sqrt{f}} T_{e0}\, n_{e0}\, r_{c,2} \\ &\times \int_{\xi/r_{c,2}}^{\infty} \left(\frac{(f_e)^2}{\left(1+(x/f_r)^2\right)^{\frac{3\beta_1}{2}}} + \frac{(1-f_e)^2}{\left(1+(x)^2\right)^{\frac{3\beta_2}{2}}} \right)^{\frac{\gamma}{2}} \frac{x dx}{\sqrt{x^2 - \xi/r_{c,2}^2}}. \end{aligned} \tag{76}$$

3.3.3 PA-model

Starting from the model with the additional cusp, we get:

$$\begin{aligned}\int_{los} n_{e,PA}^m\, dl &= \frac{2}{\sqrt{f}} \int_{\xi}^{\infty} n_{e,PA}^m(\zeta) \frac{\zeta d\zeta}{\sqrt{\zeta^2 - \xi^2}} \\ &= \frac{2}{\sqrt{f}} \int_{\xi}^{\infty} n_{e0}^m \left(\zeta/r_c\right)^{\frac{-m\eta}{2}} \left(1+(\zeta/r_c)^2\right)^{-\frac{3m\beta}{2}+\frac{m\eta}{4}} \frac{\zeta d\zeta}{\sqrt{\zeta^2 - \xi^2}} \\ &= \frac{\sqrt{\pi}}{\sqrt{f}} \frac{\Gamma[-1/2 + 3m\beta/2]}{\Gamma[3m\beta/2]} n_{e0}^m \frac{r_c^{3m\beta}}{\xi^{3m\beta-1}} \\ &\quad \times {}_2F_1\left[-\frac{1}{4}m(\eta - 6\beta), -\frac{1}{2}(1-3m\beta), \frac{3m\beta}{2}, -\frac{r_c^2}{\xi^2} \right]. \end{aligned} \tag{77}$$

The last line is given by [G & R], equation 3.197.2, see appendix, if we assume that $3m\beta > 1$ and $m\eta < 4$, that is generally fulfilled[9]. The PA-model $n_{e,PA}^m(\zeta)$ has a cusp at $\zeta = 0$. The integral $\int_{los} n_{e,PA}^m\, dl$ or in particular the last argument in ${}_2F_1$ seems to diverge if $\xi \to 0$. A way to find a more useful expression is by using the Euler hypergeometric transformations (A-6). Starting from (77), we get:

$$\begin{aligned}\int_{los} n_{e,PA}^m\, dl &= \frac{\sqrt{\pi}}{\sqrt{f}} \frac{\Gamma[-1/2 + 3m\beta/2]}{\Gamma[3m\beta/2]} n_{e0}^m \frac{r_c^{3m\beta}}{\xi^{3m\beta-1}} \\ &\quad \times {}_2F_1\left[-\frac{1}{4}m(\eta - 6\beta), -\frac{1}{2}(1-3m\beta), \frac{3m\beta}{2}, -\frac{r_c^2}{\xi^2} \right] \\ &= \frac{\sqrt{\pi}}{\sqrt{f}} \frac{\Gamma[-1/2 + 3m\beta/2]}{\Gamma[3m\beta/2]} n_{e0}^m \frac{r_c^{3m\beta}}{\xi^{3m\beta-1}} \left(1 + \frac{r_c^2}{\xi^2}\right)^{-\frac{3n\beta}{2}+\frac{1}{2}} \\ &\quad \times {}_2F_1\left[\frac{m\eta}{4}, -\frac{1}{2}(1-3m\beta), \frac{3m\beta}{2}, \frac{-r_c^2/\xi^2}{-r_c^2/\xi^2 - 1} \right] \end{aligned}$$

[9] e.g. [P & A 02] estimate a PA-model to describe A1413 with parameters $\beta = 0.69$ and $\eta = 2 \cdot 0.68$ that fulfill $3m\beta = 3 \cdot 0.69 > 1$ with $m = 1$ and $m\eta = 4 \cdot 0.68 < 4$ with $m = 2$, the chosen m represent the extreme values in the isothermal case.

$$
\begin{aligned}
&= \frac{\sqrt{\pi}}{\sqrt{f}}\frac{\Gamma[-1/2+3m\beta/2]}{\Gamma[3m\beta/2]} n_{e0}^m r_c^{3m\beta} (\xi^2)^{-\frac{3m\beta}{2}+\frac{1}{2}} \left(1+\frac{r_c^2}{\xi^2}\right)^{-\frac{3m\beta}{2}+\frac{1}{2}} \\
&\quad \times {}_2F_1\left[\frac{m\eta}{4}, -\frac{1}{2}(1-3m\beta), \frac{3m\beta}{2}, \frac{r_c^2}{r_c^2+\xi^2}\right] \\
&= \frac{\sqrt{\pi}}{\sqrt{f}}\frac{\Gamma[-1/2+3m\beta/2]}{\Gamma[3m\beta/2]} n_{e0}^m r_c^{3m\beta} (r_c^2+\xi^2)^{\frac{1}{2}-\frac{3m\beta}{2}} \\
&\quad \times {}_2F_1\left[\frac{m\eta}{4}, -\frac{1}{2}(1-3m\beta), \frac{3m\beta}{2}, \frac{r_c^2}{r_c^2+\xi^2}\right]. \qquad (78)
\end{aligned}
$$

This should be the preferred formulation of the initial integral because it is good to handle at the center. When $\xi \to 0$, we get:

$$
\int_{los} n_{e,PA}^m(0)\, dl = \frac{\sqrt{\pi}}{\sqrt{f}}\frac{\Gamma[-1/2+3m\beta/2]}{\Gamma[3m\beta/2]} n_{e0}^m r_c \; {}_2F_1\left[\frac{m\eta}{4}, \frac{1}{2}(3m\beta-1), \frac{3m\beta}{2}, 1\right]. \qquad (79)
$$

A feature of the hypergeometric function ${}_2F_1[a,b,c;z]$, as explained in the appendix, is the fact that it is always finite if the absolute value of the last argument z is smaller than 1. When $z=1$, it is only finite if the other arguments fulfill $a+b<c$. If we take a look at (78) and (79), we see that a problem occurs if $\xi \to 0$. The condition for avoiding an infinite integral is given by

$$
\begin{aligned}
\frac{m\eta}{4} + \frac{1}{2}(3m\beta-1) &< \frac{3m\beta}{2} && (80)\\
\Leftrightarrow \frac{m\eta}{4} &< \frac{1}{2} && (81)\\
\Leftrightarrow m\eta &< 2 && (82)
\end{aligned}
$$

Therefore, we have to limit the η parameter even more in order to calculate the integral in (77). This is not always fulfilled, for example in the case of the surface brightness $m=2$ and $\eta > 1$, that is also mentioned in [P & A 02].

An other way to get the central value is as follows[10]. We expand the integral for small dimensionless $x \equiv \xi/r_c \ll 1$ around 0 and assume that x is real.

$$
\begin{aligned}
I_{PA}(x) \;\simeq\; & x^{-`m\eta 2}\left(\frac{n_{e0}^m\sqrt{\pi} r_c \Gamma\left[-1/2+m\eta/4\right] x}{\sqrt{f}\Gamma\left[m\eta/4\right]}\right. \\
& \left. + \frac{m n_{e0}^m \sqrt{\pi} r_c (\eta-6\beta)\Gamma\left[(-3/2+m\eta/4)\right] x^3}{4\sqrt{f}\Gamma\left[-1+m\eta/4\right]} + O[x]^4\right) \\
& + \left(\frac{n_{e0}^m r_c \Gamma\left[1/2-m\eta/4\right]\Gamma\left[-1/2+3m\beta/2\right]}{\sqrt{f}\Gamma\left[-m\eta/4+3m\beta/2)\right]}\right. \\
& \left. + \frac{n_{e0}^m r_c \Gamma\left[-1/2-m\eta/4\right]\Gamma\left[1/2+3m\beta/2\right] x^2}{2\sqrt{f}\Gamma\left[-m\eta/4-3m\beta/2)\right]} + O[x]^4\right).
\end{aligned} \qquad (83)
$$

The lowest order term (third line) is independent of x. It describes the value of $I_{PA}(\xi)$ at the very center:

$$
\lim_{x\to 0} I_{PA}(x) = \frac{1}{\sqrt{f}}\frac{\Gamma[1/2-m\eta/4]\Gamma[3m\beta/2-1/2]}{\Gamma[-m\eta/4+3m\beta/2]} n_{e0}^m\, r_c. \qquad (84)
$$

Transformations reveal that equation (84) is identical to (79) if $m\eta < 2$, see (A-9).

[10] Of course, a integration at the center would lead to the same result: $\lim_{x\to 0} I_{PA}(x) = \int_{los} n_{e,PA}^m(0)\, dl$.

We conclude that the X-ray surface brightness of this model is given by

$$\begin{aligned} S_X &= \frac{\tilde{\Lambda}(Z)}{4\pi\,(1+z)^4}\frac{\sqrt{\pi}}{\sqrt{f}}\frac{\Gamma[-1/2+3m\beta/2]}{\Gamma[3m\beta/2]}T_{e0}^{\alpha}n_{e0}^{\alpha(1-\gamma)+m} \\ &\quad \times r_c^{3m\beta}(r_c^2+\xi^2)^{\frac{1}{2}-\frac{3m\beta}{2}}\,{}_2F_1\left[\frac{m\eta}{4},-\frac{1}{2}(1-3m\beta),\frac{3m\beta}{2},\frac{r_c^2}{r_c^2+\xi^2}\right] \qquad (85) \\ &= \frac{\tilde{\Lambda}(Z)}{4\pi\,(1+z)^4}\frac{\sqrt{\pi}}{\sqrt{f}}\frac{\Gamma[-1/2+3m\beta/2]}{\Gamma[3m\beta/2]}T_{e0}^{\alpha}n_{e0}^{2}r_c \\ &\quad \times\left(1+\frac{\xi^2}{r_c^2}\right)^{\frac{1}{2}-\frac{3m\beta}{2}}\,{}_2F_1\left[\frac{m\eta}{4},-\frac{1}{2}(1-3m\beta),\frac{3m\beta}{2},\frac{r_c^2}{r_c^2+\xi^2}\right], \qquad (86) \end{aligned}$$

where we isolated the dimensional quantities in the first line of equation (86). A substitution $m \to 2+\alpha(\gamma-1)$ gives the polytropic case. If $\xi = 0$, we get:

$$\begin{aligned} S_{X0} &= \frac{\tilde{\Lambda}(Z)}{4\pi\,(1+z)^4}\frac{\sqrt{\pi}}{\sqrt{f}}\frac{\Gamma[-1/2+3m\beta/2]}{\Gamma[3m\beta/2]}T_{e0}^{\alpha}n_{e0}^{\alpha(1-\gamma)+m}r_c \\ &\quad \times\,{}_2F_1\left[\frac{m\eta}{4},-\frac{1}{2}(1-3m\beta),\frac{3m\beta}{2},1\right]. \qquad (87) \end{aligned}$$

Equivalently, the central value, motivated by (84), is given by

$$S_{X0} = \frac{\tilde{\Lambda}(Z)}{4\pi\,(1+z)^4}\frac{1}{\sqrt{f}}\frac{\Gamma[1/2-m\eta/4]\Gamma[3m\beta/2-1/2]}{\Gamma[-m\eta/4+3m\beta/2]}T_{e0}^{\alpha}n_{e0}^{\alpha(1-\gamma)+m}\,r_c. \qquad (88)$$

The temperature decrement follows in a similar manner:

$$\begin{aligned} \Delta T_{SZ} &= T_{CMB}\,f_{SZ}(\nu,T_e)\frac{\sigma_T k_B}{m_e c^2}\frac{\sqrt{\pi}}{\sqrt{f}}\frac{\Gamma[-1/2+3\gamma\beta/2]}{\Gamma[3\gamma\beta/2]}T_{e0}\,n_{e0}r_c\left(1+\frac{\xi^2}{r_c^2}\right)^{\frac{1}{2}-\frac{3\gamma\beta}{2}} \\ &\quad \times{}_2F_1\left[\frac{\gamma\eta}{4},-\frac{1}{2}(1-3\gamma\beta),\frac{3\gamma\beta}{2},\frac{r_c^2}{r_c^2+\xi^2}\right]. \end{aligned} \qquad (89)$$

Its central value is

$$T_0 = T_{CMB}\,f_{SZ}(\nu,T_e)\frac{\sigma_T k_B}{m_e c^2}\frac{1}{\sqrt{f}}\frac{\Gamma[1/2-m\eta/4]\Gamma[3m\beta/2-1/2]}{\Gamma[-m\eta/4+3m\beta/2]}T_{e0}\,n_{e0}\,r_c. \qquad (90)$$

As usual, a polytropic gas requests $m \to \gamma$.

The results at the center are restricted to $m\eta < 2$.

3.3.4 VE-model

The increasing complexity of the models leads to difficult tasks, if we want to simplify the integrals along the line of sight. Therefore, we focus on the Vikhlinin-Ettori model and ignore the more complex Vikhlinin-model. Moreover, assumptions have to be done and particular solutions have to be considered.

According to [G & R], equation 3.259.3, see appendix, there is a solution of the integral along the line of sight if

- we concentrate our attention on the central value ($\xi = 0$),
- we assume that the radius r_s at which the slope in the outer regions is changing and the core radius $r_c \neq r_s$ are of the same power ($\gamma = 2$),

- the parameters are fixed by particular limits[11]: $m\eta < 2$ and $3m\beta + \epsilon/2 > 1$,
- we substitute $r/r_c \to x$ and $dR \to r_c\, dx$.

Under these conditions, we get

$$\begin{aligned}
\int_{los} n_{e,VE}(0)^m\, dl &= \frac{2}{\sqrt{f}} \int_0^\infty n_{e,VE}^m(\zeta) d\zeta \\
&= \frac{2}{\sqrt{f}} \int_0^\infty n_{e0}\, (\zeta/r_c)^{-\frac{\eta}{2}}\, (1 + (\zeta/r_c)^2)^{-\frac{3\beta}{2}+\frac{\eta}{4}}\, (1 + (\zeta/r_s)^\kappa)^{-\frac{\epsilon}{2\kappa}}\, d\zeta \\
&= \frac{1}{\sqrt{f}} \frac{\Gamma[1/2 - m\eta/4]\Gamma[3m\beta/2 + m\epsilon/4 - 1/2]}{\Gamma[-m\eta/4 + 3m\beta/2 + \epsilon m/4]} n_{e0}^m r_c \\
&\quad \times {}_2F_1\left[\frac{m\epsilon}{4}, \frac{1}{4}(2 - m\eta), \frac{1}{4}(6m\beta - m\eta + m\epsilon), 1 - (\frac{r_c}{r_s})^2\right].
\end{aligned} \tag{91}$$

Thus, the central values of X-ray surface brightness and temperature decrement are given by

$$\begin{aligned}
S_{X0} &= \frac{\tilde{\Lambda}(Z)}{4\pi\,(1+z)^4} \frac{1}{\sqrt{f}} \frac{\Gamma[1/2 - m\eta/4]\Gamma[3m\beta/2 + m\epsilon/4 - 1/2]}{\Gamma[-m\eta/4 + 3m\beta/2 + \epsilon m/4]} \\
&\quad \times T_{e0}^\alpha\, n_{e0}^2\, r_c \\
&\quad \times {}_2F_1\left[\frac{m\epsilon}{4}, \frac{1}{4}(2 - m\eta), \frac{1}{4}(6m\beta - m\eta + m\epsilon), 1 - (\frac{r_c}{r_s})^2\right],
\end{aligned} \tag{92}$$

where $m \to 2 + \alpha(\gamma - 1)$ and

$$\begin{aligned}
T_{SZ,0} &= T_{CMB}\, f_{SZ}(\nu, T_e) \frac{\sigma_T k_B}{m_e c^2} \frac{1}{\sqrt{f}} \frac{\Gamma[1/2 - \gamma\eta/4]\Gamma[3\gamma\beta/2 + \gamma\epsilon/4 - 1/2]}{\Gamma[-\gamma\eta/4 + 3\gamma\beta/2 + \epsilon\gamma/4]} \\
&\quad \times T_{e0}\, n_{e0}\, r_c \\
&\quad \times {}_2F_1\left[\frac{\gamma\epsilon}{4}, \frac{1}{4}(2 - \gamma\eta), \frac{1}{4}(6\gamma\beta - \gamma\eta + \gamma\epsilon), 1 - (\frac{r_c}{r_s})^2\right],
\end{aligned} \tag{93}$$

where we choose $m \to \gamma$.

The general X-ray surface brightness is given by

$$\begin{aligned}
S_X &= \frac{\tilde{\Lambda}(Z) T_{e0}^\alpha}{4\pi\, n_{e0}^{\alpha(\gamma-1)}\, (1+z)^4} \int_{los} n_e^m\, dl \\
&= \frac{\tilde{\Lambda}(Z) T_{e0}^\alpha}{4\pi\, n_{e0}^{\alpha(\gamma-1)}\, (1+z)^4} \frac{2}{\sqrt{f}} \\
&\quad \times \int_\xi^\infty n_{e0}^m\, (\zeta/r_c)^{-\frac{m\eta}{2}}\, (1 + (\zeta/r_c)^2)^{-\frac{3m\beta}{2}+\frac{m\eta}{4}}\, (1 + (\zeta/r_s)^\kappa)^{-\frac{m\epsilon}{2\kappa}}\, \frac{\zeta d\zeta}{\sqrt{\zeta^2 - \xi^2}} \\
&= \frac{\tilde{\Lambda}(Z) T_{e0}^\alpha}{4\pi\, (1+z)^4} \frac{2}{\sqrt{f}} n_{e0}^2\, r_c \\
&\quad \times \int_{\xi/r_c}^\infty x^{-\frac{m\eta}{2}} (1 + x^2)^{-\frac{3m\beta}{2}+\frac{m\eta}{4}}\, (1 + (x/f_s)^\kappa)^{-\frac{m\epsilon}{2\kappa}}\, \frac{x dx}{\sqrt{x^2 - (\xi/r_c)^2}},
\end{aligned} \tag{94}$$

[11] Here, we have a very strong limit on η, similar to the PA-model at the center. Unfortunately, a more general treatment seems not possible.

where $f_s = r_s/r_c$. The temperature decrement is

$$\frac{\Delta T_{SZ}}{T_{CMB}} = f_{SZ}(\nu, T_e)\frac{\sigma_T k_B}{m_e c^2}\frac{2}{\sqrt{f}} T_{e0}\, n_{e0}\, r_c \tag{95}$$

$$\times \int_{\xi/r_c}^{\infty} x^{-\frac{\gamma\eta}{2}} (1+x^2)^{-\frac{3\gamma\beta}{2}+\frac{\gamma\eta}{4}} \left(1+(x/f_s)^{\kappa}\right)^{-\frac{\gamma\epsilon}{2\kappa}} \frac{x dx}{\sqrt{x^2-(\xi/r_c)^2}}. \tag{96}$$

3.3.5 Checking the results

Due to the similarities of the different models, an adequate choice of the parameters should reproduce the results of the simpler models, see section 2.1.6.

If $\epsilon \to 0$, the VE-model reduces to the PA-model:

$$\begin{aligned}
[\int_{los} n^m_{e,VE}(0)\, dl]|_{\epsilon\to 0} &= \frac{1}{\sqrt{f}}\frac{\Gamma[1/2 - m\eta/4]\Gamma[3m\beta/2 + 0 - 1/2]}{\Gamma[-m\eta/4 + 3m\beta/2 + 0]} n^m_{e0} r_c \\
&\quad \times {}_2F_1\left[0, \frac{1}{4}(2-m\eta), \frac{1}{4}(6m\beta - m\eta + m\epsilon, 1 - (\frac{r_c}{r_s})^2\right] \\
&= \frac{1}{\sqrt{f}}\frac{\Gamma[1/2 - m\eta/4]\Gamma[3m\beta/2 - 1/2]}{\Gamma[-m\eta/4 + 3m\beta/2)]} n^m_{e0}\, r_c \\
&= \int_{los} n^m_{e,PA}(0)\, dl,
\end{aligned}$$

since ${}_2F_1[0, a, b; z] = 1$.

Taking the two limits of two parameters, $\epsilon \to 0$ and $\eta \to 0$, we recognize the central value of the integrated β-model:

$$\begin{aligned}
[\int_{los} n^m_{e,VE}(0)\, dl]|_{\eta\to 0,\epsilon\to 0} &= \frac{1}{\sqrt{f}}\frac{\Gamma[1/2]\Gamma[3m\beta/2 - 1/2]}{\Gamma[3m\beta/2]} n^m_{e0} r_c \left(\frac{r_c}{r_s}\right)^{-1} \\
&\quad \times {}_2F_1\left[\frac{3}{2}m\beta, \frac{1}{2}, \frac{3}{2}m\beta, 1 - (\frac{r_c}{r_s})^{-2}\right] \\
&= \frac{\sqrt{\pi}}{\sqrt{f}}\frac{\Gamma[-1/2 + 3m\beta/2]}{\Gamma[3m\beta/2]} n^m_{e0}\, r_c \\
&= \int_{los} n^m_{e,\beta}(0)\, dl.
\end{aligned}$$

In the third equation we used the alternative representation derived through the hypergeometric transformations, see equation (91). Further, ${}_2F_1[a, 1/2, b, 1 - (r_c/r_s)^{-2}] = r_c/r_s$ if $a, b > 0$ and $\Gamma[1/2] = \sqrt{\pi}$.

3.4 General temperature profile

To improve our models of the projected quantities, it is time to include more accurate temperature profiles, e.g. the Vikhlinin temperature profile $T_{e,Vik}$ and its simplified counterpart $T_{e,fit}$, both introduced in section 2.2.3. In most of the polytropic cases, it was possible to simplify the integrals along the line of sight. If we include $T_{e,Vik}$, the integrand is more complex. Hence, it makes sense to start with the fitted simplified temperature profile $T_{e,fit}$ and the β-model to describe the electron density profile to keep the integration as simple as possible.

If we recall equation (64), we have to solve

$$\int_{los} n_{e,\beta}^m T_{e,fit}^b \, dl = \frac{2}{\sqrt{f}} \int_{\xi}^{\infty} n_{e,\beta}^m(\zeta) \, T_{e,Vik}^b(\zeta) \frac{\zeta d\zeta}{\sqrt{\zeta^2 - \xi^2}}, \tag{97}$$

beside some prefactors. If $m \to 1$ and $b \to 1$, we get the temperature decrement, if $m \to 2$ and $b \to \alpha$, it gives the X-ray surface brightness. We write down the full expression and its central value:

$$\begin{aligned}
\int_{los} n_{e,\beta}^m T_{e,fit}^b \, dl \quad &= \quad \frac{2}{\sqrt{f}} \int_{\xi}^{\infty} n_{e,\beta}^m(\zeta) \, T_{e,fit}^b(\zeta) \frac{\zeta d\zeta}{\sqrt{\zeta^2 - \xi^2}} \\
&= \quad \frac{2}{\sqrt{f}} \int_{\xi}^{\infty} \zeta \, d\zeta \, (\xi^2 - \zeta^2)^{-1/2} \, n_{e0}^m \left(1 + (\zeta/r_c)^2\right)^{-\frac{3m\beta}{2}} \\
&\quad \times T_0^b \frac{\left(T_{min}/T_0 + (\zeta/r_{cool})^2\right)^b}{(1 + (\zeta/r_{cool})^2)^b \left((1 + (\zeta/r_t)^2)^{1/2}\right)^b} \\
\left[\int_{los} n_{e,\beta}^m T_{e,fit}^b \, dl\right] |_{\xi \to 0} \quad &= \quad \frac{2T_0^b}{\sqrt{f}} \int_0^{\infty} d\zeta \, n_{e0}^m \left(1 + (\zeta/r_c)^2\right)^{-\frac{3m\beta}{2}} \\
&\quad \times \frac{\left(T_{min}/T_0 + (\zeta/r_{cool})^2\right)^b}{(1 + (\zeta/r_{cool})^2)^b \left((1 + (\zeta/r_t)^2)^{1/2}\right)^b}.
\end{aligned} \tag{98}$$

We will focus on the center, $\xi \to 0$. Moreover, we restrict the integral to the relevant cases, X-ray surface brightness and SZ temperature decrement, to simplify the problem.

In case of ΔT_{SZ} ($m \to 1$ and $b \to 1$), there is a unmanageable solution to the integral, computed by Mathematica. The surface brightness S_X is more difficult to calculate since, in the case of a cooling function $\Lambda(T_e) \propto T_e^{1/2}$, the power is given by $b = \alpha = 1/2$.

However, in order to get an analytic solution, we tried to derive a temperature profile from $T_{e,fit}(r)$ that leads to easier integrals but has the same features as $T_{e,fit}(r)$: A cool core at the center with a non-zero depth and width and a decreasing temperature at large radii. Our first idea was inspired by the PA-model. This model that describes a electron density distribution has a central cusp to mimic the high densities in the center of particular clusters. We assumed that this profile describes the temperature profile if we flip its cusp so that it mimics the cool core. This would lead to a simpler integrand. Unfortunately, to avoid zero temperature at the center, adding a constant is necessary. This results in a integration that is as difficult as in the case of the other $T(r)$-model.

The original profile $T_{e,Vik}(r)$ has highly degenerate parameters. We can use this ambiguity to modify it in a way that the integral is analytically solvable. If we set $T_{e,fit}(r) \to \tilde{T}_{e,fit}(r) = T_{e,fit}^2(r)$, we reduce the integrand to the same expression as in the case of the temperature decrement, which is solvable. But does this modified profile still contain the requested features? As shown in an example in figure 16, there is a set of parameters that satisfies $T_{e,fit}(r) \sim \tilde{T}_{e,fit}(r)$. Therefore, this seems to be an alternative profile.

Several facts suggest that including an accurate but complex temperature profile like $T_{e,Vik}$ or $T_{e,fit}$ is a good point to stop searching for analytic expressions and to start integrating numerically:

- Using $\tilde{T}_{e,fit}(r)$, the calculated integral and therefore S_X and ΔT_{SZ} become very

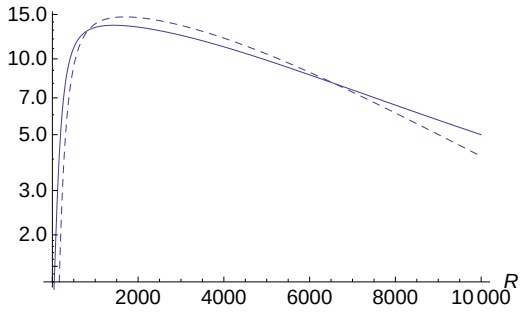

Figure 16: A comparison of $T_{e,fit}(R)$ (drawn though line) and $\tilde{T}_{e,fit}(R)$ (dashed line). Both profiles have the same parameters with exception of the truncation radius r_t. In addition, $\tilde{T}_{e,fit}(R)$ is scaled with a suitable factor. We see that features like a cool core an the slope at large radii are similar. The units are arbitrarily chosen.

complex and confusing expressions that are far beyond the beauty of a isothermal β-model. It's hard to see an advantage.

- Although we can use $\tilde{T}_{e,fit}(r)$ to simplify the X-ray surface brightness integral, we still have to include $T_{e,fit}(r)$ to calculate the temperature decrement. If we use two different temperature models performing a multi wavelength analysis, the procedure will not be self-consistent.

- The Vikhlinin temperature profile in its most general form we introduced, $T_{Vik}(r)$, can't be included in a analytic treatment.

- There seems to be a disproportionality if we use such an accurate temperature profile combined with the simple β-model which is based on a constant temperature profile. But including better density profiles would unavoidable lead to a preference of numerical methods.

In the following sections, we will give the X-ray surface brightness and temperature decrement in terms of an dimensional prefactor and an integral with a non-dimensional integrand. This leads to expressions similar to the polytropic case.

3.4.1 β model

The Vikhlinin temperature profile adds two new length scales, r_{cool} and r_t, into the expressions for the observable quantities. Nevertheless, the core radius is still the best choice for the overall length scale. Therefore, we write the other radii in units of r_c: $f_{cool} = r_{cool}/r_c$ and $f_t = r_t/r_c$. Moreover, to keep the amount of free parameters low,

we use the averaged profile $T_{e,fit}(r)$. Thus, the surface brightness can be written as:

$$\begin{aligned}
S_X &= \frac{\tilde{\Lambda}(Z)}{4\pi\,(1+z)^4}\frac{2}{\sqrt{f}}\int_\xi^\infty n_{e,\beta}^2(\zeta)\,T_{e,vik}^\alpha(\zeta)\,\frac{\zeta d\zeta}{\sqrt{\zeta^2-\xi^2}} \\
&= \frac{\tilde{\Lambda}(Z)}{4\pi\,(1+z)^4}\frac{2}{\sqrt{f}}\int_\xi^\infty n_{e0}^2[1+(\zeta/r_c)^2]^{-3\beta} \\
&\quad \times T_0^\alpha\frac{[T_{min}/T_0+(\zeta/r_{cool})^2]^\alpha}{[1+(\zeta/r_{cool})^2]^\alpha}\frac{1}{[1+(\zeta/r_t)^2]^{\alpha/2}}\frac{\zeta d\zeta}{\sqrt{\zeta^2-\xi^2}} \\
&= \frac{\tilde{\Lambda}(Z)}{4\pi\,(1+z)^4}\frac{2n_{e0}^2\,T_0^\alpha}{\sqrt{f}}\int_\xi^\infty[1+(\zeta/r_c)^2]^{-3\beta} \\
&\quad \times\frac{[T_{min}/T_0+f_{cool}^{-2}(\zeta/r_c)^2]^\alpha}{[1+f_{cool}^{-2}(\zeta/r_c)^2]^\alpha}\frac{1}{[1+f_t^{-2}(\zeta/r_c)^2]^{\alpha/2}}\frac{\zeta d\zeta}{\sqrt{\zeta^2-\xi^2}} \\
&= \frac{\tilde{\Lambda}(Z)}{4\pi\,(1+z)^4}\frac{2n_{e0}^2\,T_0^\alpha}{\sqrt{f}}\int_{\xi/r_c}^\infty[1+(x)^2]^{-3\beta} \\
&\quad \times\frac{[T_{min}/T_0+f_{cool}^{-2}x^2]^\alpha}{[1+f_{cool}^{-2}x^2]^\alpha}\frac{1}{[1+f_t^{-2}x^2]^{\alpha/2}}\frac{r_c^2 x dx}{\sqrt{r_c^2x^2-\xi^2}} \\
&= \frac{\tilde{\Lambda}(Z)}{4\pi\,(1+z)^4}\frac{2n_{e0}^2\,T_0^\alpha}{\sqrt{f}}r_c\int_{\xi/r_c}^\infty[1+x^2]^{-3\beta} \\
&\quad \times\frac{[T_{min}/T_0+(x/f_{cool})^2]^\alpha}{[1+(x/f_{cool})^2]^\alpha}\frac{1}{[1+(x/f_t)^2]^{\alpha/2}}\frac{x dx}{\sqrt{x^2-(\xi/r_c)^2}}. \qquad (99)
\end{aligned}$$

In the fourth equation, we substituted $\zeta/r_c \to x$ and changed the integration variable suitably. Therefore, the integrand becomes a-dimensional, and all dimensional information is in front of if.

The temperature decrement is obtained in a similar way, but we have to set $m \to 1$ and $\alpha \to 1$. Hence,

$$\begin{aligned}
\frac{\Delta T_{SZ}}{T_{CMB}} &= f_{SZ}(\nu,T_e)\frac{\sigma_T k_B}{m_e c^2}\frac{2}{\sqrt{f}}T_{e0}\,n_{e0}\,r_c \\
&\quad \int_{\xi/r_c}^\infty[1+(x)^2]^{-3\beta/2}\frac{[T_{min}/T_0+(x/f_{cool})^2]^\alpha}{[1+(x/f_{cool})^2]^\alpha}\frac{1}{[1+(x/f_t)^2]^{\alpha/2}}\frac{x dx}{\sqrt{x^2-(\xi/r_c)^2}} \qquad (100)
\end{aligned}$$

3.4.2 2β model

Similar to the polytropic case, I introduce fractions to simplify the integral: the total central electron density $n_{e0} \equiv n_{e0,1} + n_{e0,2}$, an electron density fraction $f_e \equiv n_{e0,1}/n_{e0}$

and the fraction of the core radius $f_r = r_{c,1}/r_{c,2}$.

$$\begin{aligned} S_X &= \frac{\tilde{\Lambda}(Z)}{4\pi\,(1+z)^4}\frac{2}{\sqrt{f}}\int_{\xi}^{\infty} n^2_{e,2\beta}(\zeta)\,T^{\alpha}_{e,vik}(\zeta)\,\frac{\zeta d\zeta}{\sqrt{\zeta^2-\xi^2}} \\ &= \frac{\tilde{\Lambda}(Z)}{4\pi\,(1+z)^4}\frac{2}{\sqrt{f}} n^2_{e0}\,T_0^{\alpha} r_{c,2} \\ &\quad\times\int_{\xi/r_{c,2}}^{\infty}\left(\frac{f_e^2}{\left(1+(x/f_r)^2\right)^{3\beta_1}}+\frac{(1-f_e)^2}{(1+x^2)^{3\beta_2}}\right) \\ &\quad\times\frac{[T_{min}/T_0+(x/f_{cool})^2]^{\alpha}}{[1+(x/f_{cool})^2]^{\alpha}}\frac{1}{[1+(x/f_t)^2]^{\alpha/2}}\frac{xdx}{\sqrt{x^2-(\xi/r_{c,2})^2}}. \end{aligned} \quad (101)$$

Then, the temperature decrement is given as

$$\begin{aligned} \frac{\Delta T_{SZ}}{T_{CMB}} &= f_{SZ}(\nu,T_e)\frac{\sigma_T k_B}{m_e c^2}\frac{2}{\sqrt{f}} T_{e0}\,n_{e0}\,r_{c,2} \\ &\quad\times\int_{\xi/r_{c,2}}^{\infty}\left(\frac{f_e^2}{\left(1+(x/f_r)^2\right)^{3\beta_1}}+\frac{(1-f_e)^2}{(1+x^2)^{3\beta_2}}\right)^{\frac{1}{2}} \\ &\quad\times\frac{[T_{min}/T_0+(x/f_{cool})^2]}{[1+(x/f_{cool})^2]}\frac{1}{[1+(x/f_t)^2]^{1/2}}\frac{xdx}{\sqrt{x^2-(\xi/r_{c,2})^2}}. \end{aligned} \quad (102)$$

3.4.3 PA model

Not surprisingly, we can simplify the quantities in a similar way also in the case of the PA-model. Let us skip the step in between. They are very similar to the β-model:

$$\begin{aligned} S_X &= \frac{\tilde{\Lambda}(Z)}{4\pi\,(1+z)^4}\frac{2}{\sqrt{f}}\int_{\xi}^{\infty} n^2_{e,PA}(\zeta)\,T^{\alpha}_{e,vik}(\zeta)\,\frac{\zeta d\zeta}{\sqrt{\zeta^2-\xi^2}} \\ &= \frac{\tilde{\Lambda}(Z)}{4\pi\,(1+z)^4}\frac{2n^2_{e0}\,T_0^{\alpha}}{\sqrt{f}} r_c\int_{\xi/r_c}^{\infty} x^{1-\eta}[1+(x)^2]^{-3\beta+\frac{\eta}{2}} \\ &\quad\times\frac{[T_{min}/T_0+(x/f_{cool})^2]^{\alpha}}{[1+(x/f_{cool})^2]^{\alpha}}\frac{1}{[1+(x/f_t)^2]^{\alpha/2}}\frac{dx}{\sqrt{x^2-(\xi/r_c)^2}}, \end{aligned} \quad (103)$$

$$\begin{aligned} \frac{\Delta T_{SZ}}{T_{CMB}} &= f_{SZ}(\nu,T_e)\frac{\sigma_T k_B}{m_e c^2}\frac{2}{\sqrt{f}} T_{e0}\,n_{e0}\,r_c \\ &\quad\times\int_{\xi/r_{c,2}}^{\infty} x^{1-\eta/2}[1+(x)^2]^{-\frac{3\beta/}{2}+\frac{\eta}{4}} \\ &\quad\times\frac{[T_{min}/T_0+(x/f_{cool})^2]}{[1+(x/f_{cool})^2]}\frac{1}{[1+(x/f_t)^2]^{1/2}}\frac{dx}{\sqrt{x^2-(\xi/r_{c1})^2}}. \end{aligned}$$

3.4.4 VE model

We finish with the long expressions including the VE-model.

$$
\begin{aligned}
S_X &= \frac{\tilde{\Lambda}(Z)}{4\pi\,(1+z)^4}\frac{2}{\sqrt{f}}\int\limits_{\xi}^{\infty} n_{e,VE}^2(\zeta)\,T_{e,vik}^{\alpha}(\zeta)\,\frac{\zeta d\zeta}{\sqrt{\zeta^2-\xi^2}} \\
&= \frac{\tilde{\Lambda}(Z)}{4\pi\,(1+z)^4}\frac{2n_{e0}^2\,T_0^{\alpha}}{\sqrt{f}}r_c\int\limits_{\xi/r_c}^{\infty} x^{1-\eta}(1+(x)^2)^{-3\beta+\frac{\eta}{2}}\,(1+(x/f_s)^{\kappa})^{-\frac{\epsilon}{\kappa}} \\
&\quad\times\frac{[T_{min}/T_0+(x/f_{cool})^2]^{\alpha}}{[1+(x/f_{cool})^2]^{\alpha}}\frac{1}{[1+(x/f_t)^2]^{\alpha/2}}\frac{dx}{\sqrt{x^2-(\xi/r_c)^2}}, \qquad (104)
\end{aligned}
$$

$$
\begin{aligned}
\frac{\Delta T_{SZ}}{T_{CMB}} &= f_{SZ}(\nu,T_e)\frac{\sigma_T k_B}{m_e c^2}\frac{2}{\sqrt{f}}T_{e0}\,n_{e0}\,r_c \\
&\quad\times\int\limits_{\xi/r_c}^{\infty} x^{1-\frac{\eta}{2}}(1+(x)^2)^{-\frac{3\beta}{2}+\frac{\eta}{4}}\,(1+(x/f_s)^{\kappa})^{-\frac{\epsilon}{2\kappa}} \\
&\quad\times\frac{[T_{min}/T_0+(x/f_{cool})^2]}{[1+(x/f_{cool})^2]}\frac{1}{[(1+(x/f_t)^2)]^{1/2}}\frac{dx}{\sqrt{x^2-(\xi/r_c)^2}}, \qquad (105)
\end{aligned}
$$

where $f_s = r_s/r_c$.

3.5 On the deprojection of X-ray surface brightness

We already introduced a multi wave length approach to estimate the elongation of a cluster through combination of X-ray observations and temperature decrement measurements. But, without taking account for gravitational lensing or assuming given cosmological parameters, the degeneracy among elongation and distance can not be broken. Disregarding the temperature decrement of the SZE might lead to additional uncertainties. Or is it possible to estimate the true cluster shape just with observations in the X-ray band?

Chakrabarty et al. [Chakrabarty 08] proposed in 2008 a new method to determine the intrinsic shape of galaxy clusters due to X-ray measurements without using SZE data. They project the cluster X-ray surface brightness profile under peculiar assumptions about geometry and inclination that correspond to four extreme scenarios. An intercomparison of the different deprojected emissivity profiles should lead to the signature of the true cluster shape. SZE data might improve the inclination, but the shape determination should be possible by implementing the X-ray brightness alone.

3.5.1 Analytic counterexample: prolate vs. oblate cluster

With a simple counterexample we will show that a unique determination of axial ratios and orientation of an ellipsoid representing the electron density of a galaxy cluster is not possible using only X-ray brightness profiles and the method described by Chakrabarty does not work in general. We start with a simple β-model (see section 2.1). This is a model that describes the electron density of the cluster parameterized by two parameters θ_c and β and its central electron density. In addition, we are assuming an isothermal plasma with constant metallicity.

We assume a *prolate* cluster with inclination $\theta = 0$, i.e. its major axis along the line

of sight. According to section 3.1, its intrinsic axial ratio is q_{int} and its projected axial ratio is $e_{p,pro} = 1$. The other observable parameters, projected angular core radius θ_p, and therefore θ_c. The central surface density S_{X0} and the slope β are arbitrarily chosen. The orientation of the projection does not give additional information, since j and k in (51) are equal and therefore, ψ_{Eu} is not defined.

The projection of an *oblate* cluster with its minor axis along the line of sight has the property: $e_{p,obl} = 1$. If it is at the same position in the plane of the sky and has the same observable features as the prolate one introduced above, we can't distinguish between these two ellipsoids[12].

Under the conditions above, the elongations, equations (61) and (62), reduce to:

$$e_{\Delta,pro} = q_{int,pro}, \tag{106}$$

$$e_{\Delta,obl} = \frac{1}{q_{int,obl}}. \tag{107}$$

But e_Δ can not be measured and therefore can't help to limit the model. The subscripts $_{pro}$ or $_{obl}$ denote the quantity of the prolate or oblate clusters.

Equation (52) describes the dependence of the projected core radius on the intrinsic parameters. If we equalise this radius θ_c in the case of a prolate and an oblate cluster in consideration of $f = 1$ and $e_p = 1$ we get

$$\theta_{c,pro}\, q_{int,pro} = \theta_{c,obl} \,/\, q_{int,obl}. \tag{108}$$

In the case of a simple β-model, the central surface brightness is given as $S_{X0} \propto n_{e0}^2 \theta_c / \sqrt{f}$, up to a prefactor that is independent on geometric cluster parameters, see equation (71). If we equalise the prolate and oblate expression for S_{X0}, we get

$$\theta_{c,pro}\, n_{e0,pro}^2 = \theta_{c,obl}\, n_{e0,obl}^2. \tag{109}$$

These equations depend on intrinsic, not directly measurable parameters and are therefore degenerate in a sense that we are free to choose values for these parameters as long as they satisfy equations (108) and (109). And as long as these equations are satisfied, we observe the same S_{X0} and θ_p for both clusters.

The central surface brightness S_{X0} is the only model dependent observable. In the case of a general model, S_{X0} is a product of an intrinsic length scale (e.g. the core radius), the square of the normalisation of the central electron density, a geometrical factor f and a factor that depends only on model dependent parameters, see equation (130). The latter two cancel in (109) since $f_{obl} = f_{pro} = 1$ and the model dependent values $(p_1, p_2, ...)$ are equal. Therefore this counterexample is model independent.

In this simple example, we are not able to determine the shape of this cluster starting from the 'observed' quantities, e.g. we can not distinguish between oblate and prolate. Therefore, the method described in Chakrabarty et al. (2007) is not general.

3.5.2 Degeneracies of the triaxial β model

In the case of an arbitrary triaxial β-model, there are four observable parameters, which we collected in equations (110) to (113), dropping the slope β. In the second equation of each line, we express the dependence on axis ratios and orientation as functions f_i to highlight the dependence of this observable quantities on non-geometrical parameters,

[12] The same angular diameter distance D_A was assumed for both possible solutions to focus on the intrinsic degeneracies. In general, this is a parameter inversely proportional to the Hubble constant. Without additional (external) measurements (SZE, gravitational lensing), it could lead to a degeneracy with the cluster geometry (i.e. e_Δ). But let's keep the eye on the intrinsic degeneracies.

that means parameters which are not connected to shape or orientation of the cluster. We assume that $\Psi = 0$, so that $\psi = \psi_{Eu}$. Ψ would just require a more complex function of j_ζ, k_ζ and l_ζ, which are a function of ψ_{Eu}.

$$\psi = \frac{1}{2}\arctan\left(\frac{2k}{j-l}\right) = f_\psi(e_1, e_2, \theta, \varphi) \tag{110}$$

$$e_p = \sqrt{\frac{j+l+\sqrt{(j-l)^2+4k^2}}{j+l-\sqrt{(j-l)^2+4k^2}}} = f_e(e_1, e_2, \theta, \varphi) \tag{111}$$

$$\theta_p = \theta_c \left(\frac{e_p}{e_1\, e_2}\right)^{1/2} f^{1/4} = \theta_c\, f_\theta(e_1, e_2, \theta, \varphi) \tag{112}$$

$$S_{X0} = \frac{\Lambda_e}{4\sqrt{\pi}(1+z)^4} n_{e0}^2 \frac{D_d \theta_p}{e_\Delta} \frac{\Gamma(3\beta - 1/2)}{\Gamma(3\beta)} = n_{e0}^2 \frac{\theta_c}{\sqrt{f}}\, f_\beta(\beta) \tag{113}$$

The intrinsic core radius θ_c is the intrinsic scale parameter of the model. Due to the normalization by the central electron density n_{e0}, every observed value of S_{X0} can be achieved by a suitable choice of θ_c, which can be expressed as a function of of the geometrical factors, i.e. there is a degeneracy between n_{e0}, θ_c and cluster shape as showed in the example above.

An analytic expression of this degeneracies can be achieved as follows: Assuming $f_\beta = 1$, equation (113) is:

$$S_{X0} = n_{e0}^2 \frac{\theta_c}{\sqrt{f}}. \tag{114}$$

θ_p depends on several intrinsic quantities (112), whereas only the projected axial ratio e_p can be directly measured. If we assume the ratio of this quantities as a unique observable quantity:

$$\hat{\theta}_p \equiv \frac{\theta_p}{\sqrt{e_p}} = \theta_c \left(\frac{1}{e_1\, e_2}\right)^{1/2} f^{1/4}, \tag{115}$$

we can multiply S_{X0} and $\hat{\theta}_p^2$ and thus define a new parameter Υ build by the intrinsic quantities,

$$\Upsilon \equiv S_{X0} \frac{\theta_p^2}{e_p} = n_{e0}^2 \frac{\theta_c^3}{e_1\, e_2}. \tag{116}$$

The left hand side of this equation depends only on observed quantities and the right hand side is just a function of intrinsic axial ratios, n_{e0} and θ_c, independent of the orientation angles.

This means, starting from a set of observed parameters (ψ, e_p, θ_p, S_{X0}), multiple cluster scenarios are possible as long as this combination of parameters equals for each cluster. More precisely: if we are comparing clusters A and B, their parameters have to fulfil:

$$n_{e0,A}^2 \frac{\theta_{c,A}^3}{e_{1,A}\, e_{2,A}} = n_{e0,B}^2 \frac{\theta_{c,B}^3}{e_{1,B}\, e_{2,B}}. \tag{117}$$

The suitable orientation angles are then determined by the equations of ψ and e_p. Some numerical examples will explain this situation, e.g. section 3.5.3, example 2.

Let's assume that two cluster candidates A and B have the same central electron density and the same core radius, that means

$$e_{1,A}\, e_{2,A} = e_{1,B}\, e_{2,B}. \tag{118}$$

That means that in this very peculiar case, we can't even uniquely determine the set of intrinsic axis ratios (e_1, e_2, e_3) since they are degenerate.

shape	e_1	e_2	φ	θ	θ_c	n_{e0}
prolate	1.8	1.8	-	0	3.6	1.666
oblate	0.8	0.8	-	0	1.6	2.5

Table 3: Numerical example 1. The 'observed' values are (e_p, θ_p, S_{X0})=(1, 2, 10), and $e_3 = 1$. The angles are measured in radians.

3.5.3 Numerical examples

In the following examples, we will use the β-model to describe the electron density profile. Equations (110 - 113) characterising the observable parameters can be decoupled into a pair of equations that depend only on axis ratios and orientation, the (ψ, e_p)-system, and a pair that depends on the core radius, central electron density and slope β: the (θ_p, S_{X0})-system. Therefore, assuming that the observational quantities and two initial parameters are known, the remaining geometrical parameters are given by the first two equations. In a second step, the (θ_p, S_{X0})-system defines θ_c and n_{e0}. Our goal is to find multiple cluster configuration that fit a single set of observed quantities. Finally, the equality of the solutions is easily tested by inserting them into equations (110) to (113). We use arbitrary units and set $f_\beta = 1$.

Example 1: prolate vs. oblate This example is identical to the scenario in section 3.5.1. An arbitrarily chosen axis ratio of an axisymmetric ellipsoid aligned with the line of sight ($\theta = 0$) should fit the observed values if θ_c and n_{e0} are appropriate.

For such particular initial conditions, $e_1 = e_2$ obeys the spheroidal shape, therefore k=0 ((48) and j=l (47) and (49)). On the other hand, the third Euler angle $\psi = (1/2)tan(2k/(j-l))$ is not well defined in this case, so we will ignore equation (110). Moreover, $e_p = 1$ becomes a fix 'observable' quantity.

The (ψ, e_p)-system reduces to

$$e_1 = e_2, \tag{119}$$

$$e_p = 1. \tag{120}$$

Therefore, in the spheroidal case, we can freely choose $e_1 = e_2 = q_{int,pro} > 1$ for a prolate or $0 < e_1 = e_2 = 1/q_{int,obl} < 1$ for an oblate cluster model, see table 3. There is no φ-dependence in e_p or f anymore, hence we ignore φ. Finally, we have to choose values of S_{X0} and n_{e0} to complete the set of 'observed' quantities. Solving equation (112) for θ_c gives in consideration of $f = 1$

$$\theta_c = \theta_p \sqrt{e_1\, e_2}, \tag{121}$$

and than solving equation (113) for n_{e0}

$$n_{e0} = \sqrt{\frac{S_{X0}}{\theta_c}}. \tag{122}$$

For these two spheroidal scenarios, we can find two sets of solutions, see table 3. This shows that one can't distinguish between an oblate and prolate model in this special scenario.

In addition, q_{int}, n_{e0} and θ_c of the prolate and oblate model fulfill equations (108) and (109), of course.

Example 2: simple orientation In a more general case, assuming triaxial models, we calculate two solutions of the first pair of equations and insert them into the second pair to get a proper core radius and a suitable central electron density (table 5).

$sin\varphi = 0$	$\theta =$	-2.449	2.449	-0.692	0.692

Table 4: Example of the structure of the (θ, φ)-solution, if the initial values (e_1, e_2)=(0.3, 0.5). The simple degeneracies are obvious.

shape	e_1	e_2	φ	θ	θ_c	n_{e0}	Υ
triaxial	0.4	0.7	0	0.745	0.8	2.339	10
triaxial	0.3	0.5	0	2.449	0.6	2.635	10
oblate	0.4	0.4	0	1.237	0.8	1.767	10

Table 5: Numerical example. The 'observed' values are (ψ, e_p, θ_p, S_{X0})=(0, 2, 2, 5), $f_\beta = 1$ and $e_3 = 1$. The angles are measured in radians. The equality of Υ, equation (116), documents the degeneracies among the parameters.

Solving the (ψ, e_p)-system becomes more complex. In order to eliminate the inverse tangent, we convert this system into

$$\hat{\psi} \equiv \tan(2\psi) = \frac{2k}{j-l}, \tag{123}$$

$$e_p = \sqrt{\frac{j+l+\sqrt{(j-l)^2+4k^2}}{j+l-\sqrt{(j-l)^2+4k^2}}}. \tag{124}$$

A simple set of 'observed' quantities is (ψ, e_p, θ_p, S_{X0})=(0, 2, 2, 5). In this case, $\psi = \hat{\psi} = 0$. Solving with suitable[13] initial values e_1 and e_2, several solutions (θ, φ) exist. In the case of (e_1, e_2)=(0.3, 0.5), among several complex solutions, two couples of real results are given in the following table 4. Out of this solutions, we choose groups of real parameters which solve the (ψ, e_p)-system, e.g. table 5. In the triaxial case, the (θ_p, S_{X0})-system leads to the intrinsic core radius and the central electron density:

$$\theta_c = \theta_p \left(\frac{e_1\, e_2}{e_p}\right)^{1/2} \frac{1}{f^{1/4}}, \tag{125}$$

$$n_{e0} = \sqrt{\frac{S_{X0}}{\theta_c}}\, f^{1/4}. \tag{126}$$

Inserting the computed core radius in (126) provides complete sets of parameters to describe triaxial clusters with β-model electron density shape (the slope is given by f_β=1), table 5. We add an axisymmetric, oblate cluster which is also able to reproduce the 'observed' values.

Example 3: triaxial In order to get the most general example, we start with initial orientations (φ, θ) but compared with example 2, we choose $\psi \neq 0$, respectively $\hat{\psi} \neq 0$, e.g. (ψ, e_p, θ_p, S_{X0})=(0.155, 2.6, 2, 5), hence $\hat{\psi} = 0.32$. Therefore, we get a cluster that is rotated by all Euler's angles and therefore, it describes that most general case concerning the orientation.

The $(\hat{\psi}, e_p)$-system, equations (123) and (124), can be numerically solved. Keeping in mind the degeneracies among the orientations, unique solutions (e_1, e_2) are found. As before, inserting these solutions in (125) and (126) gives suitable values of θ_c and n_{e0}, see table 6.

In order to compare these general shaped cluster with a spheroid, we substitute the equation of $\hat{\psi}$ with the condition that $e_1 = e_2$ and proceed similar to the first

[13] In this example, the existence of a real solution depends on the choice of the initial values of e_1 and e_2, respectively on e_p. To reproduce the quantities on the plane of the sky, one of the intrinsic axis ratios e_i should be at least as small as the projected one. Moreover, extreme values may not represent a physical cluster.

shape	e_1	e_2	φ	θ	θ_c	n_{e0}	Υ
triaxial	1.669	4.506	1.1	0.8	2.440	1.994	7.692
triaxial	2.684	6.026	1.3	0.3	4.353	1.228	7.692
prolate	8.182	8.182	1.3	0.3	6.294	1.437	7.692
unphysical	5.933	38.160	0.7	0.3	6.308	2.633	7.692

Table 6: Numerical example. The 'observed' values are (ψ, e_p, θ_p, S_{X0})=(0.155, 2.6, 2, 5), and $e_3 = 1$. The angles are measured in radians. The equality of Υ, equation (116), documents the degeneracies among the parameters.

example. Despite of its additional symmetry, the prolate cluster is able to reproduce the 'observed' quantities as good as the triaxial one even though the orientations are identical. This reflects the degeneracy among these parameters, documented by Υ.

In this example, not every orientation leads to physical solutions. Line 4 in table 6 describes are highly elongated cluster since $e_3 = 1$ and is not a solution to take into account. If $\theta = 0.3$ is fixed and $\varphi \to 0$, no solution exists. Therefore, we might limit the range of orientation.

3.5.4 Model independent statements

Every parametric model uses a scale factor whose projection is defined as (52).

In general, it holds, [Stark]:

$$F_S(\xi) = \frac{2}{\sqrt{f}} \int_\zeta^\infty \frac{F_V(\zeta)\zeta}{\sqrt{\zeta^2 + \xi^2}}\, d\zeta \tag{127}$$

if the intrinsic volume density F_V is monotonically decreasing with radius. F_S is its projection on the plane of the sky as a function of the elliptical radius. All geometrical aspects are packed into the prefactor $1/\sqrt{f}$. The integral in ζ is proportional to an intrinsic scale length l_c. The size of the ellipsoid along the line of sight can be expressed in terms of the intrinsic scale length. Its projected counterpart is:

$$l_p = l_c \frac{e_\Delta}{\sqrt{f}} = l_c\, f_\theta(e_1, e_2, \theta, \varphi). \tag{128}$$

Therefore, the X-ray surface brightness S_X can be written as

$$S_X = S_{X0} \cdot f_{S_x}(\xi, l_c, p_1, p_2, ...), \tag{129}$$

where $\xi = D_d \sqrt{\theta_1^2 + e_p^2\, \theta_2^2}\, (l_c/l_p)$ denotes the radial dependence and the central surface brightness S_{X0} is

$$S_{X0} = n_{e0}^2 \frac{l_c}{\sqrt{f}} \cdot f_{S_{X0}}(l_c, p_1, p_2, ...). \tag{130}$$

l_p, p_1, p_2 etc. are model dependent parameters which are obtained by fitting the X-ray brightness[14]. S_{X0} has the same structure as in the β-model case (113) and we can adapt equation (116) to describe degeneracies model *independent*.

Therefore, X-ray brightness measurements are not enough to constrain the shape and orientation of a ellipsoidal galaxy cluster because the set of observable quantities is to small to eliminate all degeneracies.

[14]The prefactors depending on e.g. the redshift and metallicity of the cluster are also packed into $f_{S_{X0}}$. See section 3 to know how the prefactors vary under different model assumptions.

4 On the estimation of the elongation

In the previous sections, we introduced different models for electron densities and temperature profiles and we derived analytic expressions for the X-ray surface brightness and the temperature decrement for some combinations of those models. Now, we will use those results.

In this section, we will examine the estimation of the cluster elongation. Our goal is to derive a method to estimate the cluster elongation and to understand the dependence of the accuracy of the estimated elongation on the quality of the observed quantities. If we know these dependences, we can decide which model we should use to examine the cluster elongation in consideration of the accuracy of the different measurements. Hence, we can avoid to use a complex model to fit the data whenever a simpler model can give a comparable estimation of the elongation. The X-ray surface brightness profile provides orientation and ellipticity of the projected cluster and also the parameters that describe the electron density. Spectroscopic measurements give the temperature profile of the ICM and the SZ-effect provides the central temperature decrement. We do not use the SZ data to constrain the model parameters since the astrometric precision is usually much worse than in the X-ray measurements. If we know all those values we can estimate the elongation.

We will not use real observational data. Instead, we will perform simulations of the projected quantities, where we mimic an accuracy similar to observatories like Chandra, and analyse the dependence of the fitted parameters and of the elongation on the initial data. So, we can make statements about the needed accuracy of the data or about the level of precision that electron density or temperature parameters should have to guarantee a desired accuracy of the estimated elongation.

First, we describe the steps we have to do. We start with the simulation of the projected quantities, that means $S_X(r), \Delta T_0$ and $T_e(r)$. Then, with certain fitting procedures we constrain the model and temperature parameters. We combine these values to end up with the elongation and its uncertainty. To illustrate the simulations and present some details, we give an example of the whole procedure where we will focus on the polytropic β-model. We report on peculiarities of the other models in the following paragraphs. Then, we vary the assumptions about the precision of the measurements and the used models to examine several cases. At last, we make some final considerations.

Chandra observation of Abell 1995 A measurement made by Chandra in 2000 of the galaxy cluster Abell 1995 gives data that represents a typical cluster observation. Dr. de Filippis recently analysed the measurement and provided us with the X-ray observation files, with a reduced binned map and a extracted X-ray surface brightness profile, figure 17. In addition, we received measurements of the temperature profile, see table 7. We will use these observations as reference so that our simulated values and their errors are in the correct order of magnitude.

$r_i\,[arcsec]$	17.5	26.25	35.0	43.75	53.63	65.44	81.18	108.73
$T(r_i)\,[keV]$	6.45	8.25	7.32	8.51	8.47	7.79	6.80	13.4
$\sigma_{T(r_i)}\,[keV]$	2.00	1.99	1.31	2.11	2.36	1.74	1.69	10.6

Table 7: The measured temperature profile of A1995. r_i denote the semi major-axes of the annuli. The average error on this estimations is $\sigma_{T(r)} \sim 2\,keV$, if we skip the outermost annulus.

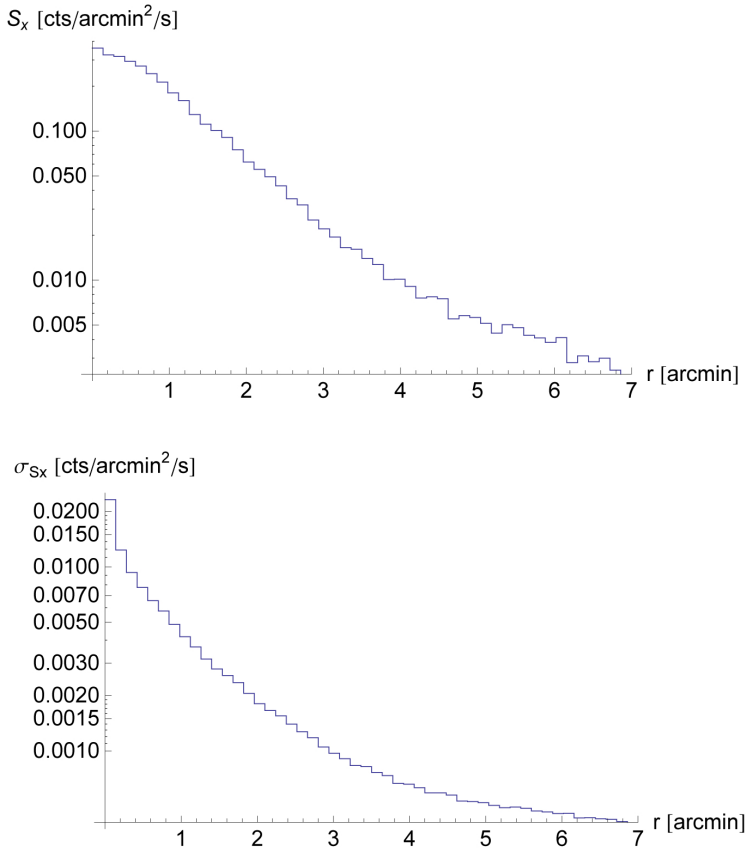

Figure 17: TOP: A surface brightness profile of Abell 1995, binned in annuli. The width of an annulus is $0.15'$. The averaged total photon count in a superpixel embodied in the central annulus is $N_c \sim 23\,cts$. BOTTOM: The error on the annuli.

4.1 X-ray surface brightness

4.1.1 Simulation

A simulation of a X-ray surface brightness map is performed in several steps.

- First, we pick a useful set of intrinsic parameters that define the shape and orientation of the 'observed' cluster. We choose a model which describes the electron density and define an appropriate set of parameters. Then, we decide to assume an isothermal gas or to include a radial depending temperature profile as e.g. in the case of a polytropic gas and choose the required parameters. Moreover, we have to make assumption about the energy band of the simulated observation, the cooling function, the cluster distance and other initial parameters.

- Next, we have to decide which method of projection we want to use to get the map, i.e. how we compute the observational quantities introduced in section 3.2. This is just a question of computation time but does not affect the result. There are several ways to proceed: The easiest one it the direct numerical integration along the line of sight, but it takes more time than other methods. If we convert the integral into a function of the elliptical radius as shown in (63), we can choose to express this radius in terms of the ellipticity or in terms of the coefficients j_ζ, l_ζ and k_ζ, (56) or (58). Following section 3, it makes sense to use the analytic expressions of the integrals that we have derived as much as possible to reduce computation time.

- We have to decide which size and resolution our simulated map should have. The resolution gives the distance between two simulated points; this can be equal to the pixel size of a real detector, for example. If we decrease size and/or increase resolution, we also increase the number of simulated data points which is of crucial importance for the computing time in the following steps.

- Then, in order to simulate maps like they are observed through the Chandra telescope we have to add noise to the data that is reflecting the statistical uncertainties of the measurement.

Finally, we end up with a map that provides realistic features. Of course, we do not simulate substructures. Figure 18 gives an example of a simulated map, with noise and without.

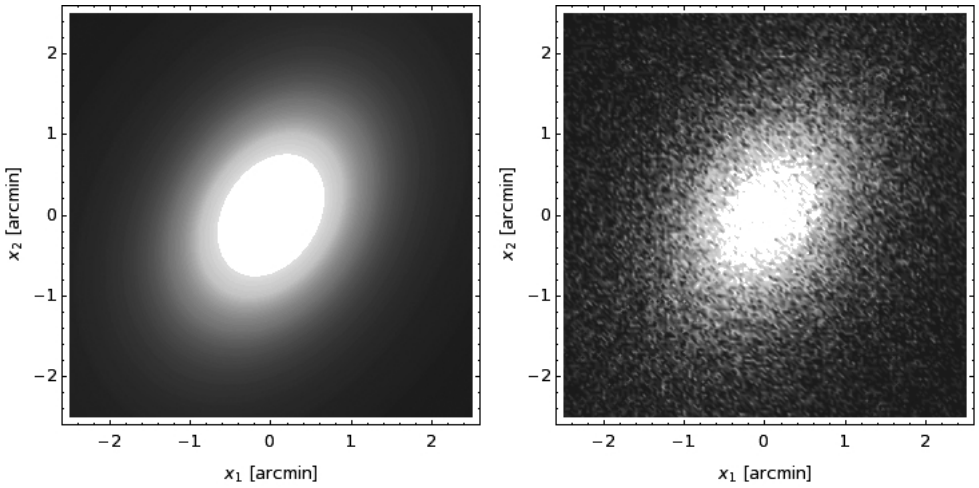

Figure 18: LEFT: A simulated X-ray surface brightness map with a field of view of $2.5' \times 2.5'$ and a pixel size of $2" \times 2''$. RIGHT: The same cluster but with noise. The cluster parameters are the same that we use in section 4.5: $(e_1 = 1.5, e_2 = 1.3, e_3 = 1, \theta_{Eu} = 60°, \varphi_{Eu} = 20°, \psi_{Eu} = 30°, \theta_c = 1', \beta = 0.6, \gamma = 1.3, \alpha = 0.25)$.

Initial parameters This simulation should represent a typical cluster, as it can be observed by Chandra or other observatories. We can distinguish between four groups of parameters:

- geometrical parameters, that control the intrinsic shape and orientation of the cluster:
  $e_1, e_2, \theta_{Eu}, \varphi_{Eu}, \psi_{Eu}$.

- model parameters that describe the chosen electron density model:
  $n_{e0}, r_{c1}, \beta_1, ...$

- temperature parameters that contain information about the temperature profile:
  $T_0, \gamma, T_{min}, r_{cool}, ...$

- additional parameters, like the energy band of observation, the physical constants, the distance parameters:
  $\alpha, \Lambda, z, ...$

We consider Chandra measurements of true clusters which provide a true X-ray surface brightness to obtain an estimate of the number of photons an observatory can actually detect, so that we have to be sure that our set of parameter is consistent with this

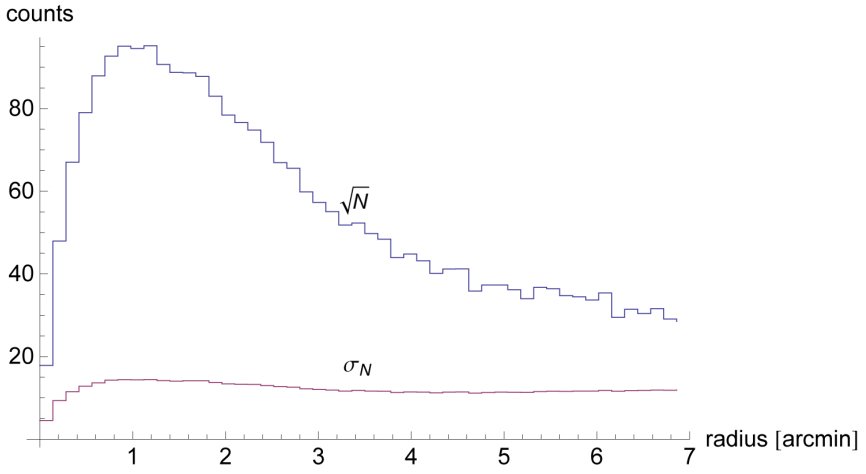

Figure 19: The error on the total number of measured photons N per annulus σ_N provided by the data file compared with $\sqrt{N}$. Both are in the same order of magnitude.

counts. Thus, instead of choosing n_{e0} as an initial parameter, we decide to calculate n_{e0} with respect to those measurements. More precisely, we compute n_{e0} so that the central X-ray surface brightness equals the value in A1995.

Noise There are different methods to reproduce noise. Usually, we can assume that the observed values of the photon counts are distributed Poisson-like around the total expected number of photons that are measured at one pixel of the CCD sensor during the exposure time. If the exposure time or the X-ray flux are high enough, that means, if the total number of counts everywhere is larger then ~ 10, the Poisson distribution can be replaced by a Gaussian distribution. This number is connected to the total exposure time, to the sensitivity of the detector, to the binning and to the received flux, of course. But usually, there are not enough photons per pixel observed.

The A1995 data consists of a pure observation map and a binned map, where the detector pixels ($0''5 \times 0''5$) are binned into areas with $2'' \times 2''$ to obtain a higher photon count, let us call them *superpixel*. Moreover, the A1995 data includes a list that represents the measured photons per *second* per $arcmin^2$ arranged in annuli with a width of $0.14'$, figure 17. It also provides the error on the measurements of each annuli. Taking into account the exposure time and the resolution, we can calculate the total number of photons N measured in an annuli. Figure 19 compares the given error on N, σ_N, this is the error on the A1995 measurements, with $\sqrt{N}$ - this is the standard deviation of a Poissonian distribution with mean N. The comparison of the two errors in figure 19 shows that they are of the same order of magnitude, as expected.

Conversion We take the Chandra observation of Abell 1995 as a reference and we assume that the central surface brightness in our simulation equals the measured photon count in the central bin. Therefore, we have to estimate a conversion factor C which allows to convert a flux, $S_X[erg/cm^2/sec]$ to a count rate, $S_X[counts/sec]$ and vice versa. C can be obtained through the `webPIMMS`-application[15], which evaluates this instrument dependent conversion factor. We assume that the simulated count of our central pixel is the 'observed' count rate, and webPIMMS gives the central surface brightness in the desired *cgs*-units. Since the cluster emissivity depends on the temperature, we have to include the cluster temperature in the webPIMMS-application obtained by analysing a 'measured' temperature profile, see below.

[15] http://heasarc.gsfc.nasa.gov/Tools/w3pimms.html

We also use this conversion to complete our set of initial parameters. The central surface brightness is a function of the central electron density n_{e0}. Assuming typical values for all the other initial parameters, we can calculate the central electron density of the cluster that is consistent with the Abell 1995 measurements.

4.1.2 Fitting Procedure

Starting from the simulated X-ray surface brightness map obtained as described above, we want to fit a suitable electron density model and temperature profile. Thus, we obtain quantities like the central surface brightness S_{X0}, the ellipticity e_p and orientation Ψ of the cluster ellipse and parameters that describe the electron profile like the projected core radius or a slope parameter. We tried several methods to get a good fit.

Due to the fact that we only obtained analytic expressions for the X-ray surface brightness if we assumed a polytropic gas instead of a more complex temperature gradient, we limit the fitting procedure to the polytropic gas models. The Vikhlinin temperature profile would be in conflict with our attempt to realise a low computing time procedure whereas we fit an expression that consists of 'elementary' functions.

Shape and orientation There are at least five free parameters (S_{X0}, e_p, Ψ, r_p, β and additional model dependent parameters). If we want to estimate all parameters at once, the fitting procedure fails. Hence, we split the set of parameters into two groups: parameters that describe the shape and orientation of the ellipse (e_p, Ψ) and parameters that control the electron density model (S_{X0}, r_p, β, ...). First, we try to estimate e_p and Ψ.

With an arbitrary set of model parameters, we try to obtain e_p and Ψ through a fit of the simulated surface brightness map. This is motivated by the fact that those parameters are independent of the model parameters and a change in r_c would not affect the ellipticity, for example. But without suitable model parameters, we are not able to estimate shape and orientation correctly. We execute the fitting procedure several times, always changing the initial parameters r_p and β a little bit. At the end, the ellipticity and the orientation are widely scattered, their variance is very large. This is not a good method to obtain e_p and Ψ.

Bartelmann and Schneider [Bartelmann] use the tensor of second brightness moments Q_{ij} to analyse the projected shape of galaxies. This tensor is defined by

$$Q_{ij} = \frac{\int d^2\theta \, q_S[S_X(\vec{\theta})](\theta_i - \theta_{0,i})(\theta_j - \theta_{0,j})}{\int d^2\theta \, q_S[S_X(\vec{\theta})]}, \quad i,j \in \{1,2\}. \tag{131}$$

$S_X(\vec{\theta})$ is the X-ray surface brightness at the angular position $\vec{\theta}$. $q_S[S_X(\vec{\theta})]$ is a suitably chosen weight function. In our case, $q_S[S_X(\vec{\theta})] = S_X H(S_X - S_{X,min})$, whereas H is the Heaviside step function. This weighting guarantees that the center of light $\vec{\theta}_0$ within the limiting isophote $S_{X,min}$ is given by

$$\vec{\theta}_0 = \frac{\int d^2\theta \, q_S[S_X(\vec{\theta})]\vec{\theta}}{\int d^2\theta \, q_S[S_X(\vec{\theta})]}, \quad i,j \in \{1,2\}. \tag{132}$$

Then, we quantify the shape of the projection by the complex ellipticity

$$\chi = \frac{Q_{11} - Q_{22} + 2iQ_{12}}{Q_{11} + Q_{22}}. \tag{133}$$

This can be parametrised by the axis ratio q and the position angle Ψ of the elliptical isophotes:

$$\chi = \frac{1-q^2}{1+q^2} e^{2i\Psi}. \tag{134}$$

Therefore, the ellipticity $e_p = 1/q$ is obtained by solving this equation

$$|\chi| = \frac{1-q^2}{1+q^2} \tag{135}$$

and the orientation by using the fact that the imaginary part of a complex number z equals the absolute value of z times the sinus of the phase of z,

$$\sin(2\Psi) = \frac{\mathrm{Im}\chi}{|\chi|}. \tag{136}$$

The correct signature of Ψ is given by the signature of the imaginary part of χ.

Since our simulation consists of discrete data points, we have to replace the integral in Q_{ij} by a sum. Moreover, we can assume that the center of light $\vec{\theta_0} = (0,0)$. Then, the tensor reads

$$Q_{ij} = \frac{\Sigma_{k=1}^{m}\Sigma_{l=1}^{m} S_X(\theta_{1,k},\theta_{2,l}) H(S_X(\theta_{1,k},\theta_{2,l}) - S_{X,min})\theta_{i,k}\theta_{j,l}}{\Sigma_{k=1}\Sigma_{l=1} S_X(\theta_{1,k},\theta_{2,l}) H(S_X(\theta_{1,k},\theta_{2,l}) - S_{X,min})}, i,j \in \{1,2\}. \tag{137}$$

m gives the number of bins along the simulated field of view. $\theta_{j,l}$ denotes the j^{th} component of the position of the l^{th} bin measured in the direction of the j^{th} axis. From (135) and (136), we are able to estimate the orientation and shape of the cluster on the plane of the sky. The only free parameter is $S_{X,min}$. It makes sense to check if the $S_{X,min}$ is of the right order of magnitude before e_p and Ψ are estimated. We vary the surface brightness $S_{X,min}$ in a wide range and observe the behaviour of those estimations. In this way, we exclude the very noisy outer regions. Usually, as soon as $S_{X,min}$ is higher than a particular value, e_p and Ψ are more or less constant till $S_{X,min} \to S_{X,max}$, the maximum of the S_X map, where we start to exclude too many points, figure 20.

Model dependent parameters Through the separated estimation of ellipticity and orientation, we can change from fitting a two dimensional map to fitting a radial profile. The estimation of e_p and Ψ allows us to bin the X-ray surface simulation. That means that we will gather data points that are in a given range of radius, those regions are called annulus. Figure 21 shows a set of annuli drawn on a X-ray surface brightness map. I will shortly explain the algorithm which enables to bin the data.

Let us define an annulus A_j as the set of points that are enclosed by two elliptical radii r_j and r_{j+1}. This radii are defined as

$$r_j \equiv \frac{a_j\, e_p}{\sqrt{1-(1-e_p^2)^2\cos[\alpha-\Psi]^2}} \tag{138}$$

where e_p and Ψ are ellipticity and orientation of the cluster on the plane of the sky and α is the free polar angle. a_j is the length of the inner semi-major axis of the j^{th} elliptical annulus. In our case, it is limited to the half size of the simulation map n_{size} and connected to the number of annuli n_{annu}, we want to obtain:

$$a_j = \frac{n_{size}}{n_{annu}} j \tag{139}$$

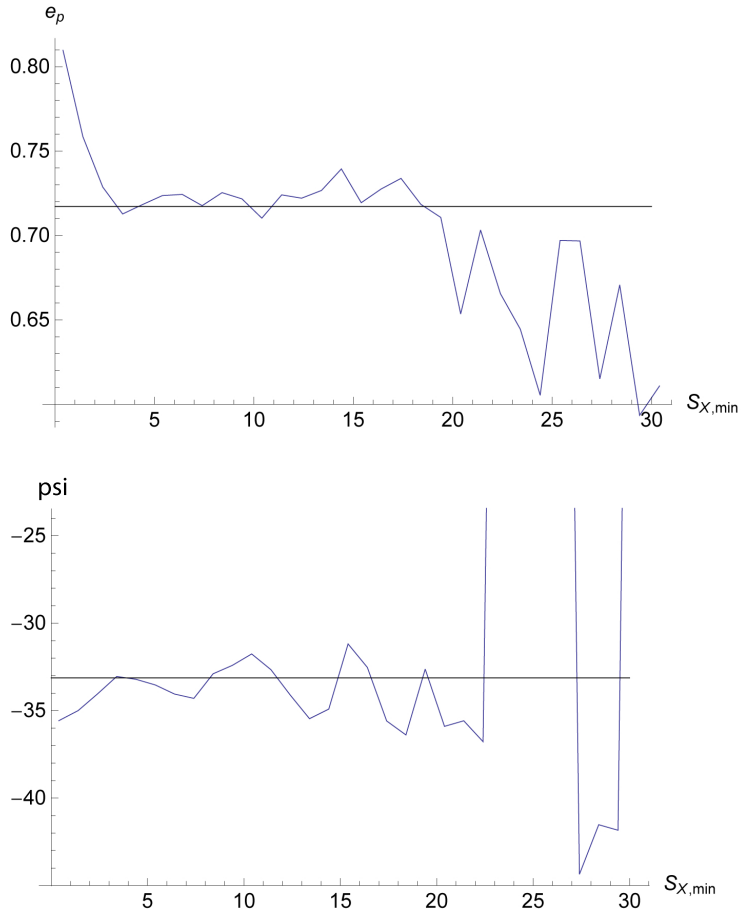

Figure 20: The choice of the limiting surface brightness $S_{X,min}$ affects the estimation of ellipticity and elongation. As long as $S_{X,min}$ is in a certain interval, in the examples above between $S_{X,min} = [5, 15]$, the estimation is close to the true value.

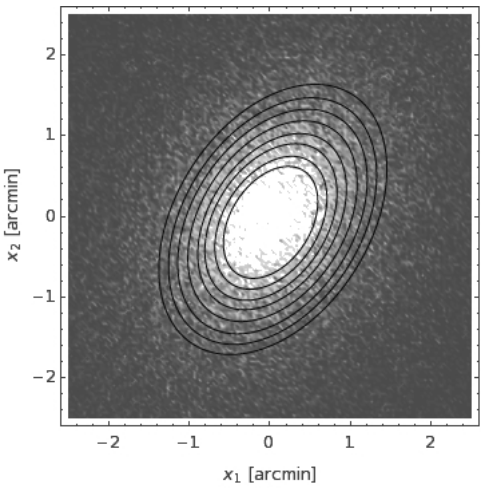

Figure 21: Some annuli drawn on a simulated X-ray surface brightness map.

Therefore, the simulated point, $S_X(x_i, y_i)$ is part of A_j, if

$$r_j \leq \sqrt{x_i^2 + y_i^2} < r_{j+1} \tag{140}$$

where $\alpha = \arctan(y_i/x_i)$ in r_j. If $j = 0$, then $r_0 = 0$. With these tools, we can map the surface brightness onto a profile along the major axis of the projected ellipse. We do this to split the fitting procedure into two parts whose parameters are almost independent. The binning by the annuli allows us to assume that the error on the total photon count N_j per annulus A_j is normal distributed, since the total number of photons per annuli is usually high enough, even in the outer regions - at least if we do not draw too small annuli. The error on the averaged photon count $\bar{N}_{pix}$ per superpixel located in an annulus A_j is given by $\sqrt{\bar{N}_{pix}/n_p}$, where n_p is the number of superpixel in A_j. The factor $n_p^{-1/2}$ has to be included because $\bar{N}_{pix}$ is a *mean* of all superpixel in an annulus.

On the other hand, we lose information when we bin the data if the cluster is not elliptical. Thus, the number of annuli should be as high as possible in consideration of the increase of the computing time and the limited number of simulated points.

In the following, $\bar{S}_{X,j}$ is the mean of all $S_{X,i}$ in an annuli A_j. This mean and the standard deviation in each annuli leads to a surface brightness profile similar as shown in the left panel of figure 17. There are some points worth mentioning:

- In the profile above, we assumed that the position of the mean of each annuli is in between its outer and inner limit. There are always less points in the inner half of an annulus than in the outer half, since the size of this areas are not equal. Hence, we tried to take the median of the positions of all points in an annulus to represent its position in the profile. But this leads just to a small change in the central part. Again, a good balance between the resolution and the number of annuli can prevent this change almost completely.

- If the number of annuli is too small, there may be a deviation between the profile obtained above and the true profile along the major axis. The true profile simply gives the value of the X-ray surface brightness at a given radius. The binned profile gives $\bar{S}_{X,j}$, which represents all $S_{X,i}$ in the interval $r_j < r \leq r_{j+1}$. Thus, we should compare the binned data with

$$S_{X,int} = \frac{\int_0^{2\pi}\int_{r_j}^{r_{j+1}} S_X(r')\, r'\, dr'\, d\varphi}{\int_0^{2\pi}\int_{r_j}^{r_{j+1}} r'\, dr'\, d\varphi} = \frac{\int_0^{2\pi}\int_{r_j}^{r_{j+1}} S_X(r')\, r'\, dr'\, d\varphi}{\pi({r_{j+1}}^2 - {r_j}^2)} \tag{141}$$

  A suitable number of annuli helps to prevent this detour and we usually can compare the means with the true profile. This is also important when we try to fit the profile. If there is a large discrepancy between the means and the true profile, we can not use the analytic expressions we derived in this thesis to mimic the annuli since these continuous formulae do not take into account the discrete mean of a given interval.

The X-ray surface brightness profile allows to estimate the central surface brightness and model parameters as core radii and slopes. We use the `NonlinearModelFit`-function provided by Mathematica 7.0 to obtain the correct parameters.

4.2 Temperature profile

The simulation of a realistic temperature profile and a suitable fitting procedure to estimate the parameters are easily realized compared to the surface brightness. Now,

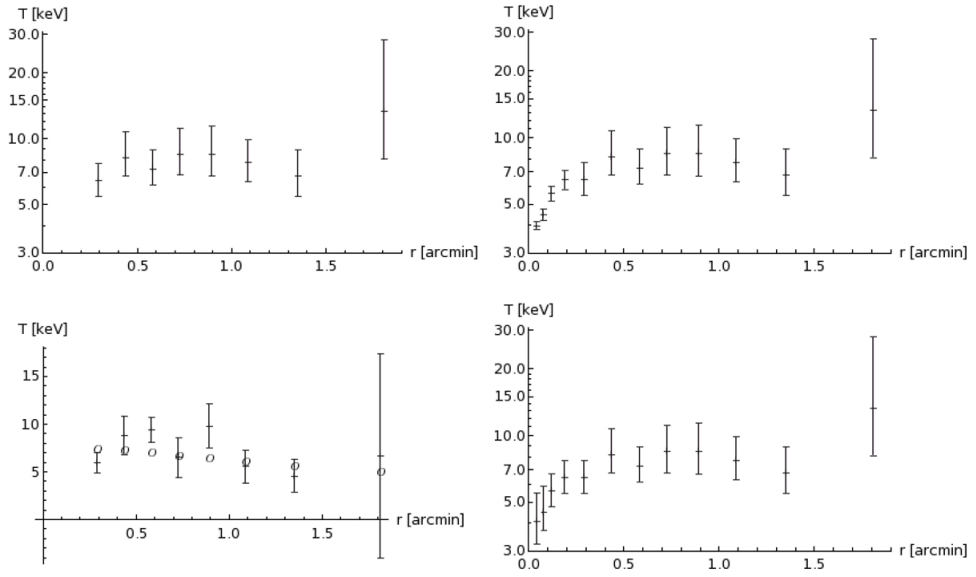

Figure 22: TOP LEFT: A logarithmic plot the temperature profile of Abell 1995, see table 7. BOTTOM LEFT: A simulated profile assuming a polytropic gas. The circle indicate the true polytropic profile with $T_0 = 8.61\,keV$ and $\gamma = 1.3$. TOP RIGHT: A logarithmic plot of a profile with a cool core added, A478 in [Vikhlinin 06]. BOTTOM RIGHT: The same profile as in the panel at top right, but with larger error bars at the center.

we have to take into account the difference between the physical temperature of the cluster and the spectroscopic temperature that we can measure. Therefore, we introduced the spectroscopic-like temperature T_{sl} in section 2.2. It gives the temperature that is actually measured.

4.2.1 Simulation

A1995 provides a measurement of the temperature profile. The low resolution and the large error bars, especially in the outer regions, are a realistic reference if we want to simulate a T-profile, figure 22. We simulate either polytropic profiles or profiles that include a cool core, $T_{Vik}(r)$. Hence, we need additional information about the measurements of a cool core cluster. [Vikhlinin 06] provides a lot of such observations. And we add the measurements of the core of A478 to the profile of A1995.

The simulation is performed within a few steps. First, we choose a model that describes the electron density of the gas and we decide whether the gas is polytropic or has a feature like a cool core, which is described by T_{Vik}. Then, we calculate the spectroscopic-like temperature profile T_{sl} along the major axis of the cluster. Finally, according to the data from Abell 1995, we resample the profile at several radii assuming that the given error is normal distributed. Figure 22 provides the measured profile of Abell 1995 and a simulated polytropic T-profile and a Vikhlinin T-profile with error bars.

4.2.2 Fitting procedure

In order to predict the parameters that describes the temperature profiles, we have to fit them with suitable models of T_{sl}. They are described by integrals of electron density and temperature. Their structure is similar to the integrals that are included in the expressions for the projected quantities: X-ray surface brightness and SZ-effect, as discussed in section 3.2. Since we were not able to give analytic expressions for arbitrarily powers of n_e and T, we will focus on fits with an isothermal and polytropic

gas.

Isothermal The fit by a constant temperature profile is done by the `LinearModelFit`-function provided by Mathematic 7.0. If the cluster is polytropic, the isothermal fit often underestimates the temperature normalization T_0, since it ignores the decrement of the gas temperature for larger radii. We will see that the isothermal assumption is often justified if the error on the measured T-profile is large.

Polytropic Now, we fit the simulated temperature profile with a suitable weighted T_{sl}. Since the polytropic temperature profile is a function of the electron density, we have to derive integrals of the form $\int_{los} n_e^m \, dl$, which we already discussed in section 3. The spectroscopic temperature T_{sl} is given by

$$T_{sl} = \frac{\int_{los} T \, n_e^2 / T^{3/4} \, dl}{\int_{los} n_e^2 \, T^{3/4} \, dl} = \frac{\int_{los} n_e^2 / T^{1/4} \, dl}{\int_{los} n_e^2 T^{-3/4} \, dl} = \frac{T_0}{n_{e0}^{\gamma-1}} \frac{\int_{los} n_e^{2+1/4(\gamma-1)} \, dl}{\int_{los} n_e^{2-3/4(\gamma-1)} \, dl}. \tag{142}$$

Thus, we can use the expressions derived in section 3.3 with indices $m = 2+1/4(\gamma-1)$ or $m = 2 - 3/4(\gamma - 1)$.

Next, we have to obtain the electron density parameters which describe the polytropic profile. We perform a isothermal fit of the surface brightness, $\gamma = 1$, and estimate these parameters up to 0^{th} order. Then, with the `NonlinearModelFit`-function provided by Mathematica 7.0, we are able to fit the simulated profile under the assumption that the gas is polytropic. To get a better estimate of γ, we can now perform a polytropic fit of the surface brightness profile. We could iterate several times to improve the estimation of the polytropic index and T_0. Moreover, we directly estimate also the surface brightness parameters. Now, we show that this estimation is similar to the results we obtain if we use the *true* electron density parameters.

We give an example in the case of a polytropic β-model. The initial assumptions are listed in section 4.5. After three iteration steps, we can compare the estimated elongation $e_{\Delta,3}$ with the result obtained by directly inserting the initial values of the electron density in the polytropic profile, $e_{\Delta,init}$:

$$\begin{aligned} e_{\Delta,true} &= 1.18 \\ e_{\Delta,3} &= 1.17 \pm 0.26 \\ e_{\Delta,init} &= 1.15 \pm 0.26 \end{aligned}$$

Both elongations are very close to the true value and both have almost the same standard deviation. Hence, we can avoid this iteration procedure. We directly insert the initial values without producing wrong results. In our further calculations, we will always estimate $e_{\Delta,init}$, see section 4.5 for an example. Of course, if real observations are analysed, we can't use the true values and the iteration procedure is the more consistent choice.

4.3 Sunyaev-Zeldovich effect

In this case, the simulation is very simple, since we are only interested in the central value. Due to the higher resolution and astrometric precision of the observations, we use the X-ray surface brightness map to estimate the electron model parameters.

To get a simulated value of the central temperature decrement, we calculate ΔT_0 where we insert our initial set of parameters and the desired electron density and

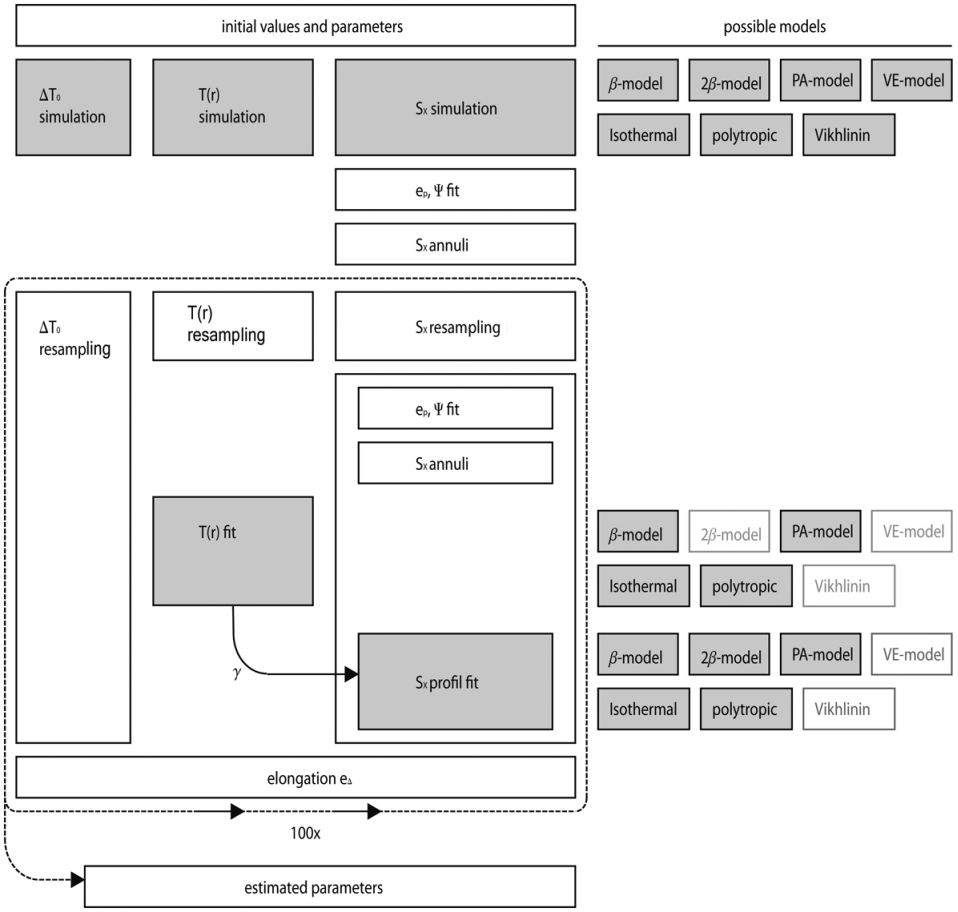

Figure 23: This scheme illustrates the steps that lead from initial assumptions to estimations of the parameters and their errors. On the right hand side, we list the possible electron density and temperature profiles we could use in the gray shaded step on the left hand side. In the fitting procedure, we only use the model combinations which we can describe by an analytic expression.

temperature models. Present day observations of the SZE embody an error of 10% to 20%, see [Bonamente]. Hence, we resample the true value of ΔT_0 to obtain the 'observed' value.

4.4 Combining the simulations

The diagram in figure 23 illustrates how the steps in the previews sections are arranged to receive the desired parameters and their uncertainties. Moreover, it shows the set of models that can be implemented in each step. Hence, a lot of ways to proceed are available. We present the whole procedure illustrated by a polytropic β-model in section 4.5.

First, we define the initial values and models and perform the simulation of the X-ray brightness map, the temperature profile and the temperature decrement. Next, the following steps are performed several times to obtain a consistent estimate of the final standard deviation of the fit parameters: We resample the temperature profile, the central temperature decrement and the surface brightness map and proceed as described above to get a set of parameters. In the polytropic case, we examine the surface brightness profile with a γ that is obtained through the temperature profile fit. We also include the elongation into the loop. Hence, after a number of runs that is high enough, we are able to include experimental noise correctly. The mean and the standard deviation of the final set of parameters give the values and the corresponding

e_p	Ψ	e_Δ
0.7172	56.87	1.184

Table 8: Quantities based on the geometric factors.

uncertainties.

4.5 Estimation of the Elongation: Example

We present an example which should illustrate how we get from the initial assumptions about our galaxy cluster to final considerations about the estimation of its shape. To keep it clear, we use the polytropic β-model. More complex temperature profiles and electron density models are included by using the analytic expressions we derived, but the way to proceed is exactly the same.

Initial values The physical constants are listed in appendix A. Now, we have to decide in which energy band we will perform the analysis. The A1995 data we got are limited to $0.7 - 7\,keV$, hence this should be a good choice. The parameter α, which occurs in the approximated cooling function $\Lambda(T, Z) = \tilde{\Lambda}(Z)T^\alpha$ of a gas, and hence the cooling function itself depends on the energy window and on the gas temperature and the metallicity of the plasma.

Let us list the parameters introduced in section 4.1.1 that describes one cluster of galaxies.

- the geometrical parameters
  $e_1 = 1.5, e_2 = 1.3, e_3 = 1, \theta_{Eu} = 60°, \varphi_{Eu} = 20°, \psi_{Eu} = 30°$.
- the model parameters
  $\theta_c = 1', \beta = 0.6$.
- the temperature parameters
  $T_0 = 10^8\,K = 8.61\,keV, \gamma = 1.3$
- additional parameters
  $\alpha = 0.25, \Lambda = 3.0 \times 10^{-27}\,erg\,s\,cm^3/K^\alpha, z = 0.5$

We will calculate n_{e0} based on an initial assumption about the photon counts. The temperature decreases to $T \sim 4\,keV$ at a radius of $r = 4\,r_c$. According to table 17 in the appendix, we choose $\alpha = 0.25$, assuming $Z = 0.3\,Z_\odot$.

Now, we are already able to compute quantities like the projected ellipticity e_p, the orientation Ψ and the elongation along the line of sight e_Δ, see table 8. All of them are just functions of the geometrical parameters.

At the end of this section, we will compare these values with those we will obtain through the fit.

Overall scaling Next, we use the Abell 1995 data file to calibrate our simulation of the X-ray surface brightness map. Our goal is to get a photon count per pixel that is comparable to real measurements. This is important so that we can compute the Poissonian noise correctly.

According to the binned Chandra data, we calculate the total number of photons N_c measured in the central superpixel of size $a_{pix} = 2" \times 2"$. For this purpose, we

extract the total exposure time E and the photon count n_c per *second* per $arcmin^2$ in the central annulus,

$$E = 57497\,s, n_c = 0.3607 \frac{cts}{s \times arcmin^2}, \tag{143}$$

$$N_c = E \times n_c \times a_{pix} = 23\,cts. \tag{144}$$

Now, we can complete our set of parameters. Starting from n_c, we can calculate the central surface brightness with webPIMMS. We enter our energy band, a galactic hydrogen column density ($n_H \sim 10^{21}\,cm^2$) and choose a temperature model, for example the bremsstrahlung model. We assume that the energy band dependence derived in [Ettori 00] and expressed though parameter α is included in this conversion procedure. Finally, we receive S_{X0} in *cgs*-units.

$$S_{X0} = 4.21 \times 10^{-12} \frac{ergs}{cm^2 \times s} \tag{145}$$

With this value, we solve the equation of S_{X0}, equation (70) with $\zeta = 0$, for n_{e0} and get our last initial parameter

$$n_{e0} = 0.0841\,cm^{-3}. \tag{146}$$

This value seems an order of magnitude larger than one would expect[16]. $n_{e0} \propto T^{\alpha/2}$ and hence, it depends on the correct choice of α. Ettori et al. provides this parameter only for few energy windows and cluster temperature ranges, but since n_{e0} is not of main interest in this thesis[17], we avoid further investigations. Moreover, the central electron density is also depending on the electron density model choice.

We get a conversion factor C that allows us convert from counts to *cgs*-units and vice versa.

$$C = \frac{S_{X0}}{n_c} = 1.83 \times 10^{13} \frac{ergs}{cts \times arcmin^2 \times cm^2 \times s} \tag{147}$$

We will use this factor to normalise our simulated central X-ray surface density considering N_c, the central photon count in the superpixel of the Abell 1995 measurement.

4.5.1 X-ray surface brightness simulation

To perform the simulation, we choose a map size of $5' \times 5'$, divided in 150^2 superpixel. Hence, we get a resolution of 2“, which is identical to the binning in the Abell 1995 file. Now, we calculate the surface brightness $S_{X,i}$ in each superpixel at position (x_i, y_i). From (70) we get

$$S_X(x_i, y_i) = \frac{\tilde{\Lambda}(Z)}{4\pi\,(1+z)^4} \frac{\sqrt{\pi}}{\sqrt{f}} \frac{\Gamma[-1/2 + 3\beta + 3/2\alpha(\gamma-1)\beta]}{\Gamma[3\beta + 3/2\alpha(\gamma-1)\beta]} \tag{148}$$

$$\times T_{e0}^{\alpha}\, n_{e0}^2\, r_c \left(1 + \frac{\xi_i^2}{r_c^2}\right)^{\frac{1}{2} - 3\beta - \frac{3}{2}\alpha(\gamma-1)\beta}, \tag{149}$$

We use the ellipsoidal radius ξ_i in the form defined in (56):

$$\xi_i^2 = (x_i \cos\Psi + y_i \sin\Psi)^2 \frac{f}{e_\Delta^2} + e_p^2(-x_i \sin\Psi + y_i \cos\Psi)^2 \frac{f}{e_\Delta^2}. \tag{150}$$

[16] [Bonamente] estimate $n_e 0 = 0.009\,cm^{-3}$.

[17] The central electron density cancels out in the expression for the elongation.

The inverse conversion factor times the exposure time ($C^{-1} \cdot E$) change the units of $S_{X,i}$ into total photon count per superpixel N_{pix}. The maximum is $N_c \sim 23\,cts$ and located at the center, as we assumed.

Thus, we can use the Mathematica-commands `PoissonianDistribution[`μ`]` and `RealInteger[]` to extract an integer that is Poissonian distributed around the mean μ. Thus, the simulated photon count with noise, let us call it the *observed* photon count $\tilde{N}_{pix}$, reads

$$\tilde{N}_{pix} = N_{pix} + \texttt{RealInteger[PoissonianDistribution[}N_{pix}\texttt{]]}. \tag{151}$$

At last, we get a X-ray surface brightness map in units of $cts/superpixel$, see figure 18.

Temperature profile To simulate the temperature profile we use the spectroscopic-like $T_{sl}(r)$, (142). Considering a polytropic β-model, we integrate $T_{sl}(r)$ along the line of sight. To obtain a realistic simulation, we simulate the profile at the radii r_i of the A1995 observations. Table 7 lists the radii, the measured temperatures at those position and their error.

Then, T_{sl} at radius r_i is given by

$$T_{sl}(r_i) = \frac{T_0}{n_{e0}^{\gamma-1}} \frac{\int_{los} \left(1 + \left((r_i + z')/r_c^2\right)\right)^{-\frac{3\beta}{2}(2+1/4(\gamma-1))} dz'}{\int_{los} \left(1 + ((r_i + z')/r_c^2)\right)^{-\frac{3\beta}{2}(2-3/4(\gamma-1))} dz'}. \tag{152}$$

At the positions r_i, we resample T_{sl} assuming a normal distributed error. Let's call this resampled profile the *observed* temperature profile.

Central temperature decrement Equation (73) gives the central temperature decrement. With our initial values, whose central electron density we calculated based on the assumed photon count, we obtain

$$\Delta T_0 = -11.9\,mK. \tag{153}$$

The error $\sigma_{\Delta T}/\Delta T$ is usually around 10%. A wrong estimation of n_{e0} would lead to a wrong temperature decrement[18]. But since we are focusing on the cluster shape, which is not explicitly depending on n_{e0}, only the relative error on ΔT_0 is important. If our analysis is consitent, this should not play a role. Finally, we extract our *observed* temperature decrement from a normal distribution with mean ΔT_0 and standard deviation $\sigma_{\Delta T}$.

4.5.2 Fitting procedure

Now, we will estimate the parameters from the analysis of the observed quantities. To obtain consistent errors we resample all the observed data several times. Thus, we establish a loop which will estimate the parameters after each resampling.

First of all, we try to estimate the polytropic index from the observed temperature profile. In the case of the polytropic β-model, T_{sl} can be written as

$$T_{sl} = \frac{T_0}{n_{e0}^{\gamma-1}} \frac{\frac{\Gamma[-1/2+3\beta m]}{\Gamma[3\beta m]} \left(1 + \frac{\xi^2}{r_c^2}\right)^{\frac{1}{2}-3\beta m} |_{m \to 2+1/4(\gamma-1)}}{\frac{\Gamma[-1/2+3\beta m]}{\Gamma[3\beta m]} \left(1 + \frac{\xi^2}{r_c^2}\right)^{\frac{1}{2}-3\beta m} |_{m \to 2-3/4(\gamma-1)}} \tag{154}$$

[18] [Bonamente] found $\Delta T_0 = -0.92\,mK$ in A1995.

	initial	isothermal	polytr. ($\bar{\sigma}$)	polytr. ($1/4\bar{\sigma}$)
$T_0\,[keV]$	8.61	6.7 ± 0.7	10 ± 4	8.7 ± 0.8
γ	1.3	1	1.5 ± 0.5	1.4 ± 0.1
BIC ($\bar{\sigma}$)		35	39	-
BIC ($1/4\sigma$)		70	-	67

Table 9: The fit parameters assuming an isothermal and a polytropic gas. The errors of the parameters are very large in the polytropic case with $\bar{\sigma} \sim 2\,keV$. To obtain of parameters that describe a polytropic gas better, we assume that the errors on the temperature measurement are 1/4 of the given ones, $\sigma_{T(r)} = 0.5\,keV$. A comparison with the BIC reveals the one that should be preferred.

If we use this function to obtain T_0 and γ, we have to check if their estimated errors are not too large. Since the reference errors of the Abell 1995 profile are quite large, their mean is $\bar{\sigma} \sim 2\,keV$, we are usually not able to fit with a polytropic profile and we have to change to an isothermal one. Only if we assume that the accuracy of the measurements reaches a certain level, we can perform a polytropic fit and obtain the index γ. In addition, we can use the *BIC*, the Bayesian information criterion, to estimate the number of parameters we can actually fit.

The formula for the BIC is

$$\texttt{BIC} = -2 \ln L + k \ln(n) \tag{155}$$

where L is the maximized value of the likelihood function for the estimated model, k is the number of free parameters of the model and n the number of data points used in the fit, see [Liddle] and references therein. We used the command in Mathematica.

This facts tells us which temperature profile we have to assume for the rest of the fitting procedure.

If we perform this fitting with the initial parameters - we skip an iteration procedure as described in section 4.2.2 - we get the results in table 9. We see that in this case, we should prefer the isothermal model since the polytropic parameters can not be estimated. For example, if we assume that the errors on the measurements are 1/4 of the given errors, $\sigma_{T(r)} \sim 0.5\,keV$, we are able to fit a polytropic profile. Hence, we fit once with the polytropic gas and small errors on $T(r)$ and once with the isothermal assumption, but $\sigma_{T(r)} \sim 2\,keV$.

From the surface brightness map, we can estimate the ellipticity and the orientation of the projected ellipsoid. This procedure is model independent. With this information, we produce annuli. Hence, we get a surface brightness profile as shown in figure 17.

In the fitting procedure of the surface brightness profile, the errors on the annuli are given by $\sqrt{\bar{N}_{pix}/n_{pix}}$, whereas $\bar{N}_{pix}$ is the averaged photon count per superpixel in an annulus which embodies n_{pix} superpixel. We use this information to weight the fit correctly. A fit provides an estimate of the projected core radius r_p, the slope β and the *central* surface brightness in units of total counts per superpixel. We use the conversion factor C and the size of a superpixel to get an expression in *cgs*-units, S_{X0}.

To get the elongation of a polytropic β-model, we insert $r_c/\sqrt{f} = r_p/e_\Delta$ in (71) and (73). Out of them, we calculate $S_{X0}/\Delta T_0$ and solve for e_Δ. Here, we used that the surface brightness and temperature decrement depend differently on the electron

	e_p	Ψ	$r_p[arcmin]$	β
true	0.71	56.87	0.946	0.6
isothermal	0.719 ± 0.014	55.6 ± 1.7	0.95 ± 0.02	0.62 ± 0.01
polytr. ($\sigma_{1/4}$)	0.719 ± 0.014	55.6 ± 1.7	0.93 ± 0.02	0.59 ± 0.01
	$S_{X0}[\frac{10^{-12} erg}{cm^2\, arcmin^2\, s}]$	$T_0[keV]$	γ	e_Δ
true	4.21	8.61	1.3	1.184
isothermal	4.20 ± 0.05	6.2 ± 0.1	1	1.3 ± 0.4
polytr. ($\sigma_{1/4}$)	4.21 ± 0.05	9.0 ± 0.6	1.34 ± 0.08	1.2 ± 0.2

Table 10: The fit parameters assuming an isothermal gas and assuming a polytropic gas, whereas we assume that the error on the observed temperature is $\sigma_{T(r)} = 0.5\, keV$ in the second case.

density, as discussed in section 1.2.5. Then, the elongation is given by

$$e_\Delta = \frac{S_{X0}}{\Delta T_0^2} \frac{4\pi(1+z)^4}{\tilde{\Lambda} T_0^\alpha} \left(T_{CMB}\, f_{SZ}(\nu, T_e) \frac{\sigma_T k_B}{m_e c^2} \right)^2 T_0^2 r_p \tag{156}$$

$$\times \left(\frac{\Gamma[-1/2 + 3\gamma\beta/2]}{\Gamma[3\gamma\beta/2]} \right)^2 \frac{\Gamma[3m\beta/2]}{\Gamma[-1/2 + 3m\beta/2]}, \tag{157}$$

where $m = 2 + \alpha(\gamma - 1)$. We have to keep in mind that the factor 4π, which is originated in the integration to obtain the surface brightness, is a solid angle. Since S_{X0} is expressed in $arcmin^2$, we should insert

$$4\pi\, sr = 180/\pi \cdot 60\, arcmin^2 \tag{158}$$

Finally, we can estimate the elongation.

This is the end of the fitting procedure and we start a new loop to estimate the parameters based on a new resampeling of the observed values. The fit parameters we obtain are listed in table 10. In this table, we see that the estimation of orientation and ellipticity is quiet exact. Core radius and central X-ray surface brightness agree with the true value. But there are also differences between isothermal and polytropic assumption. The slope parameter β is overestimated in the isothermal case. Both β and the polytropic index γ control the slope of the surface brightness. Hence, this overestimation can be a compensation of the underestimated γ. The isothermal profile is not able to estimate the central temperature correctly. This is originated in the fact that the polytropic profile usually decreases with radius and the isothermal fit gives the average temperature and not the central one. The polytropic profile is able to give a good estimation of T_0. Surprisingly, both models constrain the elongation quiet good. Obviously, the underestimated temperature is able to compensate the β and γ parameters in the isothermal case.

The polytropic fit tells us the the method we use to estimate the elongation works correctly. Moreover, we see that the isothermal assumption can also be a good choice.

In figure 24, we see the distribution of the fitted parameters of each loop around the true values. This is a good tool to estimate if the fitting procedure works correctly. As we expect, the distributions are almost symmetric, their median is close to their mean. In addition, we give the distributions of the values that differ in the isothermal case.

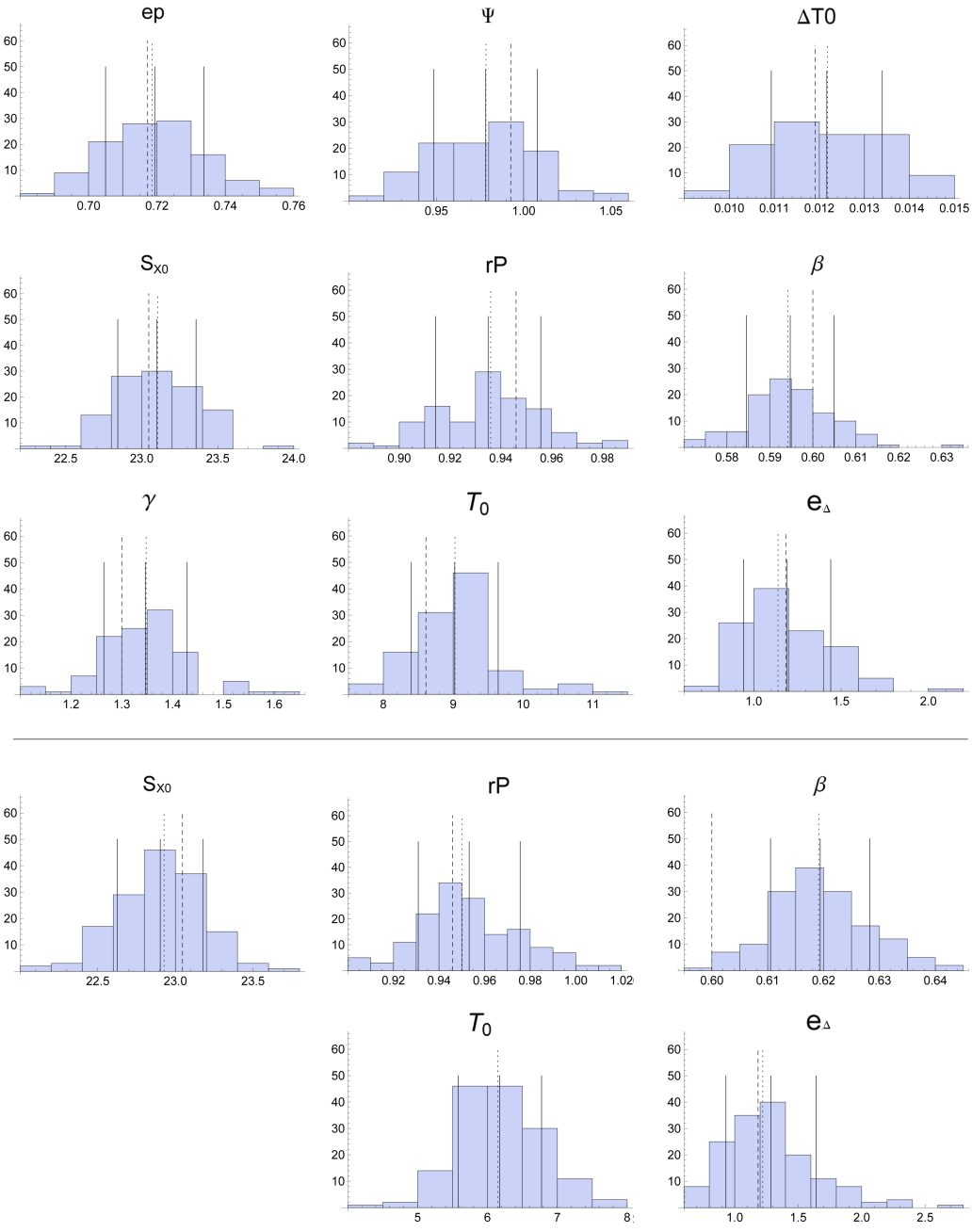

Figure 24: TOP: The distribution of parameters estimated in $\sim$ 100 runs where we tried to fit a cluster described by a polytropic β-model. We took the same model to obtain the parameters assuming the error on the temperature profile is $\sigma_{T(r)} \sim 0.5\, keV$. The dashed line indicates the true value of the parameter, the central drawn through line gives the mean of all runs, the other drawn through lines are the standard deviation on this distribution. The dotted line is the median and should correspond with the mean if the distribution is Gaussian. The true values coincide with the 1σ confidence interval, as we expect, because we choose the right model. The coordinates along the axis of abscissa are given in the following units: $T_0[keV]$, $\Delta T_0[K]$, $r_p[r_c]$, $S_{X0}[cts/superpixel]$, $\Psi[rad]$. BOTTOM: Five parameters in the case of a isothermal β-model fit and $\sigma_{T(r)} \sim 2\, keV$. Although it is the wrong model, wet get a good estimation of the elongation, but we miss the slope parameter β and the central temperature.

4.6 Results

Now, we want to use the procedure which we described above to search for general features when we estimate the elongation through fitting a certain model on the measured data. Our goal is to understand how the estimation of the cluster shape depends on the accuracy of the measurements and on the models which we use to fit the observed data. Starting from different initial values, electron density models, temperature profiles and error assumptions, the number of possible configurations is very large. We try to limit our analysis to interesting and important combinations.

4.6.1 β-model, polytropic

This case has already been examined above in section 4.5. The polytropic model and the isothermal assumption lead both to a good estimation of the elongation. Now, we will examine which assumptions this result depends on.

The elongation of this model was derived above as:

$$e_\Delta = \frac{S_{X0}}{\Delta T_0^2} \frac{4\pi(1+z)^4}{\tilde{\Lambda} T_0^\alpha} \left(T_{CMB}\, f_{SZ}(\nu, T_e) \frac{\sigma_T k_B}{m_e c^2} \right)^2 \tag{159}$$

$$\times \left(\frac{\Gamma[-1/2 + 3\gamma\beta/2]}{\Gamma[3\gamma\beta/2]} \right)^2 \frac{\Gamma[3m\beta/2]}{\Gamma[-1/2 + 3m\beta/2]}, \tag{160}$$

We can identify which parameters affect the elongation most. e_Δ is inversely proportional to the square of the temperature decrement. Hence, a large error on ΔT_0 can shift the estimated elongation, because usually, its relative measurement error is of the order of $10\% - 20\%$. In the example in table 9, we have seen that different temperature profiles can lead to different central temperature estimations. We expect that T_0^α also plays an important role. These statements are model independent, of course. The other parameters, the surface brightness or the core radius, are given by the surface brightness fit, and have an effect too.

Now, we study how the elongation depends on the error on the temperature profile measurement and on the error on the temperature decrement. Our initial assumptions are $\bar{\sigma}_{T(r)} \sim 2\, keV$, where the errors are distributed according to A1995, and $\sigma_{\Delta T_0}/\Delta T_0 \sim 10\%$. We run the loop with different errors that depart from this initial values and observe how the estimation of the elongation changes. We expect that the statistical error on the elongation and its deviation from the true value will decrease if we decrease the errors. If the error of one of these quantities gets very small, there might be a threshold where the error on the elongation will be almost constant. That means, the other measurement errors become dominant.

Error on the temperature profile We fit the simulated data assuming an average error on the temperature profile in between

$$\sigma = [0.17\, keV, 2.5\, keV] \tag{161}$$

in steps of $\sim 0.2\, keV$. First, we use the polytropic profile even though the isothermal model could be a better choice in the case of large errors. But in this way, we can compare the influence of different errors on the elongation. If the fitting procedure fails, we discard the run and start a new resampling. Then, we examine the behaviour of the fit if we assume a constant temperature in the cluster.

In the case of large errors on the temperature measurements, $\sigma_{T(r)} \sim 2\, keV$, we expect that both models can give a good estimate of the elongation, as we saw in the

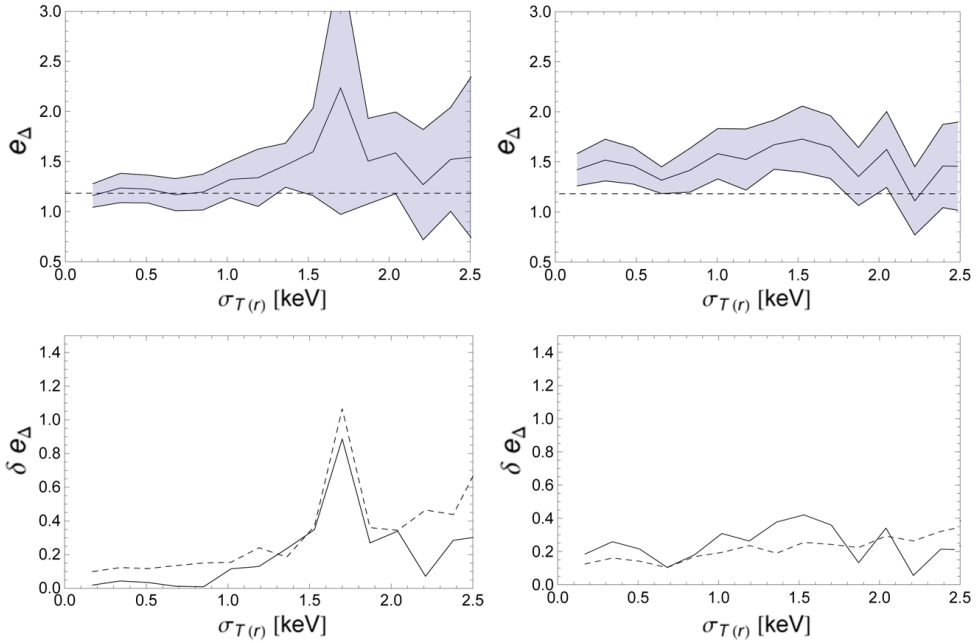

Figure 25: A cluster described by a polytropic β-model. The estimated elongation changes if the error on the temperature profile $\sigma_{T(r)}$ changes. The relative error on the temperature decrement is 10%. TOP LEFT: The polytropic β-model gives a good fit if the error on $T(r)$ is small. This shows again that our method works correctly. At $1.7\,keV$, the large deviation is a statistical fluctuation. The dashed line indicates the true elongation. BOTTOM LEFT: The statistical error (dashed line) and the deviation from the true value (drawn though line) in the polytropic case relative to the true e_Δ. The statistical error decreses by a factor ~ 5 while the deviation between true and estimated elongation is very small if $\sigma_{T(r)} < 1\,keV$. TOP RIGHT: The isothermal β-model gives a good fit if the error on $T(r)$ is large enough. Then, it's possible that assuming a constant temperature profile compensates other effects. If $\sigma_{T(r)} < 1.5\,keV$, there is a systematic error. Probably, the small errors on $T(r)$ do not allow to estimate a T_0 that leads to a e_Δ close to the true elongation, indicated by the dashed line. BOTTOM LEFT: The statistical error (dashed line) and the deviation from the true value (drawn though line) in the isothermal case relative to the true e_Δ. The statistical error decreses by a factor ~ 2 while the deviation between true and estimated elongation is always of the same order of magnitude.

example above. Otherwise, the polytropic gas will give a better fit.

In the following paragraphs, the difference between the true elongation and the estimated elongation is called *deviation*. Figure 25 shows that the systematic error and the deviation in the polytropic case decrease significantly if we assume a smaller error $\sigma_{T(r)} < 1\,keV$ on the temperature profile. Otherwise, the estimation of the correct temperature parameters becomes difficult and statistical error on the elongation increases. If we try to fit with the isothermal model, the statistical error will not increase very much. If $\sigma_{T(r)}$ is large enough, $\sigma_{T(r)} \geq 1\,keV$ the measured temperature profile could lead to an estimation of the elongation that is as good as the one in the polytropic case, whereas the relative statistical error is $\delta e_\Delta/\Delta T_0 \sim 0.4 e_\Delta$. On the other hand, if the error on $T(r)$ is small, the isothermal model overestimates the elongation. In the example discussed above, we assumed $\sigma_{T(r)} \sim 2\,keV$ and therefore, the isothermal profile can give a good fit.

Error on the central temperature decrement We investigate the dependence of the elongation on the error on the SZ temperature decrement. We vary $\sigma_{\Delta T_0}/\Delta T_0$ between 1% and 25%, while we assume that $\sigma_{T(r)} \sim 1\,keV$. The relationship between elongation and ΔT_0 is

$$e_\Delta \propto \frac{1}{\Delta T_0^2}. \tag{162}$$

Hence, we expect that the error on the elongation rapidly decrease until it becomes smaller that the statistical error due to the other parameters. The deviation from the true elongation decreases too, since the simulated temperature decrement gets closer to the true value.

Figure 27 illustrates the behaviour of the estimated elongation when we change the error on the temperature decrement measurement. As expected, a small error on ΔT_0 guarantees a good and accurate estimate. Already at $\sigma_{\Delta T}/\Delta T_0 \sim 10\%$, the elongation can deviate by 25% from the true value. This makes it sometimes difficult to interpret results. If $\sigma_{\Delta T_0}$ is even larger, a good estimation of e_Δ is not always possible and the statistical error becomes larger than $0.5 e_\Delta$. Hence, to guarantee an accurate estimation of the elongation within $\sim 20\%$ in our case, we need $\sigma_{\Delta T_0} < 5\%$. Of course, this relative accuracy is not a general result and should be tested for clusters with other elongations.

In both examples above, where we varied the error on $T(r)$ and ΔT_0, we resampled the true temperature profile or the temperature decrement in each step. Hence, every variation belongs to a new observation of those quantities. Due to this, there is always a certain uncertainty background in those plots. In figure 26 and 28, we fixed these errors and made several runs. We see that each new resampling leads to a slightly different estimation of the elongation.

Polytropic profiles As observed in the example above, the isothermal β model seems to fit a polytropic model quite well, as far es the elongation is concerned. To examine the dependence of the elongation on the fitted polytropic index a bit more, we choose a fix index γ, estimate the corresponding temperature and fit the surface brightness. We expect that the best estimation is possible at $\gamma = 1.3$ while the systematic error will increase if γ changes.

The panels in figure 29 present two different cases. The top one gives the behaviour of the elongation if we assume that the central temperature is exactly known, $T_0 = 8.61\, keV$. Hence, this is the dependence of e_Δ on the polytropic index γ. The bottom panel shows the case in which we choose γ and fit the temperature profile, whereas $\sigma_{T(r)} \sim 2\, keV$. We observe the effect we already have seen in the example above: the estimated temperature compensates the wrong model, whereas it does not matter which polytropic index we choose. To avoid too wide scattering due to the estimation of the temperature decrement, we assume a error of 5% on ΔT_0. In the isothermal case, $\gamma = 1$, the elongation deviates a bit from the true value, in contradiction to the agreement observed in our example. But since we choose a smaller error on ΔT_0 and perform a different simulation, we should not compare those scenarios directly. Moreover, a large error on T(r) does not have to give a good estimation of the elongation in all cases, see top right panel in figure 25.

Conclusion If the true cluster is described by a polytropic β-model, and isothermal β-model can estimate the elongation correctly if the error on the temperature profile larger than $\sigma_{T(r)} \sim 2\, keV$. Otherwise, the isothermal model tends to overestimate the elongation e_Δ. Hence, a temperature profile that is too simple can be a source of error if the temperature measurement has a certain accuracy.

4.6.2 PA-model, polytropic

In the case of a cluster described by a polytropic β-model, we compared the influence of the choice of the temperature model on the estimated elongation. Now, in the case of the PA-model, we can compare both the electron density models and the temperature

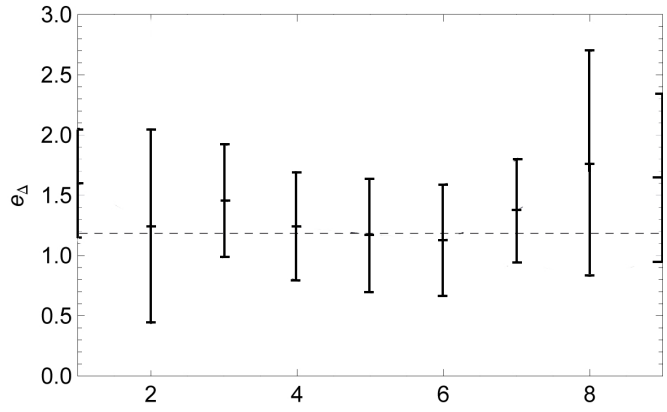

Figure 26: A polytropic β-model cluster several times fitted with a polytropic β-model. $\sigma_{T(r)} \sim 2\,keV$ and $\sigma_{\Delta T_0}/\Delta T_0 = 10\%$, whereas we resample the true temperature profile at each step. The dashed line donotes the true elongation.

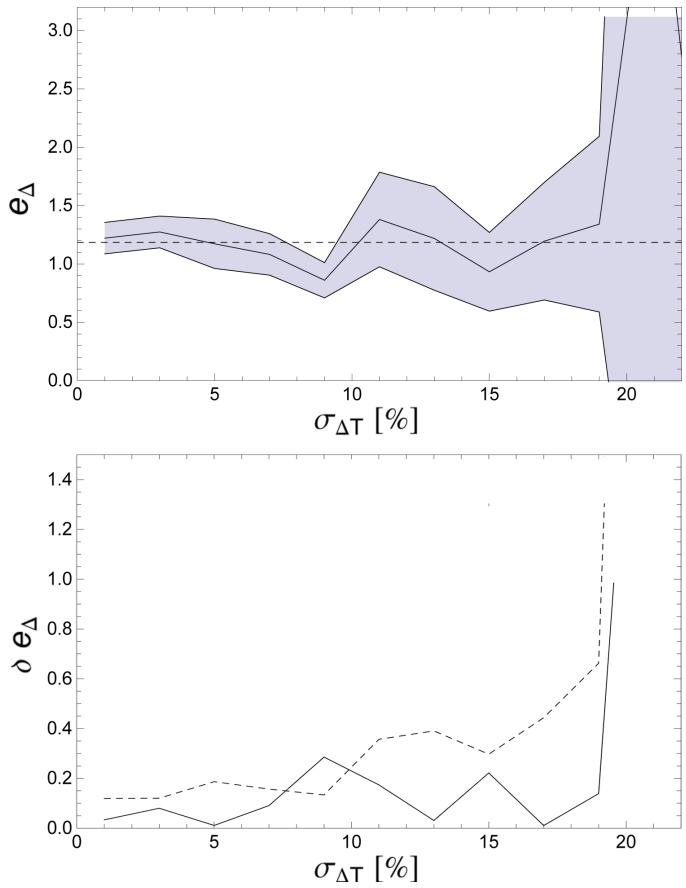

Figure 27: A cluster described by a polytropic β-model. The estimated elongation changes if the error on the central temperature decrement ΔT_0 changes. The error on the temperature profile is $\sigma_{T(r)} = 0.8$ in average. TOP : The polytropic β-model gives a good fit if the error on ΔT_0 is small. At $\sigma_{\Delta T_0} > 20\%$, a wide scattering of the estimate value is possible. The dashed line indicates the true elongation. BOTTOM: The statistical error (dashed line) and the deviation from the true value (drawn though line) relative to the true e_Δ. The statistical error decreses by a factor ~ 6 while the deviation between true and estimated elongation is of the same order if $\sigma_{\Delta T_0} < 18\%$.

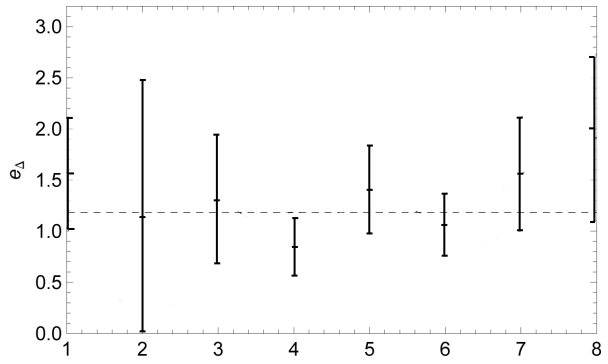

Figure 28: A polytropic β-model cluster several times fitted with a polytropic β-model. $\sigma_{T(r)} \sim 0.8\,keV$ and $\sigma_{\Delta T_0}/\Delta T_0 = 10\%$, whereas we resample the true central temperature decrement at each step. The dashed line denotes the true elongation.

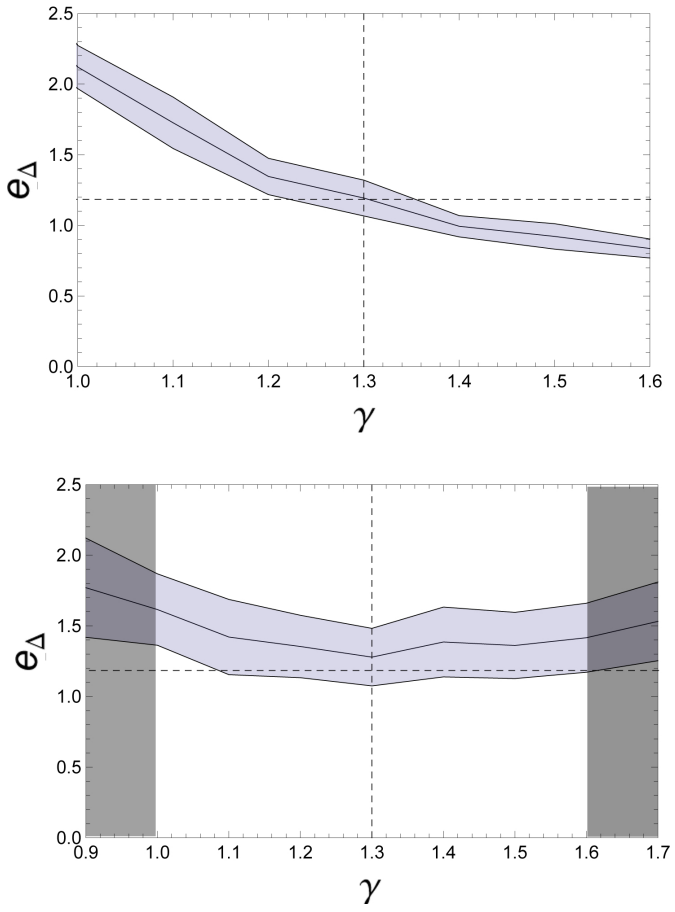

Figure 29: TOP: The behaviour of the elongation if we change the polytropic index from 1 to 1.6 and assume that the temperature is fixed at $T_0 = 8.61\,keV$. The true values of elongation and the true polytropic index are denoted by the dashed lines. BOTTOM: Here, the temperature is not fixed anymore. Moreover, we use a fixed γ to obtain a T_0 by fitting the given temperature profile with $\sigma_{T(r)} = 2\,keV$. The shaded regions indicates regions that are not plotted in the figure above. Although the best fit is possible if the model is correct, we see that a good estimate of the elongation is possible, whatever index we choose.

	e_Δ	δ
true cluster	1.18	
PA polytropic	1.3 ± 0.3	0.47
PA isothermal	1.2 ± 0.3	0.24
β polytropic	0.9 ± 0.2	-1.20
β isothermal	1.2 ± 0.2	-0.10

Table 11: The elongation obtained when we fit a cluster described by a polytropic PA-model under different model assumptions. δ gives the difference between estimated and true elongation in units of the estimated standard deviation.

models. Remembering the hierarchical structure of the n_e-models, the PA-model has one additional parameter η which describes a peak at the center.

All initial parameters are identical with the values we used in the example with the polytropic β-model. Our analytic expressions which describe surface brightness and temperature decrement in the case of a polytropic PA-model require $0 < \eta < 1$. Hence, we choose

$$\eta = \frac{1}{2} \tag{163}$$

The elongation of a cluster described by a polytropic PA-model is given by

$$e_\Delta = \frac{S_{X0}}{\Delta T_0^2} \frac{4\pi(1+z)^4}{\tilde{\Lambda} T_0^\alpha} \left(T_{CMB}\, f_{SZ}(\nu, T_e) \frac{\sigma_T k_B}{m_e c^2} \right)^2 T_0^2 r_p \tag{164}$$

$$\times \left(\frac{\Gamma[-1/2 + 3\gamma\beta/2]}{\Gamma[3\gamma\beta/2]} \right)^2 \frac{\Gamma[3m\beta/2]}{\Gamma[-1/2 + 3m\beta/2]} \tag{165}$$

$$\times {}_2F_1\left[\frac{\gamma\eta}{4}, -\frac{1}{2}(1 - 3\gamma\beta), \frac{3\gamma\beta}{2}, 1 \right]^2 {}_2F_1\left[\frac{m\eta}{4}, -\frac{1}{2}(1 - 3m\beta), \frac{3m\beta}{2}, 1 \right]^{-1} \tag{166}$$

whereas $m = 2 + \alpha(\gamma - 1)$.

If we fit the polytropic PA-model with a isothermal PA-model or a polytropic β-model, we expect that these simpler models will estimate the elongation correctly, similar as in the case before where we fit a polytropic β-model with a isothermal β-model. Assuming $\sigma_{\Delta T_0}/\Delta T_0 = 10\%$ and $\sigma_{T(r)} \sim 1\, keV$, we can estimate the elongation in those different cases, table 11.

The simpler models are able to estimate the elongation correctly. The polytropic β-model is an exception, because it is outside of the 1σ interval. But this is still a good result. It is interesting that the isothermal β-model seems to fit better than we would expect. Maybe, it is a coincidence due to the simulated temperature profile. Further research would answer this question. But in the following, we focus on the polytropic and isothermal PA-model. Let us see if there is a similar dependence on the error on the temperature profile and the SZ temperature decrement.

Error on the temperature profile While the error on the temperature decrement is 10%, we vary the error on $T(r)$ in a similar interval as in the previous section:

$$\sigma = [0.17\, keV, 1.7\, keV] \tag{167}$$

We expect a similar behaviour of the estimated elongation if we compare the isothermal and polytropic profile. Figure 30 shows the results. Again, we can say that as long as $\sigma_{T(r)} < 1\, keV$, we get a better estimate of the elongation if we use a polytropic model. The isothermal model seems to overestimate the cluster elongation. But the difference is not as large as in the case of the polytropic β-model above. If $\sigma_{T(r)} > 1\, keV$, there

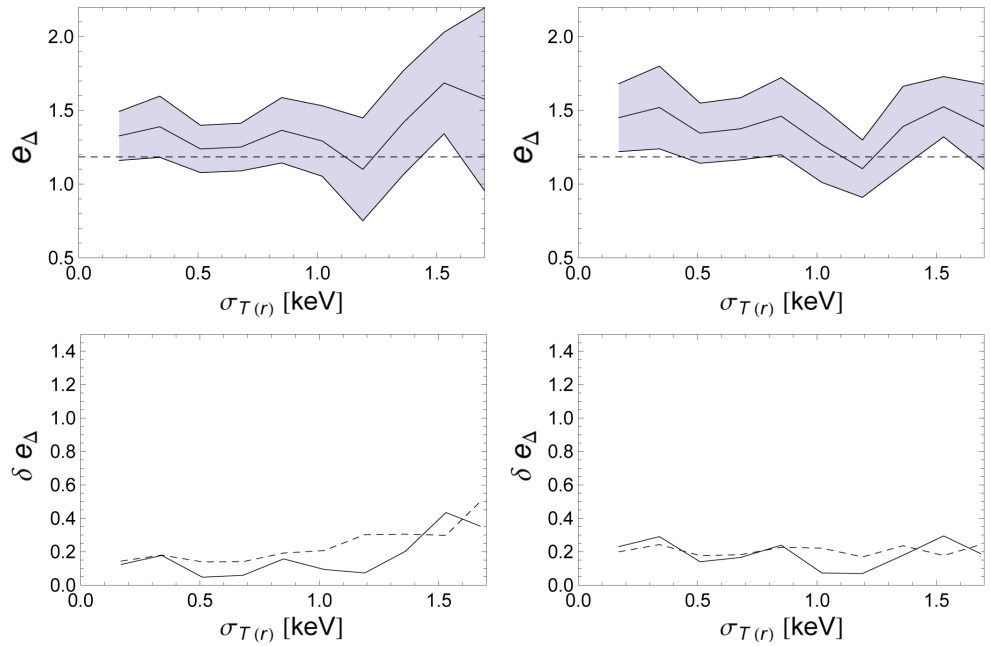

Figure 30: A cluster described by a polytropic PA-model. The estimated elongation changes if the error on the temperature profile $\sigma_{T(r)}$ changes. The error on the temperature decrement is 10%. TOP LEFT: The polytropic PA-model gives a good fit if the error on $T(r)$ is smaller than $\sim 1\,keV$. The dashed line indicates the true elongation. BOTTOM LEFT: The statistical error (dashed line) and the deviation from the true value (drawn though line) in the polytropic case relative to the true e_Δ. The statistical error decreses by a factor ~ 2 while the deviation between true and estimated elongation is around $0.2e_\Delta$ if $\sigma_{T(r)} < 1\,keV$. TOP RIGHT: The isothermal PA-model can give a good fit if the error on $T(r)$ is large enough. Then, it is obviously possible that assuming a constant temperature profile compensates other effects. If the error on $T(r)$ is small, a systematic error occurs similar as in the β-model case. The dashed line indicates the true elongation. BOTTOM LEFT: The statistical error (dashed line) and the deviation from the true value (drawn though line) in the isothermal case relative to the true e_Δ. The statistical error is almost constant while the deviation between true and estimated elongation is always of the same order of magnitude and comparable to the polytropic case.

is no advantage in using a polytropic temperature model instead of a constant one. The plots are consistent with the values derived in table 11.

Error on the central temperature decrement Again, we vary $\sigma_{\Delta T_0}$ between 1% and 25%, while we assume that $\sigma_{T(r)} \sim 0.5\,keV$. We choose a smaller error on $T(r)$ than before so that we can focus on the influence of $\sigma_{\Delta T_0}$.

Figure 31 illustrates the behaviour of the estimated elongation when we change the error on the temperature decrement measurement. As expected, a small error on ΔT_0 guarantees a good and accurate estimate. If $\sigma_{\Delta T_0} > 15\%$, the statistical error $\delta e_\Delta / e_\Delta$ becomes larger than $0.5 e_\Delta$, while the deviation from the true elongation is always of the same order of magnitude. Hence, to guarantee an accurate measurement of the elongation with a relative error of 20%, we need $\sigma_{\Delta T_0} < 10\%$. As before, this statement holds only in this example. Compared to the β-model case in the previous section, we can allow a similar error on ΔT_0.

Parameter η In the case of the β-model, we compared the polytropic temperature profiles by varying the polytropic index γ, whereas $\sigma_{T(r)} \sim 0.5\,keV$ and $\sigma_{\Delta T_0}/\Delta T_0 = 10\%$. Now, we want to examine the behaviour of the elongation if we change η in our PA-model. Figure 32 shows that a small parameter η tends to underestimate e_Δ while a larger η would result in a larger estimated elongation. In addition, the statistical error increases. This compensating effect explains the good elongation we estimate

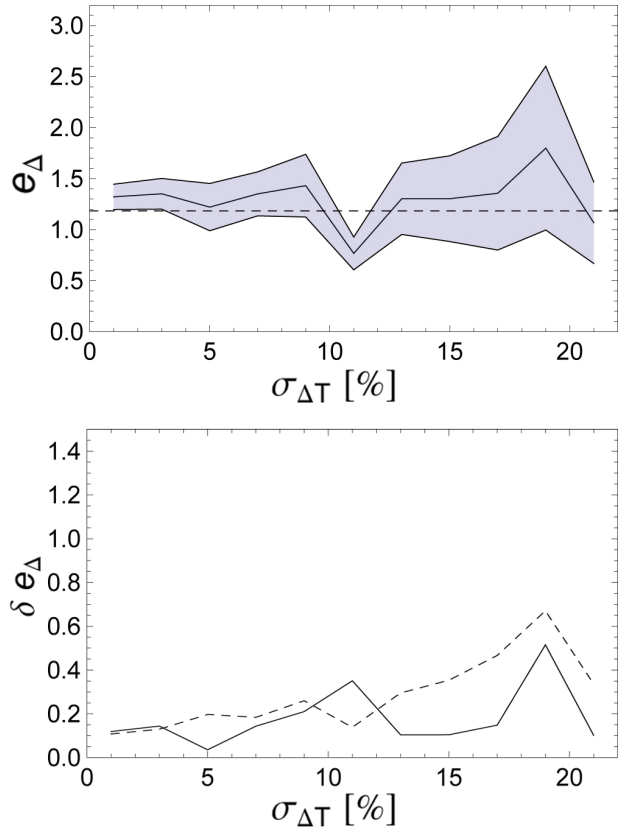

Figure 31: A cluster described by a polytropic PA-model. The estimated elongation changes if the error on the central temperature decrement ΔT_0 changes. The error on the temperature profile is $\sigma_{T(r)} = 0.4$ in average. TOP : The polytropic PA-model gives a good estimation if the error on ΔT_0 is small. The dashed line indicates the true elongation. BOTTOM: The statistical error (dashed line) and the deviation from the true value (drawn though line) relative to the true e_Δ. The statistical error decreases by a factor ~ 4 while the deviation between true and estimated elongation is of the same order.

if we use a polytropic β-model, where $\eta = 0$. Probably, it is originated in a certain degeneracy among η and the slope parameter β, which occurs if the peak parameter η is small.

Conclusion The elongation of a cluster described by polytropic PA-model can be estimated through a fit with a isothermal β-model if $\sigma_{\Delta T_0}/\Delta T_0 = 10\%$ and $\sigma_{T(r)} \sim 0.8\, keV$. Hence, the flat β-model is able to fit the cluster although there is a peak in the electron density. If we compare polytropic and isothermal PA-model fits, we observe a systematic error in the deviation if $\sigma_{T(r)} < 1\, keV$ in the isothermal case. We have observed this overestimation already in the β-model example.

4.6.3 PA-model with cool core

In our previous analysis, we focused on polytropic models. These models have temperature profiles which are a simple power law of the electron density. Now, we will simulate cool core clusters whose temperature profiles is described by the simplified Vikhlinin profile, see equation (41). The electron density is given by the PA-model. Since we found no analytic expression to express X-ray surface brightness or the central temperature decrement if the Vikhlinin profile is involved, we will fit this cluster with polytropic models. Maybe some compensating effects will occur so that we still get a good estimation of the elongation.

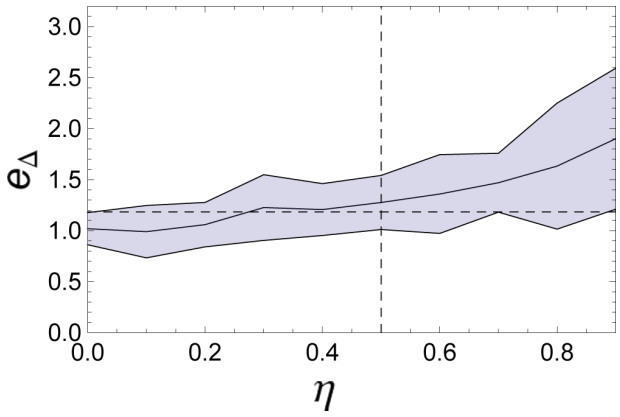

Figure 32: A cluster described by a polytropic PA-model fitted with a polytropic PA-model, where η varies between 1 and 0.9. Compared to figure 29, where we varied the polytropic index fitting a polytropic β-model, we observe also compensating effect if we change η. The dashed lines indicate the parameters that belong to the true model.

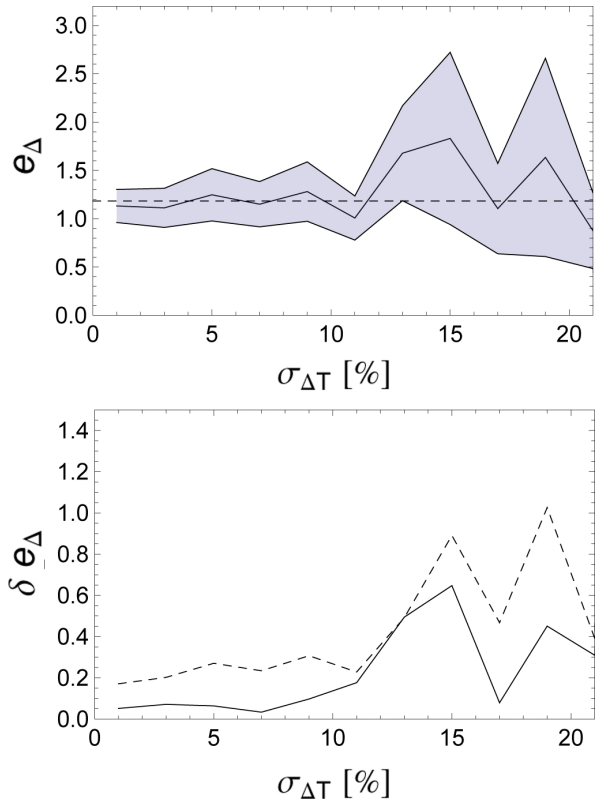

Figure 33: A cluster described by a PA-model and a Vikhlinin temperature model, where the error on the cool core measurements is assumed to be as large as on the other measurements. The estimated elongation changes if the error on the central temperature decrement ΔT_0 changes. The error on the temperature profile is $\sigma_{T(r)} = 0.5$ in average. TOP : The polytropic PA-model gives a good estimation if the error on ΔT_0 is small. The dashed line indicates the true elongation. BOTTOM: The statistical error (dashed line) and the deviation from the true value (drawn though line) relative to the true e_Δ. The statistical error decreases by a factor ~ 4 while the deviation between true and estimated elongation is much better if $\sigma_{\Delta T_0} < 10\%$.

	initial	isothermal	polytropic
$T_0\,[keV]$	8.61	4.1 ± 0.2	4.2 ± 0.2
γ	1.3	1	0.5 ± 0.2
BIC	-	86	85

Table 12: The fit parameters assuming an isothermal and a polytropic gas, where $\sigma_{T(r)} \sim 0.5\,keV$, while the core core measurements are of the order $\sigma_{T(r)} \sim 0.1\,keV$. A comparison with the BIC reveals that both profiles fit the data equally.

	e_Δ	δ
true cluster	1.18	
cool core	0.72 ± 0.25	-1.84

Table 13: A cluster described by a PA-model with Vikhlinin temperature profile that has an accurate measurement of the the cool core. We fit an isothermal PA-model. δ gives the deviation from the true value in units of the standard deviation.

The reference profile which gives the position and the error bars on the temperature measurement, see right panel in figure 22, has a very accurate measurement of the cool core. This complicates the fitting procedure, since it tends to estimate a polytropic index $\gamma < 1$. More precisely, when we derive the analytic expressions that describe the projected quantities of a polytropic PA-model, see section 3.3.3, we had to include the assumption that $3m\beta > 1$. Hence, in equation (166), we must request that $\gamma \geq 1$. As a start, we skip the polytropic index and assume a isothermal gas. The accurate measurement of the cool core leads still to a bad estimation of T_0 but we guarantee that $\gamma \geq 1$. Table 12 gives the estimated parameters obtained from a resampled cool core profile. If we assume that the error on $T(r)$ is one fourth of the initial one ($\sigma_{T(r)} \sim 0.5\,keV$ in the outer regions) and $\sigma_{\Delta T_0}/\Delta T_0 = 10\%$, the isothermal PA-model underestimate the elongation, see table 13. In figure 33, we change the error on the temperature decrement between 1% and 22%.

Next, we want to include the polytropic profile. To improve the temperature fitting procedure, we discard the measurements that describe the cool core. The remaining data points describe a decreasing temperature profile. Under the assumption that $\sigma_{T(r)} \sim 0.5\,keV$ and $\sigma_{\Delta T_0}/\Delta T_0 = 10\%$, a fit with a polytropic and an isothermal PA-model provides the elongations listed in table 14.

Hence, we are closer to the true value than in the case where we include the cool core into our analysis. This means that the cool core has not a great influence on the estimation of the elongation.

Of course, this results depend very much on the very accurate measurements of the cool core. Let us assume that the measurements close to the center are not better than the measurements at $r > r_{cool}$, where r_{cool} is the scale of the cool core, see bottom right panel in figure 22. Hence, we have not to exclude the cool core measurements anymore, but we fit this data again with a polytropic and an isothermal PA-profile, see table 15.

In consideration of these assumptions, whereas the mean error on the temperature

	e_Δ	δ
true cluster	1.18	
isoth. without core	1.3 ± 0.4	0.3
polytr. without core	1.5 ± 0.4	0.8

Table 14: A cluster described by a PA-model with Vikhlinin temperature profile. We fit an isothermal and polytropic PA-model, where the cool core is discarded in the temperature profile fit. δ gives the deviation from the true value in units of the standard deviation.

	initial	isothermal	polytropic
$T_0\,[keV]$	8.61	4.9 ± 0.7	4.8 ± 0.4
γ	1.3	1	0.9 ± 0.3
BIC		47	53

Table 15: The fit parameters assuming an isothermal and a polytropic gas, whereas $\sigma_{T(r)} \sim 2\,keV$ for all measured radii. A comparison with the BIC reveals that we should prefer the isothermal profile.

	e_Δ	δ
true cluster	1.18	
cool core	1.1 ± 0.3	-0.3

Table 16: A cluster described by a PA-model with Vikhlinin temperature profile, where the cool core is not visible, that means, the error on the central measurements comparable to the error on the outer regions. We fit with an isothermal PA-model. δ gives the deviation from the true value in units of the standard deviation.

profile is $\sigma_{T(r)} \sim 2\,keV$ and $\sigma_{\Delta T_0}/\Delta T_0 = 10\%$, an isothermal PA-model gives the value in table 16 in good agreement with the true elongation.

Conclusion If the cluster whose electron density is described by a PA-model has a cool core, this feature adds new problems to the analysis of its observational data. Due to this few examples, we can say that it is better to discard the cool core, if we want to fit with a isothermal or polytropic profile and an exact measurement of the core is available. The isothermal and polytropic fit provides good estimations of the elongation. Of course, if we would include the Vikhlinin profile to model the cluster temperature, we should not discard those exact measurements. Otherwise, if $\sigma_{T(r)} \sim 2\,keV$ everywhere, we can use the isothermal profile even if there is a cool core and obtain a good estimated elongation. Next, one should vary the Vikhlinin profile parameters, e.g. the depth and width of the core, to confirm and improve those considerations.

4.7 Summary

Finally, we want to summarise the most important results we obtained in the previous section.

First, we observed several times that our method to estimate the elongation of clusters works.

In general, if the error on the temperature profile is in average larger than $1.5\,keV$ and the measured temperature profile consists of ~ 7 data points and no cool core is visible, one should prefer to fit the temperature profile with a isothermal gas. The polytropic profile has almost no advantages in this case, the deviation of the estimated elongation from the true value is comparable to the isothermal case. Hence, a bad temperature modeling and therefore a bad estimation of the cluster central temperature, which is usually underestimated, have not to make it impossible to estimate the elongation correctly. The over- and underestimation of certain parameters compensates a underestimated T_0. For example, we observed that the underestimation of the central temperature can compensate a wrong choice of γ up to a certain degree.

If the error on the temperature profile is small, $\sigma_{T(r)} < 1.0\,keV$, and no cool core is visible, the polytropic assumption will give a better estimation of the elongation. The isothermal fit tends to overestimate e_Δ. Both the isothermal β-model and the isothermal PA-model have this behaviour when the true cluster is given by their polytropic counterparts. Hence, the overestimation is not connected to the electron density model and is originated in the bad temperature modeling. If the error on the temperature

profile is $\sigma_{T(r)} < 1.5\,keV$, to avoid a systematic error a good temperature modeling is important.

If $\sigma_{T(r)} \sim 1.0\,keV$ and $\sigma_{\Delta T_0}/\Delta T_0 \sim 10\%$, we observed that the polytropic and isothermal β-model is able to estimate the elongation as good as a PA-model, if the true cluster is described by a polytropic PA-model, whereas the isothermal model gives even a better estimation. Probably, compensation effects occur if there is a bad modeling of the temperature profile and a bad n_e modeling at once. Nevertheless, the flat β-model is able to estimate the elongation of a cluster with the central peak in the electron density.

In general, if we fit a cluster with the correct model, a smaller error on the central temperature decrement results in a significantly better estimation of the elongation. This is not surprising, because the elongation depends inversely on the square of this decrement. But if the temperature profile has an accuracy of $\sigma_{T(r)} \sim 0.5\,keV$ or worse, one will not gain a more accurate result even if the error on the temperature decrement is smaller than 10%. Hence, if we compare with the $T(r)$-measurements of A1995 where $\sigma_{T(r)} \sim 2\,keV$, it is useful to obtain a more precise temperature profile in place of improving of the central temperature decrement measurement below $\sigma_{\Delta T_0}/\Delta T_0 \sim 10\%$.

Assume $\sigma_{T(r)} \sim 0.5\,keV$ and $\sigma_{\Delta T_0}/\Delta T_0 \sim 10\%$ and a cool core is visible in the temperature profile, that means there is an accurate measurement of it. If one choses a isothermal or polytropic temperature model to fit the cluster, one can discard the cool core measurements without lose the precision of the estimated elongation. Otherwise, a bad temperature model tends to underestimate the elongation. If the cool core has large error bars, e.g. the average error in all temperature measurements is $\sigma_{T(r)} \sim 2\,keV$, that means we are not able to identify it, an isothermal or polytropic fit gives a good estimation of the elongation. Obviously, the cool core does not affect the surface brightness or the temperature decrement so much that it is important to fit the temperature profile in consideration of the cool core. Hence, a bad temperature modeling has not to lead to a bad estimated elongation, if the temperature profile is adapted correctly.

The next possible steps to proceed are:

- In the examples we discussed, we examined mainly the importance of the correct temperature modeling. The influence of a bad n_e modeling should be studied more detailed.
- Can we always ignore the cool core if we fit with a isothermal of polytropic temperature profile? One can expect that the properties of the cool core are important.
- Can an isothermal model still give good estimations of the elongation if we model a cluster with a steeper initial temperature gradient, e.g. $\gamma = 1.5$? How does this depend on the radial resolution of the temperature profile? Probably, this is a general feature if $\sigma_{T(r)}$ is large.
- We can do these analyses with different simulated clusters that have more extreme elongations of $e_\Delta = 0.5$ or $e_\Delta = 1.6$. This can result in a amplification or attenuation of certain observed effects.

5 Conclusions and future prospects

In this thesis, we discussed different topics concerning galaxy clusters. First, we presented density models and temperature profiles which describe the ICM. Then, we combined those models and tried to find analytic expression for the X-ray surface brightness and for the central temperature decrement, that means we expressed the integrals in terms of well known functions. This was possible only in a few cases. When the profiles became more complex, we had to make some assumptions concerning the model parameters or actually, we did not even find an analytic expression, e.g. if we use the VE-model or the Vikhlinin temperature profile. We made this effort, because analytic expressions are much easier to fit on a observed surface brightness profile and it takes less computation time, for example. We summarised those expressions in a catalogue.

Then, we tried to build an example to show that it is in general not possible to estimate the elongation of a cluster if we only measure a X-ray surface brightness map. We managed to give a counterexample and we observed different scenarios of electron density model, shape and orientation. At the end, we can say in general: If only X-ray surface brightness is available, one can not determine the cluster shape.

Finally, in the main part of this thesis, we used the analytic results we had obtained to examine the estimation of the cluster shape through observation. We simulated the observational data, so that we exactly knew the initial parameters and we were able to test our method. Then, we fitted those simulations and observed how the estimated elongation deviates from the true value under certain circumstances: We assumed different errors on the temperature measurement and the estimation of the central temperature decrement. Sometimes, we used the true model or we used a simpler model for the electron density of the temperature profile. We also observed the behaviour of the estimated elongation if we varied a certain parameter of $T(r)$ or n_e. In general, we can say that a simple isothermal model leads often to results as good as fitting with the true model if the error on the temperature profile and the central temperature decrement are in the order of $\sigma_{T(r)} \sim 2\,keV$ and $\sigma_{\Delta T_0}/\Delta T_0 \sim 10\%$. In the case of more precise temperature measurements, a bad temperature modeling results in an overestimation of the elongation. If $\sigma_{T(r)} \sim 1\,keV$ and $\sigma_{\Delta T_0}/\Delta T_0 \sim 10\%$, the flat β-model is able to estimate the elongation of a cluster with the central peak in the electron density correctly. The cool core of a cluster can be ignored under certain circumstances, if we use a bad temperature modeling.

Further research is needed to answer a lot of open questions and to confirm the obtained results. The method we used should be tested with different simulated clusters with more extreme shapes or other temperature profiles. And last but not least, one should start to investigate true observations of clusters.

6 Some personal remarks

I had various problems to simulate data that really represents true observations and my Mathematica files grow larger and larger so that I lost the overview sometimes. But at the end, we managed to produce some results. Often, I found one answer but discovered two new questions. At the end I tried to reduce the analysis to simple cases. However, sometimes I was overwhelmed by the huge number of opportunities and possible solutions and it took a lot of time till I was fully satisfied with the results I obtained, because I knew that many questions were still open. But all in all, this was also very motivating and I enjoyed to work on this thesis.

7 Acknowledgments

I thank Prof. Dr. Philippe Jetzer and Dr. Mauro Sereno for the supervision of this thesis. They had always time to answer my questions and provided me with good advices. Especially, I want to thank Mauro for spending a lot of time for many helpful discussions and his detailed feedback on my work. In addition, he provided me with useful Mathematica-files which were a good basis to start my thesis.

I thank Dr. Elisabetha de Filippis for kindly providing us with the observational data of Abell 1995.

I thank my office colleagues Donnino Anderhalden, Timo Schmidt and Ursula Keller for making these nine months I was working on my thesis some of the most enjoyable of my studies.

Last but not least, I am thankful to my family for their great support and especially I thank Andrea Fahr for having much endurance and comprehension when I spend whole evenings in improving my Mathematica-files and giving me continuous encouragement.

A Constants

The used physical constants [PDG] and other initial values. Useful relations are: $1\,erg = 10^{-7}\,J$ and $1\,eV = 1.602176487 \times 10^{-19}\,J$.

speed of light in vacuum:	$c = 2.99792458 \times 10^{10}\,cm/s$
electron mass:	$m_e = 0.5109989\,MeV/c^2$
Thomson cross section:	$6.652458558 \times 10^{-33}\,cm^2$
Boltzmann constant:	$1.3806504 \times 10^{-23}\,J/K$
parsec:	$1\,pc = 3.0856776 \times 10^{18}\,cm$
Temperature of CMB:	$T_{CMB} = 2.725\,K$

B Parameter α

[Ettori 00] computed α in consideration of a polytropic gas. ΔT_e denotes the temperature range in the cluster.

$\Delta T_e[keV]$	$\alpha(Z = 0.3Z_\odot)$	$\alpha(Z = 1Z_\odot)$
5-10	0.25	0.16
5-7	0.37	0.27
3-6	0.47	0.36
3-5	0.54	0.41

Table 17: The α parameter if the given energy window is $1 - 10\,keV$.

C Useful Functions

The **Euler gamma function** satisfies

$$\Gamma(z) = \int_0^\infty t^{z-1} e^{-t} dt \tag{A-1}$$

if $Re(z) > 0$. The **Euler beta function** is given by

$$B(a,b) = \int_0^1 t^{a-1}(1-t)^{b-1} dt \tag{A-2}$$

if $Re(a) > 0$ and $Re(b) > 0$. $B(a,b)$ can also be expressed in terms of Γ-functions:

$$B(a,b) = \frac{\Gamma(a)\Gamma(b)}{\Gamma(a+b)} \tag{A-3}$$

Gauss' hypergeometric function can be written as

$${}_2F_1(a,b;c;z) = \frac{\Gamma(c)}{\Gamma(b)\Gamma(c-b)} \int_0^1 \frac{t^{b-1}(1-t)^{c-b-1}}{(1-tz)^a} dt \tag{A-4}$$

Through Euler's hypergeometric transformation one can find the fallowing identities [G & R] 9.131.1

$$
\begin{aligned}
{}_2F_1(a,b;c;z) &= (1-z)^{-a}\,{}_2F_1\left(a,c-b;c;\frac{z}{1-z}\right) && \text{(A-5)}\\
&= (1-z)^{-b}\,{}_2F_1\left(c-a,b;c;\frac{z}{1-z}\right) && \text{(A-6)}\\
&= (1-z)^{c-a-b}\,{}_2F_1\left(c-a,c-b;c;z\right) && \text{(A-7)}
\end{aligned}
$$

The hypergeometric function ${}_2F_1(a,b;c;z)$ is finite for arbitrary chosen a,b and c if $z<1$ and if $z=1$, the arguments have to fulfill $a+b<c$ to guarantee a finite function. 9.102 in [G & R]

D Additional Calculations

In section 3, we claim that (84) and (79) are equivalent.

$$
\begin{aligned}
&\frac{1}{\sqrt{f}}\frac{\Gamma[1/2-m\eta/4]\Gamma[3m\beta/2-1/2]}{\Gamma[-m\eta/4+3m\beta/2]}n_{e0}^m\,r_c && \text{(A-8)}\\
=\;&\frac{\sqrt{\pi}}{\sqrt{f}}\frac{\Gamma[-1/2+3m\beta/2]}{\Gamma[3m\beta/2]}n_{e0}^m r_c\;{}_2F_1\left[\frac{m\eta}{4},\frac{1}{2}(3m\beta-1),\frac{3m\beta}{2},1\right] && \text{(A-9)}
\end{aligned}
$$

(A-9) can be written as a β-function and than be expressed through an integral if $3m\beta>1$ and $m\eta<2$,

$$
\begin{aligned}
&\frac{n_{e0}^m\,r_c}{\sqrt{f}}\frac{\Gamma[1/2-m\eta/4]\Gamma[3m\beta/2-1/2]}{\Gamma[-m\eta/4+3m\beta/2]} && \text{(A-10)}\\
=\;&\frac{n_{e0}^m\,r_c}{\sqrt{f}}B[\frac{3m\beta}{2}-\frac{1}{2},-\frac{m\eta}{4}+\frac{1}{2}] && \text{(A-11)}\\
=\;&\int_0^1 t^{\frac{3m\beta}{2}-\frac{3}{2}}(1-t)^{-\frac{m\eta}{4}-\frac{1}{2}}dt && \text{(A-12)}
\end{aligned}
$$

On the other hand, (A-9) is given in terms of Gamma-functions and integrals as

$$
\begin{aligned}
&\frac{\sqrt{\pi}}{\sqrt{f}}\frac{\Gamma[-1/2+3m\beta/2]}{\Gamma[3m\beta/2]}n_{e0}^m r_c\;{}_2F_1\left[\frac{m\eta}{4},\frac{1}{2}(3m\beta-1),\frac{3m\beta}{2},1\right] && \text{(A-13)}\\
=\;&\frac{\sqrt{\pi}\,n_{e0}^m\,r_c}{\sqrt{f}}\,\frac{\Gamma[-1/2+3m\beta/2]}{\Gamma[3m\beta/2]}\,\frac{\Gamma[3m\beta/2]}{\Gamma[3m\beta/2-1/2]\Gamma[1/2]} && \text{(A-14)}\\
&\times\int_0^1\frac{t^{\frac{3m\beta}{2}-\frac{3}{2}}(1-t)^{\frac{1}{2}-1}}{(1-t)^{\frac{m\eta}{4}}}dt && \text{(A-15)}
\end{aligned}
$$

Since $\Gamma[1/2]=\pi$, (84) and (79) are equal.

E Integral Solutions

[G & R] 3.196.2

$$
\int_u^\infty(x+\beta)^{-\nu}(x-u)^{\mu-1}dx=(u+\beta)^{\mu-\nu}B(\nu-\mu,\mu) \qquad \text{(A-16)}
$$

if $|\arg\left(\frac{u}{\beta}\right)|<\pi,\mathrm{Re}(\nu)>\mathrm{Re}(\mu)>0$.

[G & R] 3.197.2

$$\int_u^\infty x^{-\lambda}(x+\beta)^\nu(x-u)^{\mu-1}dx = u^{\mu+\nu-\lambda}B(\lambda-\nu-\mu,\mu) \times {}_2F_1(-\nu,\lambda-\nu-\mu;\lambda-\nu;-\frac{\beta}{u}) \quad \text{(A-17)}$$

if $|\arg\left(\frac{u}{\beta}\right)| < \pi$ or $|\frac{\beta}{u}| < 1$, $\mathrm{Re}(\lambda-\nu) > \mathrm{Re}(\mu) > 0$.

[G & R] 3.259.3

$$\int_0^\infty x^{\lambda-1}(1+ax^p)^{-\nu}(1+\beta x^p)^{-\mu}dx = \frac{1}{p}a^{-\frac{\lambda}{p}}B(\frac{\lambda}{p},\nu+\mu-\frac{\lambda}{p}) \times {}_2F_1(\nu,\frac{\lambda}{p};\nu+\mu,1-\frac{\beta}{\alpha}) \quad \text{(A-18)}$$

if $|\arg(\alpha)| < \pi$, $|\arg(\beta)| < \pi$, $p > 0$, $2\,\mathrm{Re}(\mu+\nu) > \mathrm{Re}(\lambda) > 0$.

F Detailed Calculations of Several Integrals

Polytropic β-model: Equation (68) is calculated in the following way:

$$\int_\xi^\infty \left(1+(\zeta/r_c)^2\right)^{-\frac{3m\beta}{2}} \frac{\zeta d\zeta}{\sqrt{\zeta^2-\xi^2}} = \int_{\xi/r_c}^\infty \left(1+y^2\right)^{-\frac{3m\beta}{2}} \frac{r_c^2 y dy}{\sqrt{r_c^2y^2-\xi^2}} = \frac{1}{2}\int_{\xi^2/r_c^2}^\infty \left(1+y^2\right)^{-\frac{3m\beta}{2}} \frac{r_c dy^2}{\sqrt{y^2-\xi^2/r_c^2}}; \quad \text{(A-19)}$$

where first we changed $\zeta/r_c \to y$ and then we used $dy^2 = 2ydy$. We substitute $x \to y^2$, $u \to \xi^2/r_c^2$, $\beta \to 1$, $\mu \to 1/2$ and $\nu \to 3\beta m/2$ in (A-16). Since $3\beta m/2 > 1/2 > 0$ as long as $\beta > 1/3$ and $m \geq 1$, we can apply this equation and re-substitute to obtain

$$B(\nu-\mu,\mu)(u+\beta)^{\mu-\nu} = \frac{\Gamma(\nu-\mu)\Gamma(\mu)}{\Gamma(\nu)}(u+\beta)^{\mu-\nu} = \frac{\Gamma[-1/2+3m\beta/2]}{\Gamma[3m\beta/2]} r_c \left(1+\frac{\xi^2}{r_c^2}\right)^{\frac{1}{2}-\frac{3m\beta}{2}}. \quad \text{(A-20)}$$

Ploytropic PA-model: To calculate (77), we also start with the normalisation of the variable of integration $\zeta/r_c \to y$ and use $dy^2 = 2ydy$

$$\int_\xi^\infty (\zeta/r_c)^{\frac{-m\eta}{2}} \left(1+(\zeta/r_c)^2\right)^{-\frac{3m\beta}{2}+\frac{m\eta}{4}} \frac{\zeta d\zeta}{\sqrt{\zeta^2-\xi^2}}$$

$$= r_c \int_{\xi^2/r_c^2}^\infty (y^2)^{\frac{-m\eta}{4}} \left(1+y^2\right)^{-\frac{3m\beta}{2}+\frac{m\eta}{4}} \frac{dy^2}{\sqrt{y^2-\xi^2/r_c^2}} \quad \text{(A-21)}$$

Now, we can used (A-17) if we substitute $x \to y^2$, $u \to \xi^2/r_c^2$, $\beta \to 1$, $\mu \to 1/2$, $\nu \to -3m\beta/2 + m\eta/4$ and $\lambda \to m\eta/4$. Starting from the integrated general expression,

we obtain

$$
\begin{aligned}
& u^{\mu+\nu-\lambda} B(\lambda-\nu-\mu,\mu)\, {}_2F_1(-\nu,\lambda-\nu-\mu;\lambda-\nu;-\frac{\beta}{u}) \\
= \quad & \left(\frac{\xi^2}{r_c^2}\right)^{1/2-3m\beta/2} r_c \, \frac{\Gamma[-1/2+3m\beta/2]}{\Gamma[3m\beta/2]} \\
& \times {}_2F_1\left[-\frac{1}{4}m(\eta-6\beta), -\frac{1}{2}(1-3m\beta), \frac{3m\beta}{2}, -\frac{r_c^2}{\xi^2}\right]. \qquad \text{(A-22)}
\end{aligned}
$$

Polytropic VE-model, center: To calculate (91), where we set $\xi \to 0$ we start with the normalisation of the variable of integration $\zeta/r_c \to y$ and substitute $r_s \to f_s r_c$.

$$
\begin{aligned}
& \int_\xi^\infty (\zeta/r_c)^{\frac{-m\eta}{2}} \left(1+(\zeta/r_c)^2\right)^{-\frac{3m\beta}{2}+\frac{m\eta}{4}} \left(1+(\zeta/r_s)^\kappa\right)^{-\frac{\epsilon}{2\kappa}} \frac{\zeta d\zeta}{\sqrt{\zeta^2-\xi^2}} \\
= \quad & r_c \int_0^\infty (y)^{\frac{-m\eta}{2}} \left(1+y^2\right)^{-\frac{3m\beta}{2}+\frac{m\eta}{4}} \left(1+(y/f_s)^2\right)^{-\frac{\epsilon}{4}} dy \qquad \text{(A-23)}
\end{aligned}
$$

To simplify the integrand we assumed that $\kappa = 2$. Now, we can used (A-18) if we substitute $\lambda \to 1-\alpha/2$, $p \to 2$, $\beta \to 1$, $a \to f_s^{-2}$, $\mu \to \epsilon/4+m\eta/4$ and $\nu \to 3\beta/2+\alpha/4$. Starting from the integrated general expression, we obtain

$$
\begin{aligned}
& \frac{1}{p} a^{-\frac{\lambda}{p}} B(\frac{\lambda}{p}, \nu+\mu-\frac{\lambda}{p}) \\
& \times {}_2F_1(\nu, \frac{\lambda}{p}; \nu+\mu, 1-\frac{\beta}{a}) \\
= \quad & \left(\frac{r_c}{r_s}\right)^{-1+\alpha/2} \frac{\Gamma[1/2-\alpha/4]\Gamma[3\beta/2+\epsilon/4-1/2]}{\Gamma[-\alpha/4+3\beta/2+\epsilon/4]} \\
& \times {}_2F_1\left[\frac{3\beta}{2}-\frac{\alpha}{4}, \frac{1}{2}-\frac{\alpha}{4}, \frac{3\beta}{2}-\frac{\alpha}{4}+\frac{\epsilon}{4}, 1-(\frac{r_c}{r_s})^{-2}\right]. \qquad \text{(A-24)}
\end{aligned}
$$

electron density models	$S_X = \frac{\hat{\Lambda}(Z)}{4\pi\,(1+z)^4}\frac{2}{\sqrt{f}}(T_0)^{\alpha}\,n_{e0}^2\,l_c\times$	$l_c =$
$n_{e,\beta}(r) = n_{e0}\left(1+(r/r_c)^2\right)^{-\frac{3\beta}{2}}$	$\int\limits_{\xi/r_c}^{\infty}[1+(x)^2]^{-3\beta}\frac{[T_{min}/T_0+(x/f_{cool})^2]^{\alpha}}{[1+(x/f_{cool})^2]^{\alpha}}\frac{1}{[1+(x/f_t)^2]^{\alpha/2}}\frac{x dx}{\sqrt{x^2-(\xi/r_c)^2}}$	r_c
$n_{e,2\beta}(r) = \left(n_{e0,1}^2\left(1+(r/r_{c,1})^2\right)^{-\frac{3\beta_1}{2}} + n_{e0,2}^2\left(1+(r/r_{c,2})^2\right)^{-\frac{3\beta_2}{2}}\right)^{\frac{1}{2}}$	$\int\limits_{\xi/r_{c,2}}^{\infty}\left(\frac{f_e^2}{\left(1+(x/f_r)^2\right)^{3\beta_1}}+\frac{(1-f_e)^2}{\left(1+(x)^2\right)^{3\beta_2}}\right)^2$ $\times\frac{[T_{min}/T_0+(x/f_{cool})^2]^{\alpha}}{[1+(x/f_{cool})^2]^{\alpha}}\frac{1}{[1+(x/f_t)^2]^{\alpha/2}}\frac{x dx}{\sqrt{x^2-(\xi/r_{c,2})^2}}$ $f_e \equiv \frac{n_{e0,1}}{n_{e0}} = \frac{n_{e0,1}}{n_{e0,1}+n_{e0,2}}$, $f_r \equiv \frac{r_{c,1}}{r_{c,2}}$.	$r_{c,2}$
$n_{e,PA}(r) = n_{e0}\,(r/r_c)^{\frac{-\eta}{2}}\left(1+(r/r_c)^2\right)^{-\frac{3\beta}{2}+\frac{\eta}{4}}$	$\int\limits_{\xi/r_c}^{\infty}x^{1-\eta}[1+(x)^2]^{-3\beta+\frac{\eta}{2}}\frac{[T_{min}/T_0+(x/f_{cool})^2]^{\alpha}}{[1+(x/f_{cool})^2]^{\alpha}}\frac{1}{[1+(x/f_t)^2]^{\alpha/2}}\frac{dx}{\sqrt{x^2-(\xi/r_c)^2}}$	r_c
$n_{e,VE}(r) = n_{e0}\,(r/r_c)^{-\frac{\eta}{2}}\left(1+(r/r_c)^2\right)^{-\frac{3\beta}{2}+\frac{\eta}{4}}(1+(r/r_s)^{\kappa})^{-\frac{\epsilon}{2\kappa}}$	$\int\limits_{\xi/r_c}^{\infty}x^{1-\eta}(1+(x)^2)^{-3\beta+\frac{\eta}{2}}(1+(x/f_s)^{\kappa})^{-\frac{\epsilon}{\kappa}}$ $\times\frac{[T_{min}/T_0+(x/f_{cool})^2]^{\alpha}}{[1+(x/f_{cool})^2]^{\alpha}}\frac{1}{[1+(x/f_t)^2]^{\alpha/2}}\frac{dx}{\sqrt{x^2-(\xi/r_c)^2}}$ $f_s = \frac{r_s}{r_c}$	r_c

Table 18: X-ray surface brightness profile in the case of different electron density models. The temperature profile is given by the Vikhlinin temperature profile with $f_{cool} \equiv \frac{r_{cool}}{r_c}, f_t \equiv \frac{r_t}{r_c}$, where r_{cool} is the radius of the cool core and r_t the truncation radius at the outer regions. The last column gives the intrinsic length scale.

electron density models	$S_X = \frac{\hat{\Lambda}(Z)}{4\pi\,(1+z)^4}\frac{1}{\sqrt{f}}(T_{e0})^{\alpha}\,n_{e0}^2\,l_c\times$	$l_c =$
$n_{e,\beta}(r) = n_{e0}\left(1+(r/r_c)^2\right)^{-\frac{3\beta}{2}}$	$\sqrt{\pi}\frac{\Gamma[-1/2+3m\beta/2]}{\Gamma[3m\beta/2]}\left(1+\frac{r^2}{r_c^2}\right)^{\frac{1}{2}-\frac{3m\beta}{2}}$	r_c
$n_{e,2\beta}(r) = \left(n_{e0,1}^2\left(1+(r/r_{c,1})^2\right)^{-\frac{3\beta_1}{2}} + n_{e0,2}^2\left(1+(r/r_{c,2})^2\right)^{-\frac{3\beta_2}{2}}\right)^{\frac{1}{2}}$	$\left[\frac{\Gamma[-1/2+3m\beta_1/2]}{\Gamma[3m\beta_1/2]}f_e^2\left(1+\left(\frac{r}{f_r r_{c,2}}\right)^2\right)^{\frac{1}{2}-\frac{3m\beta_1}{2}}\right.$ $\left.+\frac{\Gamma[-1/2+3m\beta_2/2]}{\Gamma[3m\beta_2/2]}(1-f_e)^2\left(1+\left(\frac{r}{r_{c,2}}\right)^2\right)^{\frac{1}{2}-\frac{3m\beta_2}{2}}\right]$ $f_e \equiv \frac{n_{e0,1}}{n_{e0}} = \frac{n_{e0,1}}{n_{e0,1}+n_{e0,2}}$, $f_r \equiv \frac{r_{c,1}}{r_{c,2}}$.	$r_{c,2}$
$n_{e,PA}(r) = n_{e0}\,(r/r_c)^{\frac{-\eta}{2}}\left(1+(r/r_c)^2\right)^{-\frac{3\beta}{2}+\frac{\eta}{4}}$	$\sqrt{\pi}\frac{\Gamma[-1/2+3m\beta/2]}{\Gamma[3m\beta/2]}\left(1+\frac{r^2}{r_c^2}\right)^{\frac{1}{2}-\frac{3m\beta}{2}}$ $\times {}_2F_1\left[\frac{m\eta}{4}, -\frac{1}{2}(1-3m\beta), \frac{3m\beta}{2}, \frac{r_c^2}{r_c^2+r^2}\right]$	r_c
$n_{e,VE}(r) = n_{e0}\,(r/r_c)^{-\frac{\eta}{2}}\left(1+(r/r_c)^2\right)^{-\frac{3\beta}{2}+\frac{\eta}{4}}\left(1+(r/r_s)^{\kappa}\right)^{-\frac{\epsilon}{2\kappa}}$	$2\int_{\xi/r_c}^{\infty}(x)^{-\frac{m\eta}{2}}(1+(x)^2)^{-\frac{3m\beta}{2}+\frac{m\eta}{4}}\left(1+(x/f_s)^{\kappa}\right)^{-\frac{m\epsilon}{2\kappa}}\frac{xdx}{\sqrt{x^2-(\xi/r_c)^2}}$ $f_s \equiv \frac{r_s}{r_c}$	
	$S_{X0} = \frac{\tilde{\Lambda}(Z)}{4\pi\,(1+z)^4}\frac{1}{\sqrt{f}}\frac{\Gamma[1/2-m\eta/4]\Gamma[3m\beta/2+m\epsilon/4-1/2]}{\Gamma[-m\eta/4+3m\beta/2+\epsilon m/4]}$ $\times\frac{T_{e0}^{\alpha}}{T_{spec}^{\alpha}}\,n_{e0}^2\,r_c\,{}_2F_1\left[\frac{m\epsilon}{4}, \frac{2-m\eta}{4}, \frac{6m\beta-m\eta+m\epsilon}{4}, 1-(\frac{r_c}{r_s})^2\right]$	r_c

Table 19: X-ray surface brightness profile in the case of different electron density models. The temperature profile is polytropic with $m \to 2+\alpha(\gamma-1)$. The last column gives the intrinsic length scale.

electron density models	$\frac{\Delta T_{SZ}}{T_{CMB}} = f_{SZ}(\nu, T_e)\frac{\sigma_T k_B}{m_e c^2}\frac{2}{\sqrt{f}} T_{e0}\, n_{e0}\, r_c \times$	$l_c =$
$n_{e,\beta}(r) = n_{e0}\left(1+(r/r_c)^2\right)^{-\frac{3\beta}{2}}$	$\int\limits_{\xi/r_c}^{\infty}[1+(x)^2]^{-\frac{3\beta}{2}}\frac{[T_{min}/T_0+(x/f_{cool})^2]}{[1+(x/f_{cool})^2]}\frac{1}{[(1+(x/f_t)^2)]^{1/2}}\frac{xdx}{\sqrt{x^2-(\xi/r_c)^2}}$	r_c
$n_{e,2\beta}(r) = \left(n_{e0,1}^2\left(1+(r/r_{c,1})^2\right)^{-\frac{3\beta_1}{2}} + n_{e0,2}^2\left(1+(r/r_{c,2})^2\right)^{-\frac{3\beta_2}{2}}\right)^{\frac{1}{2}}$	$\int\limits_{\xi/r_{c,2}}^{\infty}\left(\frac{f_e^2}{\left(1+(x/f_r)^2\right)^{3\beta_1}}+\frac{(1-f_e)^2}{\left(1+(x)^2\right)^{3\beta_2}}\right)^{\frac{1}{2}}$ $\times\frac{[T_{min}/T_0+(x/f_{cool})^2]}{[1+(x/f_{cool})^2]}\frac{1}{[(1+(x/f_t)^2)]^{1/2}}\frac{xdx}{\sqrt{x^2-(\xi/r_{c,2})^2}}$ $f_e \equiv \frac{n_{e0,1}}{n_{e0}} = \frac{n_{e0,1}}{n_{e0,1}+n_{e0,2}}$, $f_r \equiv \frac{r_{c,1}}{r_{c,2}}$.	$r_{c,2}$
$n_{e,PA}(r) = n_{e0}\,(r/r_c)^{\frac{-\eta}{2}}\left(1+(r/r_c)^2\right)^{-\frac{3\beta}{2}+\frac{\eta}{4}}$	$\int\limits_{\xi/r_c}^{\infty}x^{1-\frac{\eta}{2}}[1+(x)^2]^{-\frac{3\beta}{2}+\frac{\eta}{4}}\frac{[T_{min}/T_0+(x/f_{cool})^2]}{[1+(x/f_{cool})^2]}\frac{1}{[(1+(x/f_t)^2)]^{1/2}}\frac{dx}{\sqrt{x^2-(\xi/r_c)^2}}$	r_c
$n_{e,VE}(r) = n_{e0}\,(r/r_c)^{-\frac{\eta}{2}}\left(1+(r/r_c)^2\right)^{-\frac{3\beta}{2}+\frac{\eta}{4}}(1+(r/r_s)^{\kappa})^{-\frac{\epsilon}{2\kappa}}$	$\int\limits_{\xi/r_c}^{\infty}x^{1-\frac{\eta}{2}}(1+(x)^2)^{-\frac{3\beta}{2}+\frac{\eta}{4}}(1+(x/f_s)^{\kappa})^{-\frac{\epsilon}{2\kappa}}$ $\times\frac{[T_{min}/T_0+(x/f_{cool})^2]}{[1+(x/f_{cool})^2]}\frac{1}{[(1+(x/f_t)^2)]^{1/2}}\frac{dx}{\sqrt{x^2-(\xi/r_c)^2}}$ $f_s = \frac{r_s}{r_c}$	r_c

Table 20: The temperature decrement in the case of different electron density models. The temperature profile is given by the Vikhlinin temperature profile with $f_{cool} \equiv \frac{r_{cool}}{r_c}, f_t \equiv \frac{r_t}{r_c}$, where r_{cool} is the radius of the cool core and r_t the truncation radius at the outer regions. The last column gives the intrinsic length scale.

electron density models	$\frac{\Delta T_{SZ}}{T_{CMB}} = f_{SZ}(\nu, T_e)\frac{\sigma_T k_B}{m_e c^2}\frac{1}{\sqrt{f}} T_{e0}\, n_{e0}\, l_c \times$	$l_c =$
$n_{e,\beta}(r) = n_{e0}\left(1+(r/r_c)^2\right)^{-\frac{3\beta}{2}}$	$\sqrt{\pi}\frac{\Gamma[-1/2+3\gamma\beta/2]}{\Gamma[3\gamma\beta/2]}\left(1+\frac{r^2}{r_c^2}\right)^{\frac{1}{2}-\frac{3\gamma\beta}{2}}$	r_c
$n_{e,2\beta}(r) = \left(n_{e0,1}^2\left(1+(r/r_{c,1})^2\right)^{-\frac{3\beta_1}{2}} + n_{e0,2}^2\left(1+(r/r_{c,2})^2\right)^{-\frac{3\beta_2}{2}}\right)^{\frac{1}{2}}$	$2\int_{\xi/r_{c,2}}^{\infty}\left(\frac{f_e^2}{\left(1+(x/f_r)^2\right)^{3\beta_1}} + \frac{(1-f_e)^2}{\left(1+(x)^2\right)^{3\beta_2}}\right)^{\frac{\gamma}{2}}\frac{xdx}{\sqrt{x^2-(\xi/r_{c,2})^2}}$ $f_e \equiv \frac{n_{e0,1}}{n_{e0}} = \frac{n_{e0,1}}{n_{e0,1}+n_{e0,2}}$, $f_r \equiv \frac{r_{c,1}}{r_{c,2}}$.	$r_{c,2}$
$n_{e,PA}(r) = n_{e0}\,(r/r_c)^{\frac{-\eta}{2}}\left(1+(r/r_c)^2\right)^{-\frac{3\beta}{2}+\frac{\eta}{4}}$	$\sqrt{\pi}\frac{\Gamma[-1/2+3\gamma\beta/2]}{\Gamma[3\gamma\beta/2]}\left(1+\frac{r^2}{r_c^2}\right)^{\frac{1}{2}-\frac{3\gamma\beta}{2}}$ $\times {}_2F_1\left[\frac{\gamma\eta}{4}, -\frac{1}{2}(1-3\gamma\beta), \frac{3\gamma\beta}{2}, \frac{r_c^2}{r_c^2+r^2}\right]$	r_c
$n_{e,VE}(r) = n_{e0}\,(r/r_c)^{-\frac{\eta}{2}}\left(1+(r/r_c)^2\right)^{-\frac{3\beta}{2}+\frac{\eta}{4}}\left(1+(r/r_s)^{\kappa}\right)^{-\frac{\epsilon}{2\kappa}}$	$2\int_{\xi/r_c}^{\infty}(x)^{-\frac{\gamma\eta}{2}}(1+(x)^2)^{-\frac{3\gamma\beta}{2}+\frac{\gamma\eta}{4}}\left(1+(x/f_s)^{\kappa}\right)^{-\frac{\gamma\epsilon}{2\kappa}}\frac{xdx}{\sqrt{x^2-(\xi/r_c)^2}}$ $f_s \equiv \frac{r_s}{r_c}$	
	$\frac{\Delta T_{SZ,0}}{T_{CMB}} = f_{SZ}(\nu, T_e)\frac{\sigma_T k_B}{m_e c^2}\frac{1}{\sqrt{f}}\frac{\Gamma[1/2-\gamma\eta/4]\Gamma[3\gamma\beta/2+\gamma\epsilon/4-1/2]}{\Gamma[-\gamma\eta/4+3\gamma\beta/2+\epsilon\gamma/4]}$ $\times T_{e0}^{\alpha}\, n_{e0}\, r_c$	
	$\times {}_2F_1\left[\frac{\gamma\epsilon}{4}, \frac{2-\gamma\eta}{4}, \frac{6\gamma\beta-\gamma\eta+\gamma\epsilon}{4}, 1-(\frac{r_c}{r_s})^2\right]$	r_c

Table 21: The temperature decrement in the case of different electron density models. The temperature profile is polytropic with $m \to 2+\alpha(\gamma-1)$. The last column gives the intrinsic length scale.

References

[Abell] Abell, G. / Corwin, H. / Olowin, R.: *A catalog of rich clusters of galaxies*, The Astrophysical Journal supplement series, **70**:1-138, 1989 May

[Bartelmann] Bartelmann, M.; Schneider, P.: *Weak gravitational lensing*, Physics Reports, **340**:291-472, 2001

[Bonamente] Bonamente, M. et al.: *Determination of the cosmic distance scale from Sunyaev-Zel'dovich effect and Chandra X-ray measurements of high-redshift galaxy clusters*, The Astrophysical Journal, **647**:25-54, 2006 August

[Cavaliere] Cavaliere, A.; Fusco-Femiano, R.: *The distribution of hot gas in clusters of galaxies*, Astronomy and Astrophysics, **70**:677-684, 1978 March

[Chakrabarty 08] Chakrabarty, D.; De Filippis, E.; Russell, H.: *Cluster geometry and inclinations from deprojection uncertainties*, Astronomy and Astrophysics, **487**: 75-87, 2008 May

[Fox & Pen 02] Fox, D. C.; Pen, U.: *The distance to clusters: correcting for asphericity*, The Astrophysical Journal, **574**:38-50, 2002 July

[Elser] Elser, S.: *Strong gravitational lensing in galaxy cluster Abell 963* , Bachelor thesis, University of Zurich, 2007 September

[Ettori 00] Ettori, St.: *β-model and cooling flows in X-ray clusters of galaxies*, MNRAS,**318**: 1041-1046, 2000 January

[Ettori 09] Ettori, St. et al.: *The cluster gas mass fraction as a cosmological probe: a revised study*, arXiv:0904.2740v2 [astro-ph.CO], 2009 April

[G & R] Gradshteyn, I. S.; Ryzhik, I. M.: *Table of integrals, series, and products*, Academic Press, New York and London, 1965

[Gioia] Gioia, I. M.: *X-ray clusters of galaxies as cosmological tools*, arXiv: 0908.2955v1, 2009 August

[Herbig] Herbig, T., Lawrence, C. R., Readhead, A. C. S., and Gulkis, S.: *A measurement of the Sunyaev-Zeldovich effect in the Coma cluster of galaxies*, The Astrophysical Journal, ApJ, 449, L5-L8, 1995

[Hogg] Hogg, D. W.: *Distance measures in cosmology*, arXiv:astro-ph/9905116v4, 2000 December

[Jetzer 03] Jetzer, Ph.: *High Energy Astrophysics I*, Troisième cycle de la physique en Suisse romande, 2003-2004

[Kazantzidis] Kazantzidis, S. et al.: *The effect of gas cooling on the shapes of dark matter halos*, The Astrophysical Journal, **611**: L73-76, 2004

[Liddle] Liddle, A.R.: *Information criteria for astrophysical model selection*, astro-ph/0701113, 2007

[Mazzotta] Mazzotta, P.; Rasia, E.; Moscardini, L.; Tormen, G.: *Comparing the temperatures of galaxy clusters from hydrodynamical N-body simulations to Chandra and XMM-Newton observations*, MNRAS, **354**: 10-24, 2004

[MathWorld] Weisstein, Eric W. *Euler angles* From MathWorld–A Wolfram Web Resource. http://mathworld.wolfram.com/EulerAngles.html

[NFW] Navarro, Julio F.; Frenk, Carlos S.; White, Simon D. M.: *Simulations of X-ray clusters*, MNRAS, 275..720N, 1995

[P & A 02] Pratt, G. W.; Arnaud, M.: *The mass profile of A1413 observed with XMM-Newton: Implications for the M-T relation*, Astronomy and Astrophysics, **394**: 375-393, 2002 July

[Planck] Planck Science Team *Planck: The Scientific Programme (Blue Book)*, ESA-SCI (2005)-1, European Space Agency, http://www.rssd.esa.int/SA/PLANCK/docs/Bluebook-ESA-SCI(2005)1_V2.pdf, Version 2, seen at 25.08.09

[PDG] C. Amsler et al. (Particle Data Group), Physics Letters **B667**, 1 ,2008

[Sarazin] Sarazin, C.L.: *X-ray emission from clusters of galaxies*, Cambridge Astrophysics Series, 1988

[Schneider] Schneider, P.: *Einfuhrung in die Extragalaktische Astronomie und Kosmologie*, Springer, Berlin, 2005, chapter 6

[Stark] Stark, A.A.: *Triaxial models of the bulge of M31*, The Astrophysical Journal, **213**: 368-373, 1977 April

[Sereno 07] Sereno, M.: *On the deprojection of clusters of galaxies combining X-ray, Sunyaev-Zeldovich temperature decrement and gravitational lensing maps*, MNRAS, **380**: 1207-1218, 2007 May

[SZ 70] Sunyaev, R. A.; Zeldovich, Ia. B.: *The spectrum of primordial radiation, its distortions and their significance*, Comments on Astrophysics and Space Physics, Vol. 2, p.66, 1970 March

[SZA] *Overview of the Sunyaev-Zeldovich Array*, University of Chicago, http://astro.uchicago.edu/sza/overview.html, seen at 24.08.09

[Reese 02] Reese, E.D.: *Determining the cosmic distance scale from interferometric measurements of the Sunyaev-Zeldovich effect*, The Astrophysical Journal, **581**:53-85, 2002 December

[Reese 03] Reese, E. D.: *Measuring the Hubble Constant with the Sunyaev-Zeldovich Effect*, Cambridge University Press, 2003, figure 1.1

[Vikhlinin 99] Vikhlinin, A.; Forman, W.; Jones, C.: *Outer regions of the cluster gaseous atmospheres*, The Astrophysical Journal, **525** : 47-57, 1999 November

[Vikhlinin 06] Vikhlinin, A. et al.: *Chandra Sample of Nearby Relaxed Galaxy Clusters: Mass, Gas Fraction, and Mass-Temperature Relation*, The Astrophysical Journal, **640**:691-709, 2006 April

[West] West, M.J.: *Anisotropic mergers at high redshifts: the formation of cD galaxies and powerful radio sources*, MNRAS, **268**:79-102, 1994

[XMM] Ehle, M. et al.: *XMM-Newton Users' Handbook*, Issue 2.5, XMM-PS-GM-14, European Space Agency, 2007 September

[Xue] Xue, Y.; Wu, X.: *Properties of the double β model for intracluster gas*, arXiv:0006131v1, 2000 June